Thesis for the Degree of Doctor of Philosophy

High sensitivity receivers for free-space optical communication links

Rasmus Larsson

CHALMERS

Photonics Laboratory
Department of Microtechnology and Nanoscience - MC2
Chalmers University of Technology
Göteborg, Sweden, 2024

High sensitivity receivers for free-space optical communication links
Rasmus Larsson

Acknowledgements, dedications, and similar personal statements in this thesis, reflect the author's own views.

ISBN 978-91-8103-085-3
Doktorsavhandlingar vid Chalmers tekniska högskola
Ny serie nr 5543
ISSN 0346-718X

Chalmers University of Technology
Microtechnology and Nanoscience - MC2
Photonics Laboratory
SE-412 96 Göteborg, Sweden
Phone: +46 (0) 31 772 1000

Front cover illustration: A Blender illustration of a front-end sensitive free-space receiver for optical coherent communication signals. Credits: NASA/JPL-Caltech/ASU/MSSS (image of Mars' surface), NASA/Goddard Space Flight Center Scientific Visualization Studio and Gaia DR2: ESA/Gaia/DPAC (The star map, used as sky texture)

Printed in Sweden by
Reproservice
Chalmers University of Technology
Göteborg, Sweden, August 2024

High sensitivity receivers for free-space optical communication links
Rasmus Larsson
Photonics Laboratory
Department of Microtechnology and Nanoscience - MC2
Chalmers University of Technology

Abstract

Space exploration today rely on radio frequency (RF) technologies to transmit data collected by space missions back to earth. Such RF communication links constitute a bottle-neck for new discoveries as their data rates fail to keep up with that generated by sophisticated instrumentation aboard modern space probes and rovers. As RF is reaching the limits of its capacity, the emerging technology of laser-based space communication is poised for take-over of future short- and long range space networks. The reduced diffraction loss of shorter wavelength-transmission is the driving factor behind this development which offers the opportunity to resolve the RF bottle-neck of deep space communications, if paired with efficient data modulation and sensitive reception.

A receiver technology offering both high sensitivity and spectral efficiency is that of optically pre-amplified coherent detection. When paired with a phase sensitive amplifier (PSA) as pre-amplifier, it provides the highest sensitivity for any coherent modulation format. Such a receiver could significantly boost both communication throughput and reach. However, the implementation of PSAs and coherent detection for large-area receivers is non-trivial as it requires single-mode reception and phase-locking of the received signal wave in practice.

This thesis addresses these practical challenges by (I): investigating different telescope architectures such as multi-mode and multi-aperture solutions, together with coherent combining of signals for realizing efficient and sensitive large-area single-mode coupled receivers; and by (II): simplifying the phase-locking of PSAs for practical free-space links. Results and demonstrations reported within this work showcases the possibility to achieve high data rate sensitive links and constitute important steps towards the practical implementation of PSA-preamplified large-area receivers for deep space communications.

Keywords: Phase sensitive amplifier, Optical phase-locked loop, Noise figure, sensitivity, Coherent combining, multi-aperture receiver

Publications

This thesis is based on the work contained in the following papers:

[A] **Rasmus Larsson**, Jochen Schröder, Magnus Karlsson, Peter A. Andrekson, "Coherent combining of low-power optical signals based on optically amplified error feedback", *Optics Express*, vol. 30, no. 11, pp. 19441-19455, May, 2022.
DOI: 10.1364/OE.456188

[B] **Rasmus Larsson**, Magnus Karlsson, Peter A. Andrekson, "Sensitive optical free-space receiver architecture for coherent combining of deep-space communication signals through atmospheric turbulence", *Manuscript submitted*

[C] **Rasmus Larsson**, Kovendhan Vijayan, and Peter A. Andrekson, "Zero-Offset Frequency Locking of Lasers at Low Optical Powers With an Optical Phase Locked Loop", *Journal of Lightwave Technology*, vol. 42, no. 3, pp. 1183-1190, Feb, 2024.
DOI: 10.1109/JLT.2023.3322634

[D] **Rasmus Larsson**, Kovendhan Vijayan, Jochen Schröder, Peter A. Andrekson, "Low-noise phase-sensitive optical parametric amplifier with lossless local pump generation using a digital dither optical phase-locked loop", *Optics Express*, vol. 31, no. 22, pp. 36603-36614, Oct, 2023.
DOI: 10.1364/OE.499280

[E] **Rasmus Larsson**, Ruwan U. Weerasuriya, Peter A. Andrekson, "Ultralow noise preamplified optical receiver using conventional sin-gle wavelength transmission", *Manuscript submitted*

Other publications by the author, not included in this thesis, are:

[F] **Rasmus Larsson**, Jochen Schröder, Magnus Karlsson, Peter A. Andrekson, "Coherent Combining at Ultra-low Optical Signal Powers based on Optically Amplified Error Feedback", in *Optical Fiber Communication Conference (OFC)*, Paper. W2A.31, 2022.
DOI: 10.1364/OFC.2022.W2A.31

[G] **Rasmus Larsson**, Kovendhan Vijayan, Jochen Schröder, Peter A. Andrekson, "Low-Noise Phase-Sensitive Optical Parametric Amplifier with Local Pump Generation using Digital Frequency and Phase Control", in *Optical Fiber Communication Conference (OFC)*, Paper. Th1B.4, 2023.
DOI: 10.1364/OFC.2023.Th1B.4

[H] **Rasmus Larsson**, Kovendhan Vijayan, and Peter A. Andrekson, in "Zero-Offset Frequency Locking of Lasers at Ultra-Low Optical Powers", in *Optical Fiber Communication Conference (OFC)*, **Post Deadline** Paper. Th4A.5, 2023
DOI: 10.1364/OFC.2023.Th4A.5

Contents

Abstract **iii**

Publications **v**

Acknowledgement **xiii**

Acronyms **xvii**

1 Introduction **1**
1.1 Background 1
1.2 This thesis 7

2 Free-space optical communications **9**
2.1 Data modulation 9
2.2 The free-space link 11
2.2.1 Atmospheric turbulence 13
2.2.2 Doppler shift 18
2.3 Signal reception 19
2.3.1 Noise 19
2.3.2 Channel compensation 21
2.3.3 Data recovery 22
2.3.4 Sensitivity 23

3 The dither-optical phase-locked loop **27**
3.1 Example setup 28

3.2 OPLL in time domain 29
3.2.1 1st order control loop 31
3.2.2 2nd order control loop 33
3.3 Optimising the dither-OPLL 35
3.3.1 OPLL in frequency domain 35
3.4 Phase error statistics 38

4 Large receiver area for coherent reception 41
4.1 Adaptive Optics 44
4.1.1 Performance of adaptive optics 47
4.1.2 Guide stars 48
4.2 Multi-mode reception 50
4.2.1 Performance of MMF-reception 52
4.3 Multi-aperture reception 54
4.3.1 Performance of multi-aperture reception 56
4.4 Coherent combining 57
4.4.1 Digital Combining 57
4.4.2 Optical Combining 58
4.4.3 Final MMF and multi-aperture performance 64
4.5 Comparing the methods 65
4.6 Additional details 66
4.6.1 OPLL impact on BER 67
4.6.2 Performance for varying signal bandwidth 68
4.6.3 Coherent combining at multiple wavelengths 69

5 PSA implementation for free-space optics 73
5.1 PSA basics 73
5.1.1 Phase matching 74
5.1.2 Four wave mixing 75
5.1.3 Three wave mixing 77
5.1.4 Phase sensitive amplification 78
5.2 Phase sensitive amplification of data 84
5.2.1 The two-mode PSA 84
5.2.2 The one-mode PSA 87
5.3 Phase-locking of PSAs 89
5.3.1 Signal tapping 90
5.3.2 Pump carrier recovery 92
5.3.3 Local pump locking 94

6 Conclusion & Future outlook 97

7 Summary of papers **103**

A Appendix A **I**
A.1 Calculations for the AO-systems I
A.1.1 AO model I
A.1.2 The ISS to ground AO sensitivity III
A.1.3 Estimation of background intensity III
A.2 Factor relating angle of arrival and tip-tilt phase IV

Included papers A–E **V**

Acknowledgement

The completion of this thesis was made possible thanks to the support of my supervisors, colleagues, friends and family, who all deserve honorable mentions.

First, I would like to thank Prof. Peter Andrekson for providing me the opportunity to pursue my doctoral studies at the photonics lab, but also for all the support as my supervisor and the interesting PSA-related discussions along the way. I want to thank Prof. Magnus Karlsson for the support as my co-supervisor, for always taking the time to answer my optics related questions and for organizing the excellent course on photonics, which during my Master's studies undoubtedly guided me on the path towards this thesis. I also want to thank Dr. Jochen Schröder for all the support as my co-supervisor, our DSP-related discussions and for attempting to convert me to coding in python (I'm half-way there).

In getting my hands on the experimental work in the lab I wish to thank Dr. Ravikiran Kakarla and Dr. Kovendhan Vijayan for their guidance and the experience they shared with me. I also want to thank Dr. Ali Mirani and Dr. Zonglong He for many interesting discussions and for always helping out in the lab. Dr. Ping Zhao deserves a big thanks for many interesting discussions and his inspiring research drive. I also want to thank Dr. Ruwan Udayanga for the collaborative effort in the lab and the discussions on SBS suppression.

For nice discussions on frequency locking and related experiments I would like to thank Dr. Krishna Sundar Twayana, Dr. Òskar Bjarki Helgasson, Dr. Connor Skehan and Dr. Fuchuan Lei. A special thank you to Dr. Marcello Girardi for teaching me about photonic integrated chip

design and characterization. I also want to thank Dr. Israel Rebolledo-Salgado for teaching me how to operate the chip characterization stage and for being a role-model in taking lab notes. Dr. Alexander Caut and Yi Sun also deserves thanks for the collaboration on the chip-combiner and thank you to Erik Börjesson for our discussions on FPGAs.

I am grateful to Dr. Ekaterina Deriushkina for having been a fantastic colleague and friend, supporting me during our five years of Phd studies together. Thank you so much! I also want to thank Estrella Torres and Johan Kolvik for the refreshing kitchen talks amidst the, sometimes, long and late hours of work.

I wish to thank Prof. Åsa Haglund for her great work in heading the optics course for bachelor physics students which I had the opportunity to help teaching. I also want to thank my co-teachers Dr. Filip Hjort, Dr. Alexander Grabowski, Erik Strandberg, Lars Persson and Johan Kolvik for sharing the effort in inspiring students toward the fascinating world of optics and photonics. With that said, I also wish to thank Dr. Jörgen Bengtsson, Dr. Per Rudquist and Prof. Victor Torres-Company for inspiring lectures on optics and photonics during my student years. Prof. Victor Torres-Company also deserves a special thanks for his help and advice on my career path towards being accepted as a Phd student.

To all my colleagues at the photonics lab, I truly cannot emphasize enough how much your positive attitude and helpfulness has mattered in realizing a welcoming environment and the privilege I have felt while working here. Each and everyone of you have my sincere gratitude. I also want to thank you for organizing the photonics nights which helped secure me on my path to this point. So also, I wish to thank Olle Rosenqvist for providing me the opportunity to do my master's project at Thorlabs sweden where special thanks go to my, then, supervisors Dr. Kristof Seidl and Dr. Stina Guldbrand for supporting me. Looking back further, I wish to express sincere thanks to Mikael Stöberg and Christina Lundberg for excellent teaching and who have played pivotal roles in sparking my interest for physics, which ultimately brought me here.

Finally, I wish to thank all my friends for brightening my life on the side from work. I want to express my special gratitude to Sarah Ronström Kern for the food excursions, games, adventures and overall amazing time I've had the opportunity to share with you. I want to thank Maja Larsson for being a wonderful sister and, to my parents Lars and Päivi Larsson, thank you for your unwavering support during my

many years of studying, this work would not have been possible without you. Lastly, I thank myself, for the dedication and motivation that helped me surmount the many tireless hours of work that is this thesis.

Rasmus Larsson
Göteborg, August 2024

Acronyms

RF	radio-frequency
PPM	Pulse-position modulation
MRO	Mars Reconnaissance orbiter
DSN	deep-space network
GEO	geostationary orbit
FEC	forward error correction
LLCD	Lunar laser communication demonstration
AU	astronomical units
LEO	Low earth orbit
LLO	Low lunar orbit
DSOC	deep space optical communications
LRCD	laser communication relay demonstration
SN-SPD	super-conducting nano-wire single photon detector
APD	avalanche photo-detector
MPSK	M-ary phase shift keying
LO	local oscillator
EDFA	erbium doped fiber amplifier
PSA	phase sensitive amplifier
OPLL	optical phase locked loop
MMF	multi-mode fiber
OOK	on-off keying
PSK	phase-shift keying
BPSK	binary PSK
QPSK	quadrature PSK

FPA	focal plane-array
SNR	signal to noise ratio
SMF	single mode fiber
PSD	power spectral density
NF	noise figure
PIA	phase-insensitive parametric amplifier
ASE	amplified spontaneous emission noise
AWN	amplified vacuum noise
DSP	digital signal processing
ADC	analog to digital converter
BER	bit error rate
PPB	photons per bit
PPIB	photons per information bit
OIL	optical injection-locking
CW	continuous wave
PLL	phase locked loop

CHAPTER 1

Introduction

Humans comprise a curious species. Our inherent drive to explore and understand the world we inhibit provokes new discoveries, tools and technologies. For each tool we create and technology we develop, our realm of possibilities expand, pushing our boundaries, our confines and limits ever farther. This is our nature, since ancient settlers crossed great seas in exploratory inquisitiveness to now, where we turn our gaze from our all-too familiar earth, to the vast space beyond. Our curiosity lends us new questions, and in our pursuit for answers, we look as far and wide as we can.

1.1 Background

Space exploration today consists of a broad range of technologies to map and probe the universe around us. Large ground-based telescopes and antennas allow us to detect electromagnetic waves for astronomical imaging [1] and spectroscopy [2]. Sensing of other types of cosmic radiation are also performed, such as cosmic muon detection [3] and recently, gravitational waves [4].

While much information can be garnered from earth-based receivers, the vast distance to the objects we observe limit the amount of information retrievable. The density of a rock on Mars cannot be probed by the radiation reflected off it, nor can the rock itself be resolved in an image

taken by an earth-based telescope. To overcome these limitations, space missions are launched to locations of interest, carrying appropriate sensing equipment to perform the desired measurements. For instance, on the surface of Mars reside currently two operational rovers; Curiosity [5] since 2012, whose mission involve geological and climate monitoring and Perseverance [6] since 2020, whose mission involve sample caching and atmospheric oxygen tests as preparation for future manned missions.

Although space missions allow us to breach the distance between earth and, so far, the remainder of our solar system [7] (Voyager1), they bring with them the challenge of long-distance space communications. The information produced by a distant space probe is of no use for us unless the information can be retrieved.

Most space missions today rely on radio-frequency (RF) communication for upload of instructions to the space-craft and download of measurement data to earth. The current state-of-the-art in RF communications for deep space rely on the Ka-band (26-40 GHz) and can achieve a few Mb/s of downlink data rates at distances of 0.5 astronomical units (AU) (1 AU $\approx 150 \cdot 10^6$ km), as demonstrated in the Mars Reconnaissance orbiter (MRO) space mission from 2005 [8]. The demonstrated data-rate would allow a typical 1 megapixel black and white image (∼8 Mb in size) to be retrieved every other couple of seconds from a space-craft orbiting Mars when Mars passes by earth, see Fig 1.1 for overview. With modern sophisticated cameras and measurement equipment able to capture data at rates of Gb/s and more, it is clear that the Mb/s RF communication will be a bottle neck for the discoveries these missions can leverage. With manned space missions on the horizon for space agencies such as NASA [9], the need for higher data rate deep space communications is further evident to support and entertain future mission crews.

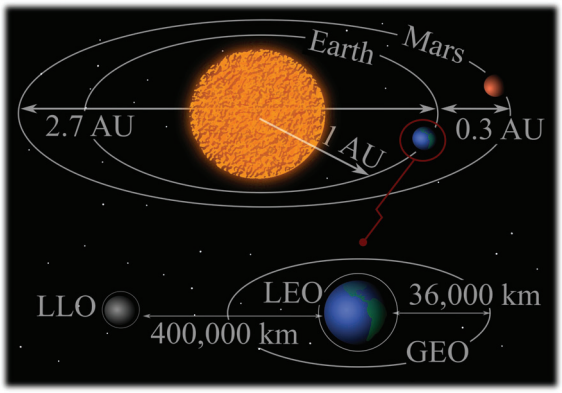

Figure 1.1: Distance overview, Mars-earth, earth-moon and geostationary orbit (GEO). Low earth orbit (LEO) (∼2,000 km); Low lunar orbit (LLO)

The main challenge of deep space communications is the vast channel distance, which incur significant power loss of the electromagnetic

Figure 1.2: Beam divergence for a 32 GHz RF-beam with 3 m diameter transmitter and a 193.5 THz optical beam with a 10 cm diameter transmitter.

waves used for data-transmission. The loss stems from the divergence of the transmitted beam and the inability to, in practice, realise a large enough receiver to capture all transmitted power. The issue of free-space loss in a Mars-earth communication link is demonstrated in Fig. 1.2 which illustrates the beam divergence for electromagnetic radiation at two different frequencies and transmitter antenna sizes. In the RF communication link only a very small fraction of the transmitted power reaches earth, and out of that power it is paramount to capture as much as possible. Due to fundamental noise limitations, more of which we will discuss later, there is a minimum required amount of received energy per data bit transmitted, if that data bit is to be recovered correctly. The required energy per bit is typically denoted as receiver sensitivity. A higher received power thus allows a higher data rate. Hence, to receive more power and sustain adequate data rates, antenna sizes for the ground-based RF deep-space network (DSN) feature large diameters between 30 to 70 m [10]. They enabled the Mb/s data rate from Mars in [8], however, to achieve Gb/s data rates at Mars-earth distances or further, the antenna size would become impractically large. Meanwhile, transmit-area and power is typically already maximised to the extent possible, as volume, mass and power on a space-craft is severely limited due to the traditionally high cost per kg of payload sent into space [11]. Other than attempting to reduce receiver sensitivity with use of high sensitivity modulation formats [12] and forward error correction (FEC) codes [13], there are currently no realistic prospects to achieve much higher data rate RF communications for deep space. Instead, an emerging development that shows the potential to overcome the bottle-neck of deep-space communications, reside in the field of free-space optical communications.

The invention of the laser in the 1960s started a series of advances in optics and detectors, providing key technologies for what would enable light-based data transmission. This field of research brought on the vast fiber-optic communication network that enables the globalised, high-speed internet we enjoy today. Despite the wide-spread success of fiber-optical communications, the interest in laser-based free-space communication has been slow in development, that is, until recently. The high optical frequency, hundreds of THz vs. tens of GHz for RF, allow for a much larger modulation bandwidth [14] which in addition to enabling higher data rates, also prevents frequency-channel congestion thanks to the wide spectrum available. Furthermore, the short optical wavelength significantly limits the beam divergence compared to RF [14] (see Fig. 1.2), thus improving power-efficiency which in turn promotes both higher data rates and reach.

Since the first successful bi-directional ground-to-orbit laser communication demonstration in 1997 [15] and orbit-to-orbit link in [16] (1998), others followed suit, with the first deep-space demonstration performed by NASA's Lunar laser communication demonstration (LLCD) in 2013 [17]. The LLCD showcased laser-based communication at 1550 nm wavelength between a satellite orbiting the moon and a ground station on earth, featuring data rates of 300-600 Mb/s, by then the highest ever achieved via communication to or from the moon.

With the LLCD having paved the way for future optical deep space communication, NASA again set the record in their ongoing deep space optical communications (DSOC) mission, in which they successfully streamed a high-definition video at 267 Mb/s back to earth from the Psyche mission located 31 million kilometers away (about 80 times the earth-moon distance) [18]. Leading up to this demonstration in late 2023, NASA's laser communication relay demonstration (LRCD) has in the last few years provided a platform for testing and experimentation of laser-communications within GEO and between GEO and ground to further improve and develop free-space optical technologies [19]. The LRCD, furthermore, enables the first optical platform for relaying deep-space optical communication signals down to earth, improving line-of-sight and help in overcoming the atmospheric turbulence for future deep space missions.

Looking ahead, the next manned mission to the moon, the Artemis II mission, will also feature an optical communications transceiver module [20] with targeted data rates in the hundreds of Mb/s with a later target

to reach Gb/s. These demonstrations and upcoming missions tell a clear story in favour of optical free-space communications as the new platform for communicating into deep space and it is likely that many future deep-space missions will follow in their tracks.

The benefits of optical communications do, however, entail a number of practical challenges. As shown in Fig. 1.2, the narrow optical beam requires more accurate pointing to ensure that the transmit-signal strikes the receiver. To produce and receive the short wavelength-beam efficiently, stringent tolerances on the telescope-optics need to be met during manufacture. The short optical wavelength also makes the beam prone to deformation when propagating through earth's turbulent atmosphere which severely limits the efficiency of larger ground-based receive-telescopes.

To partly relieve these issues the use of larger photo-detector areas are employed, typically together with direct-detection modulation formats such as amplitude or Pulse-Position Modulation (PPM) [21]. In fact, PPM was used in NASA's LLCD and LRCD missions and has demonstrated record low required energies per bit together with the use of super-conducting nano-wire single photon detectors (SN-SPDs) [22] and avalanche photo-detectors (APDs) [23]. However, the inefficient use of bandwidth for PPM, in combination with the limited bandwidths of SN-SPDs and APDs, effectively restricts the possible data rates one can achieve with direct-detection PPM communication. While PPM offers state-of-the-art sensitivity and the possibility to receive arbitrarily low powers, at the expense of data rate, there remains an interest in alternatives that can enable high data rate laser communications for deep-space.

Coherent optical communication is a technology well-versed in the fiber-optics community. The signal and local oscillator (LO)-beating in a coherent receiver, not only boosts the sensitivity but also allows additional modulation formats, such as M-ary phase shift keying (MPSK) and higher order QAM [24]. Although shot noise-limited sensitivity is attainable in theory with a strong LO, low detector quantum efficiencies limit the sensitivity in practice. For modern day optical telecom-systems, this problem was solved by the advent of the erbium doped fiber amplifier (EDFA) [25] back in the 1980s. Optical amplification, e.g. using an EDFA, boosts the signal power before detection and can typically achieve sensitivities of 4 dB (3 dB ideally) above the shot noise-limit. The EDFA-compatible telecom wavelength-bands, C (1530-1560 nm) and L-band (1560-1625 nm), also overlap well with the transmission

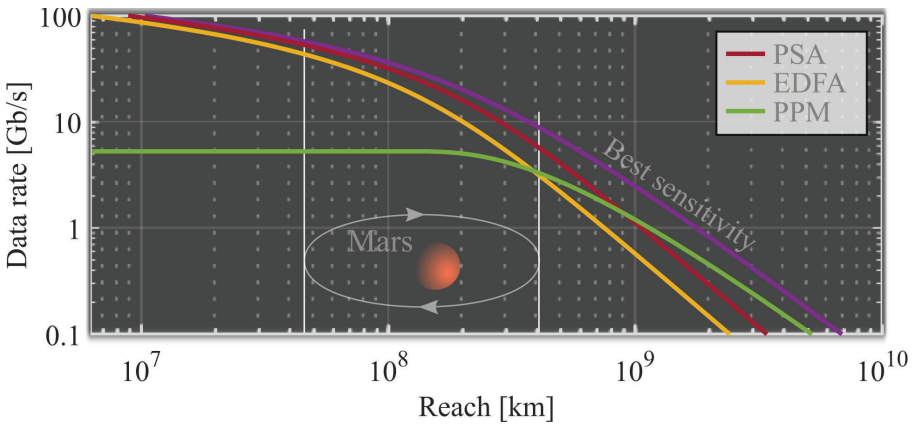

Figure 1.3: Receiver communication reach vs. achievable data rate for different receiver types. The theoretical curves assume a 10 GHz detection bandwidth, 1.55 µm wavelength, a 1 m diameter transmitter with 10 W transmit power and a 10 m diameter receiver.

window of earth's atmosphere. Thanks to the mature state of coherent fiber-optical communication, power-efficient transmitters, receivers and components are readily available at commercial prices.

In comparison, Fig. 1.3 shows the achievable data rate vs. reach for both PPM and coherent systems with an optimistic yet plausible transmitter-receiver configuration. It illustrates the restricted data rate of PPM with the use of a typical 10 GHz bandwidth-limited detector. Hence, in this example, the EDFA pre-amplified coherent receiver can provide much higher data rates than PPM for distances up to the earth-Mars distances. Meanwhile, PPM retains superior performance over the EDFA at very long reach. The approaches of PPM and coherent thus complement each other. However, in the region of transition there are attainable sensitivity gains with the use of phase sensitive amplifiers (PSAs) [26]. Like EDFAs, PSAs can be used as pre-amplifiers for coherent optical receivers. Their implementation differs form that of stimulated emission-based EDFAs and instead rely on parametric amplification via a non-linear interaction between signal, idler and one or several strong optical pumps waves [26]. In short, PSAs can in principle reach shot noise-limited sensitivity, i.e. 0 dB noise figure (NF) vs. the 3 dB NF quantum-limit of EDFAs [27]. Several significant PSA demonstrations have been performed [28–33], with a record-low sensitivity of 1 photon/bit (2.1 dB above the shot noise-limit) achieved in [34].

To reach sensitivities below the conventional 3 dB quantum-limit, PSAs are operated in phase-sensitive mode, i.e., all optical waves, signal, idler and pump(s), must be phase-locked. This requirement poses a

significant challenge for PSAs in optical communications as signal and pump-waves, created at transmitter and receiver, respectively, will be uncorrelated from free-running laser frequency drifts and phase noise. The result in [34] demonstrates the potential of PSAs in applications where both sensitivity and high data rates are desired. However, their implementation for deep-space laser communications require a sophisticated signal and pump-wave phase-locking solution, that does not burden the space-craft transceiver with impractical complexity.

In addition, to leverage the use of PSAs and coherent fiber technologies at large, for deep space communications, another big challenge remains in the interface between free-space and fiber. The relatively large size of SN-SPDs and APDs for PPM-detection circumvents the need for fiber reception in contrast to coherent, where the incoming beam should be focused into a 10 micron diameter core of a single-mode fiber (SMF). Any telescope imperfection, pointing error or turbulence-induced beam-deformation, will significantly degrade the power-coupling. Unfortunately, these problems are further exacerbated with increasing telescope size, meanwhile it is the size that is key to power-efficient reception. Thus it is crucial that these problems are solved if PSA pre-amplified coherent optical receivers are to enable high-speed, sensitive, communication for deep-space missions.

Provided the practical solutions to achieve sensitive PSA pre-amplified coherent reception, the bandwidth limitations of current deep-space communications can be overcome and the present bottle-neck in space-exploration discoveries may be resolved.

1.2 This thesis

This thesis addresses the practical challenges of implementing large-area receivers and PSAs as pre-amplifiers for free-space optical communications. Among different approaches toward larger telescope receive-areas is the idea of a multi-aperture array. By collecting the incident signal with many smaller telescopes one can avoid impractical tolerances and high costs [35]. In paper [A], optical coherent combining of individually sampled signals from 4 apertures is investigated. Phase fluctuations between the four channels were compensated using a new, optically pre-amplified error feedback control system, based on a dither-optical phase locked loop (OPLL). The system performance was experimentally tested in the limit of low received powers, something that had not been explored

in the context of optical coherent combining previously. While paper [A] targets the compensation of relative phase variations only, paper [B] extends the investigation to incorporate compensation of amplitude fluctuations, as would be present at a ground-based multi-aperture array receiving through the turbulent atmosphere. A comparative analysis between multi-mode and multi-aperture reception is also covered. Numerical simulations are used to model expected fluctuations at plausible telescope sites which are then used to test the low-power performance of the control system in [A].

Previously, PSA demonstrations for practical communication links have relied on pump-carrier regeneration either using a pump reference propagated from the transmitter [26, 36, 37] or part of the communication signal itself [38, 39]. The minimum reference power required for pump-generation negatively impacts the link power-efficiency and hence receiver sensitivity at low signal powers. In paper [C], we lower the limit of the required reference power by more than 10 dB by demonstrating a novel dither-OPLL for frequency locking of lasers at record-low powers. In paper [D], we show for the first time a practical PSA-implementation without the need for transmitter pump references or signal-tapping. The PSA pump is locked locally using a dither-OPLL that continuously maximises the PSA gain. Finally in paper [E], we implement a dual-pump degenerate PSA which removes the need for idler-wave generation at the transmitter. This result enables PSA pre-amplified reception of signals generated using conventional transmitter optics already suited in typical space-crafts like the LLCD and LRCD missions.

The thesis is outlined as follows, the free-space optical communication link alongside its challenges is explained in chapter 2. The dither-OPLL, which constitute an essential part of the work in this thesis, is described in chapter 3. Chapter 4 provide a detailed overview of current technologies enabling larger free-space to fiber reception area and chapter 5 discusses different methods for implementing PSAs for free-space optical communications. Conclusions are given in chapter 6 together with a future outlook in the field of high-speed, sensitive optical receivers for deep-space communication. Finally, the papers are summarized in chapter 7.

CHAPTER 2

Free-space optical communications

To discuss different implementations of large area receivers and PSAs for high-sensitivity free-space optical reception, it is first necessary to understand the practical challenges they face. Hence, this chapter serves as a basic introduction to the free-space optical communication link, its core concepts and the associated challenges.

2.1 Data modulation

To transmit data one can utilize several properties of the electromagnetic wave, such as its magnitude $|E|$, phase ϕ, polarization, frequency, time or its spatial distribution. From these properties, several different modulation formats can be defined in which a specific combination of e.g. magnitude and phase corresponds to a symbol with a designated sequence of bits (ones and zeros). While information encoded in time, field magnitude and spatial distribution may be recovered by simply measuring the power in a photo-detector or focal plane array (FPA), phase, polarization and frequency typically requires coherent detection where the signal wave is interfered with an LO-wave.

Some examples of sensitive modulation formats [40, 41] are shown in Fig. 2.1. In the top are constellation diagrams of on-off keying (OOK) and coherent phase-shift keying (PSK) formats: binary phase-shift keying (BPSK) and quadrature phase-shift keying (QPSK). They are illus-

trated in the complex plane where the radial distance from zero represents the field magnitude and the angle vs. the positive real axis represents the phase. Each brown dot (or ring) represents a symbol with corresponding bit(s) attached and each symbol occupies a fixed slot in time, creating a time-sequence of symbols with corresponding bits to be transmitted.

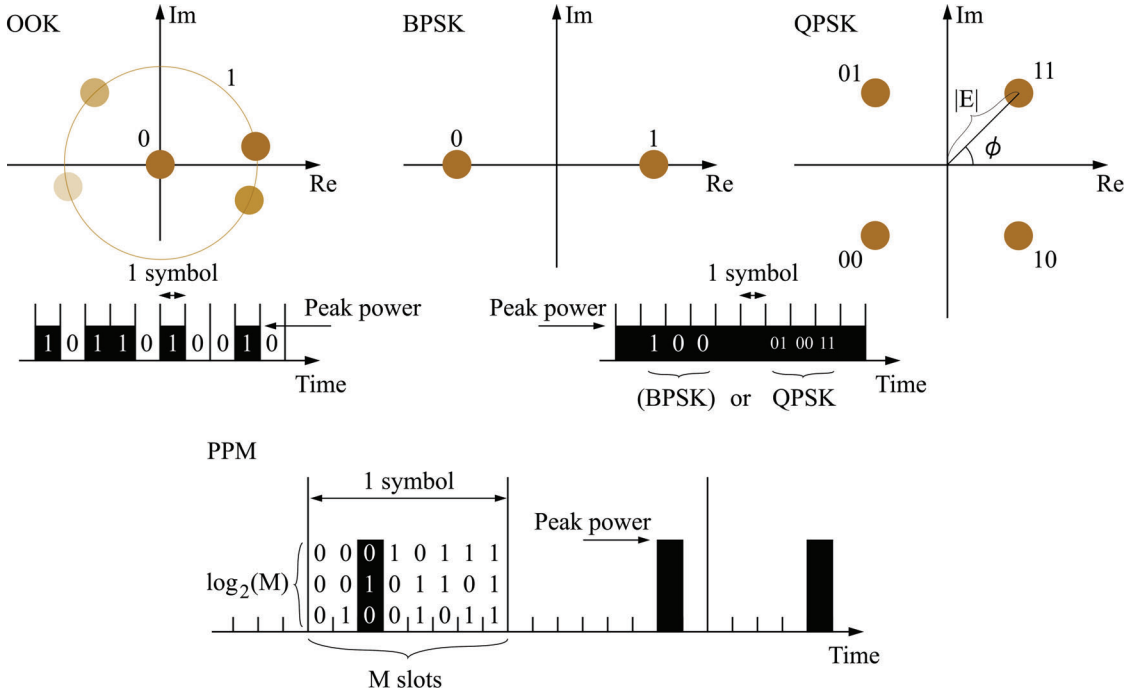

Figure 2.1: Illustration of different modulation formats suited for sensitive free-space optical communications.

In QPSK the number of unique symbols M=4 whereas as in BPSK M=2, this allows 2 times as many bits to be transmitted per symbol and time slot. Higher order (M)-modulation formats can thus enable more data per time, typically $\log_2(M)$ bits per symbol. However, as eluded to in chapter 1, the power-requirement per bit will favour simpler, low-order formats at low signal to noise ratio (SNR) [30, 40, 42]. This is true for fixed time-slot modulation formats. For Pulse-Position Modulation (PPM) (shown in the bottom of Fig. 2.1), whose symbol time slot size is proportional to the modulation order M, the opposite is true. In PPM the power per symbol is allocated entirely into a $1/M$-slot which boosts the power per bit as $M/\log_2(M)$ for higher M, making higher order M-PPM a highly sensitive modulation format. The high sensitivity of PPM comes at a cost in the amount of bits transmitted per unit time, which scales as $\log_2(M)/M$ w.r.t. M.

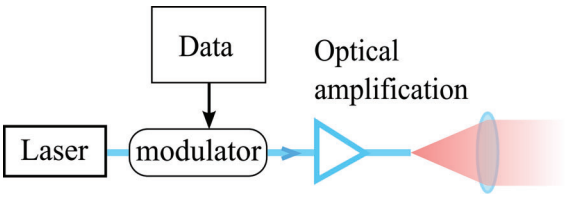

Figure 2.2: A basic transmitter configuration for an optical free-space link.

To apply the data to the amplitude and/or phase of the electro-magnetic wave one can use an electro-optic modulator, driven by the data-encoded voltage signal. A schematic of a typical transmitter in a free-space optical link is shown in Fig. 2.2. The wave itself is generated using a continuous wave (CW) laser that launches the wave through the modulator which applies the data. Thereafter an optical amplifier boosts the transmit power before the wave is coupled out into free-space using a lens or telescope.

2.2 The free-space link

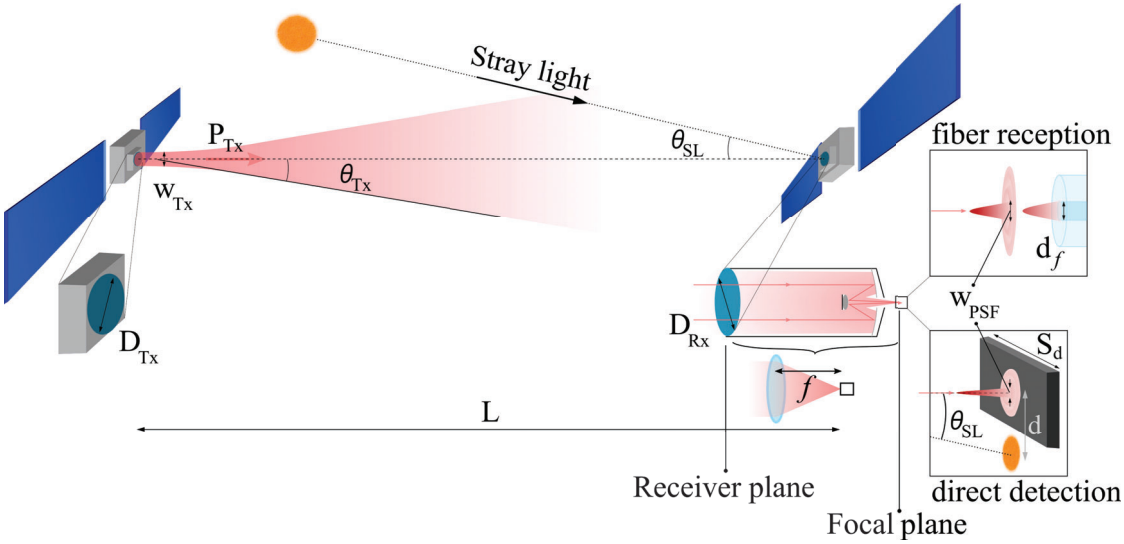

Figure 2.3: A schematic of a satellite-to-satellite optical free-space channel.

The free-space optical link is a point-to-point link encompassed primarily by the transmitter, a free-space vacuum or atmospheric channel and the receiver. In Fig. 2.3 we consider a satellite-to-satellite link in space. Here, a transmitter akin to that in Fig. 2.2 launches a free-space beam of power P_{Tx} from an aperture of diameter D_{Tx}. The transmitted field will diffract in free-space, its divergence can be modelled using Gaussian beam formalism, with divergence angle $\theta_{Tx} = 2\lambda/(\pi w_{Tx})$. Here, λ is the wavelength and w_{Tx} is the beam diameter. Using this the field can be propagated the distance L between transmitter and receiver to calcu-

late the power P_{Rx} incident on the receive-aperture and the end-received power $P_r = \eta_r P_{Rx}$ as [43]

$$P_r = \frac{P_{Tx}\eta_t D_{Tx}^2 \eta_r D_{Rx}^2}{4L^2\lambda^2}, \tag{2.1}$$

assuming $w_{Tx} \ll L$ and $D_{Rx} \ll \theta_{Tx} L$. Here, η_t is the transmit optics efficiency which accounts for the difference between D_{Tx} and w_{Tx} and D_{Rx} is the receive-aperture diameter. Meanwhile, η_r is the efficiency of the receive-optics and depends on the type of reception.

To increase overall received power, Eq. (2.1) indicates increasing either transmit power, transmit or receive-aperture sizes or reducing the the wavelength, as mentioned already in chapter 1. The diffraction loss is proportional to channel distance squared and Fig. 2.4 a) illustrates its characteristic for deep-space links within the solar system for three different combinations of aperture sizes.

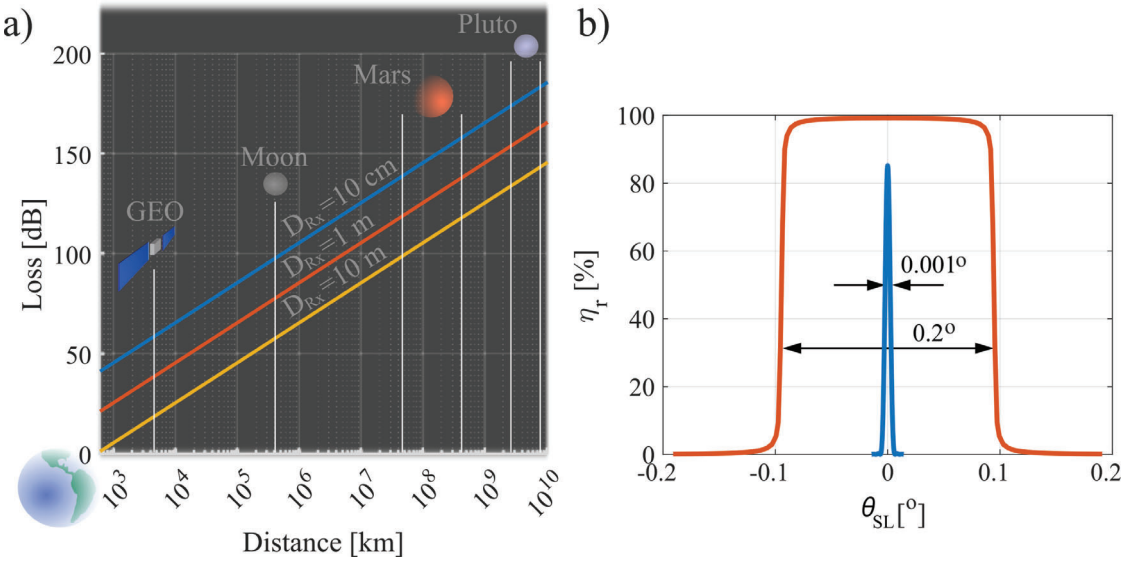

Figure 2.4: a) The free-space link diffraction loss for $\lambda = 1550\,\text{nm}$, $D_{Tx} = 10\,\text{cm}$ and D_{Rx} as indicated in the figure. b) Example of detection efficiency vs. angle of incidence for SMF reception (blue) and a 1 mm sized photo-detector area (orange). Focal length $f = 26$ cm, wavelength $\lambda = 1550$ nm and receiver aperture diameter $D_{Rx} = 10$ cm.

From a receiver perspective, it is important to both maximise D_{Rx} as well as η_r. In practice, these parameters depend heavily on the type of reception. Fig. 2.3 illustrates both direct detection as well as fiber-based reception, both of which uses a focusing element (lens or telescope) of focal length f to concentrate the collected power into a diffraction-limited

spot-size

$$W_{\text{PSF}} = 2.44\lambda f/D_{Rx}. \tag{2.2}$$

For direct detection, P_r consist of all power focused onto the the photo-detector (of size S_d in black) while for fiber-reception, P_r is the power coupled into the fiber, given by the spatial mode-overlap between the focused field and fiber-mode.

Large super-conducting nano-wire single photon detector (SN-SPD)-sizes of 1 mm^2 [44], compared to mode-matched single mode fiber (SMF)-reception, alleviates receiver alignment significantly. The acceptance angle for the SN-SPD is $\theta_{\text{SN-SPD}} = 0.5S_d/f$ and for the mode-matched SMF $\theta_{\text{SMF}} = 0.5W_{\text{PSF}}/f = 1.22\lambda/D_{Rx}$. The SMF acceptance angle is independent of f and fiber core size since the diffraction-limited spot-size should match the fiber core size $d_f \sim W_{\text{PSF}}$ (see Fig. 2.3).

Fig. 2.4b) shows an example of the power reception efficiency vs. incidence-angle θ_{SL} for the two cases where the SN-SPD enables an acceptance cone roughly 200 times wider than for the SMF. Note how a larger aperture size reduces θ_{SMF}, which implies a trade-off between D_{Rx} and η_r in a practical system were non-zero alignment-error will remain.

In the context of direct detection, this issue is circumvented and both a high η_r and D_{Rx} can typically be achieved by scaling f or the detector size. Although direct detection enjoys this benefit thanks to simpler alignment, it is more susceptible to stray light noise sources like stars or daylight atmospheric scattering. This is especially problematic for single photon-counting receivers to reach high sensitivity. Consequently, by reversing the perspective, fiber-reception provides a much narrower spatial filtering which reduces the impact of such noise sources.

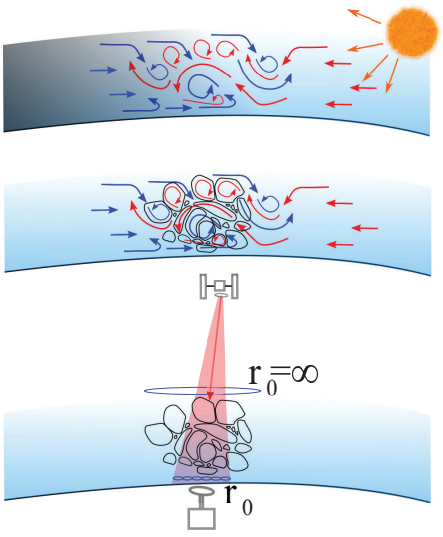

Figure 2.5: Atmospheric turbulence, caused by temperature gradients from the day-night cycle, creating a spatially varying refractive-index.

2.2.1 Atmospheric turbulence

So far, we have assumed a free-space vacuum channel. However, when considering transmission from or to a ground station we must take into account the channel-effects of the atmosphere. The

day-night cycle of earth heats and cools the atmosphere sequentially, generating temperature-gradients that causes winds which in turn mixes the air in a turbulent fashion, see Fig. 2.5. This turbulence creates a time-dependent structure of air-pockets of different temperature, and hence of different refractive index. When a ground-station receives a beam propagating through the atmosphere the time-varying and inhomogeneous refractive index spatially deforms and uncorrelates the received wave. A common metric known as the Fried parameter r_0 measures the coherence radius of the field after propagation along an atmospheric path and can be calculated from the atmospheric refractive-index structure parameter C_n^2 (for a plane wave) as [45]

$$r_0 = \left[0.423k^2 \int_{\text{path}} C_n^2(z)dz\right]^{-3/5}, \quad k = \frac{2\pi}{\lambda}. \tag{2.3}$$

The "path" represents the trajectory of the propagation through the atmosphere and z is the length coordinate along the trajectory. A typical C_n^2 vs. altitude model is shown in Fig. 2.6 which indicate that a stronger turbulence tends toward the ground. Hence, to reduce the effect of turbulence on the propagating light, receivers for both optical communications and astronomical observations are built at high altitudes atop mountains. The height also shortens the "path" through the atmosphere and brings the receiver "closer" to space.

Snapshots of simulated turbulence-perturbed fields are shown in Fig. 2.7 both at the receiver plane and the focal plane (see Fig. 2.3 for reference) for different turbulence strengths (r_0). Here the receiver plane-field is collected by a 80 cm diameter aperture and focused down to the focal plane with $f = 2.4$ m to match the spot size to the mode of a 10 µm diameter core SMF.

In the weak turbulence case ($r_0 = 60$ cm), the received field amplitude is still relatively constant, phase is relatively flat and most of the focused power is injected into the fiber. As r_0 decreases further, stronger spatial field variations are produced and less power is collected by the fiber mode, significantly reducing η_r.

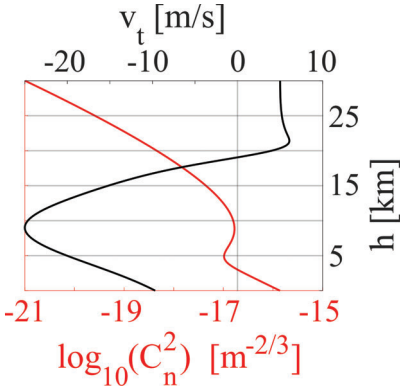

Figure 2.6: Hufnagel-Valley model of the atmospheric refractive index structure parameter C_n^2 and a Gaussian atmospheric wind-profile model vs. altitude h.

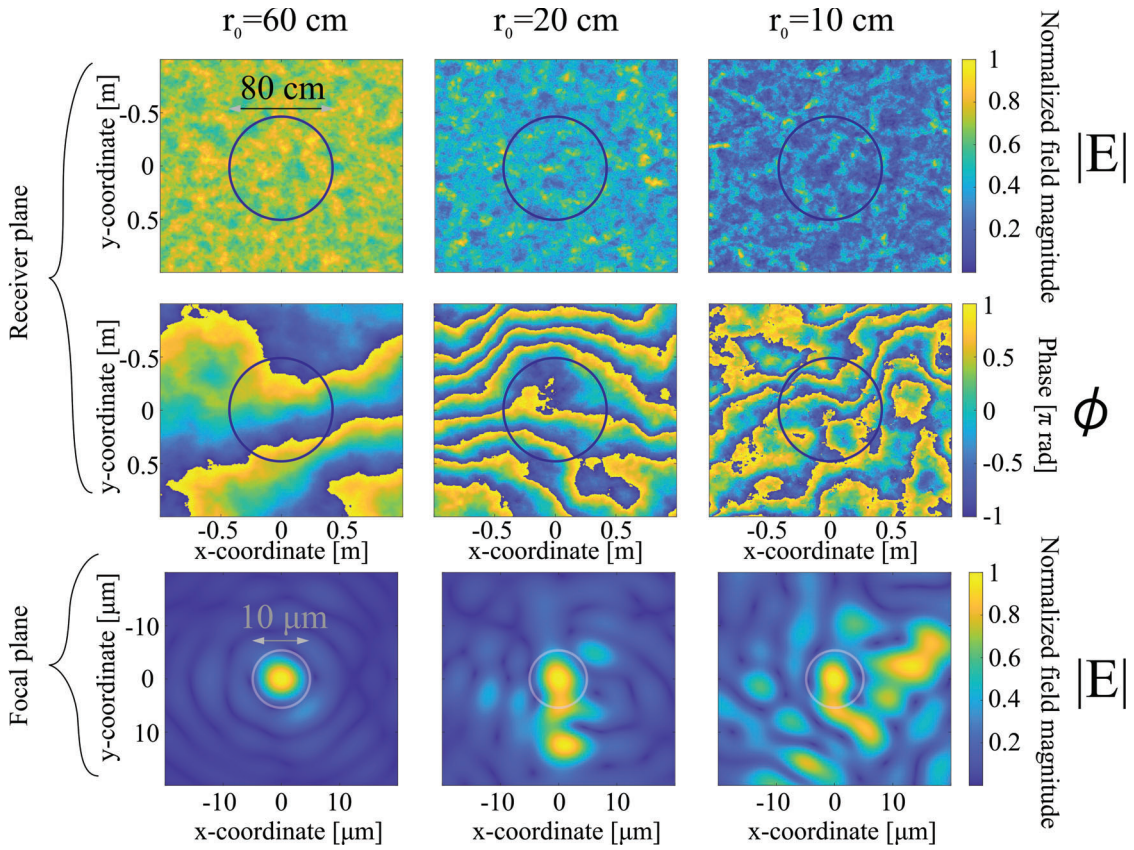

Figure 2.7: Simulated spatial field magnitude and phase in the receiver plane (see Fig. 2.3) for different turbulence cases with spatial coherence radii of 60, 20 and 10 cm respectively. The simulation used a vertical path from space to an altitude of 1 km, with C_n^2 as in Fig. 2.6. In the bottom row are the corresponding spatial field magnitudes in the focal plane as captured by a 80 cm diameter aperture in the receiver plane. A focal length of 2.4 m narrows the beam for reception into a 10 µm diameter SMF.

For increasing ratio $D_{Rx}/r_0 > 1$ we see that the focused power is no longer contained in the diffraction limited spot-size W_{PSF}. Instead, it is spread across a new, larger size given by $W_{r_0} \sim 2.44\lambda f/r_0$ as shown in Fig. 2.8. This is the turbulence-limited spot-size and is made up of roughly $(D_{Rx}/r_0)^2$ number of speckles of diffraction-limited size W_{PSF}. Even if the size of the turbulence limited spot is reduced to match the fiber mode size, e.g. by choosing a shorter f,

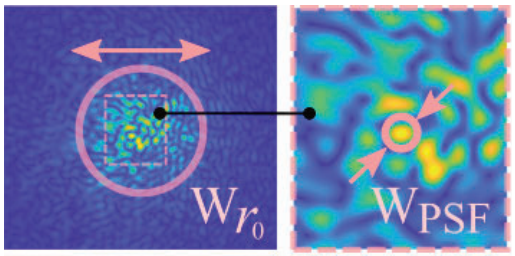

Figure 2.8: The turbulence-limited spot size and the speckle size for $D_{Rx} = 80$ cm and $r_0 = 10$ cm.

its irregular and dynamically changing field profile caused by the speckles prohibits efficient coupling into a single fiber mode. Hence, for single-mode reception, the turbulence limits the aperture size to $D_{Rx} \leq r_0$ for efficient reception. Meanwhile, a 1 mm sized SN-SPD can more or less capture all power incident on the aperture for these three turbulence cases and do not suffer the same limitation. The possible ways to overcome the challenge of single-mode reception under atmospheric turbulence we reserve for chapter 4.

Fig. 2.7 and Fig. 2.8 represent a snap-shot in time, in reality the spatial profile varies through time as well. This results in significant power and phase fluctuations of the collected field and will impact the sensitivity of the receiver. Both the absolute phase at a single point in the receiver plane, as well as the relative phase between two spatially separated points will be modulated by the atmosphere. In the latter case, the power spectral density (PSD) can be modelled by [46, 47]

$$S_\phi(f) = 0.0326k^2 f^{-8/3} \int_{\text{path}} C_n^2(z) v^{5/3}(z) dz \tag{2.4}$$

where $v(z)$ is the path-transverse wind speed along the trajectory. As it is wind that is mixing and altering the atmospheric refractive index-profile it makes sense that it is via its inclusion in Eq. (2.4) we obtain the PSD. Simulated PSDs of SMF-collected field-phase and field-power are shown in Fig. 2.9 for different r_0 values, a vertical path and a typical gaussian wind-profile vs. altitude (see Fig. 2.6). The PSDs indicate a

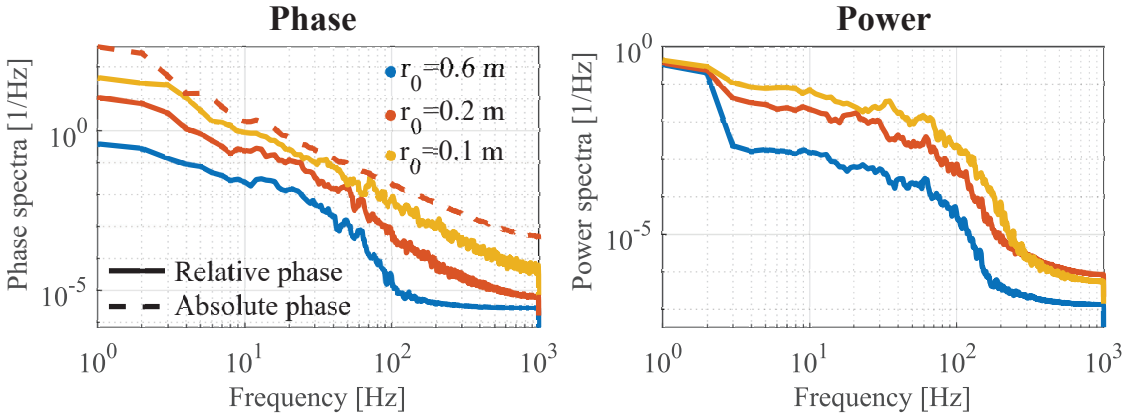

Figure 2.9: Left: Simulated PSD of the relative and absolute phase of SMF-collected fields from two adjacent apertures with $D_{Rx} = 20$ cm for different r_0. Right: Simulated PSD for SMF-collected power using a $D_{Rx} = 20$ cm aperture for different r_0. Note the simulation noise floor in the high-frequency limit.

limited bandwidth within 1 kHz, which is typical for atmospheric links

through the atmosphere.

The power variation can moreover be described by the Scintillation index σ_I^2 which is the power variance of the wave received by the aperture [48]. For optical communications relying on coherent modulation the scintillation only results in a time-varying instantaneous power (or SNR) variation, whereas for direct detection modulation formats, with power-dependent symbols, the link performance can be significantly degraded. The effect of scintillation can be remedied by increasing the aperture size, where the variance of the power collected inside the aperture decreases thanks to aperture averaging $\sigma_I^2 \rightarrow A\sigma_I^2$ and generally depends on D_{Rx} in a space-to-ground link as [49]

$$A \simeq 0.9(h_0\lambda/D_{R_x}^2)^{7/6}. \tag{2.5}$$

Here $h_0 = h_0(C_n^2(z))$ [m] depends on the turbulence channel.

Finally, since the relative phase between different points in the receiver plane varies with time, the phase-front topology will as well, which, when received by a finite-sized aperture, leads to angle of arrival (AOA) fluctuations, see Fig. 2.10. The AOA fluctuation will limit the single-mode reception via the same principle as the overall receiver misalignment discussed earlier. The average efficiency degradation due to AOA fluctuations for single-mode reception can be modelled by[B]

$$\eta_{\text{AOA}} = e^{-\alpha(D_{Rx}/r_0)^{5/3}} \tag{2.6}$$

where α is a constant. The expression highlights, once more, the limitation of efficient large-area single-mode reception imposed by the atmosphere.

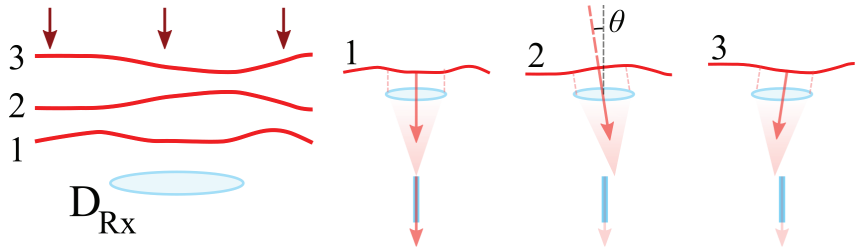

Figure 2.10: Illustration of AOA fluctuations for a receiver with aperture size D_{Rx}. The AOA is indicated by θ.

The time-domain characteristic of the atmospheric turbulence channel is important for the techniques used to compensate it, especially the phase variation of the received field, which we shall discuss further in

chapter 4. While this time-variation also affect direct detection, the large detector area allows for significant spatial averaging (and large D_{Rx}) with relative practical simplicity in contrast to single-mode reception, which helps reduce otherwise detrimental power fluctuations.

2.2.2 Doppler shift

For optical communications in space there will exist relative movement between transmitter and receiver. This relative motion will impose a Doppler shift $\Delta\nu_d = v_r/c \cdot \nu$ of the transmitted light with respect to the receiver, where v_r is the relative speed and c the speed of light.

Fig. 2.11 shows the frequency shifts that would be obtained in a link between Mars and earth (left) and between a Low earth orbit (LEO) satellite and the point on earth's equator below the LEO orbit (right), as well as their respective time derivatives (frequency drifts). The peak Doppler shift in the Mars-earth link corresponds to a relative speed of roughly 14 km/s.

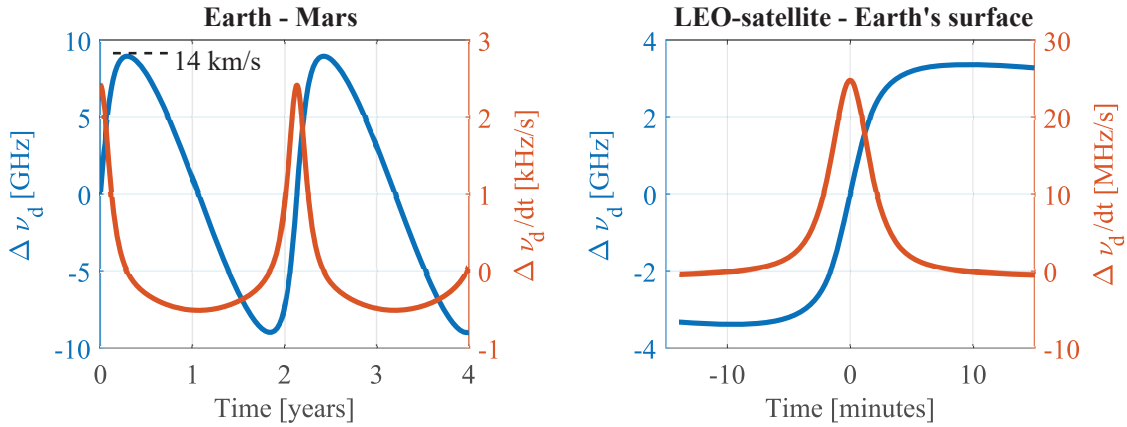

Figure 2.11: Doppler shift and its time derivative (drift) vs. time from relative velocities between earth-Mars (left) and between a LEO-satellite and a point on the equator below the orbit during a pass.

Meanwhile, the fastest man-made space-craft, The Parker Solar Probe, reached a speed of 194 km/s relative to the sun which would correspond to a frequency shift of $\sim$ 125 GHz. Large absolute frequency shifts may become problematic depending on the wavelength tunability of the receiver lasers, however, the rate at which the frequency shift changes is equally (if not more) important, i.e. the drift $d\Delta\nu_d/dt$. In this case, the LEO-to-ground Doppler shift may be more challenging even though the earth-Mars link experiences larger relative speeds.

2.3 Signal reception

In order to recover the transmitted information the receiver must convert the modulation of the optical wave into a voltage signal that can be sampled by an analog to digital converter (ADC) for computer interfacing. Again, if coherent modulation formats are used, coherent detection is necessary to extract phase information in addition to amplitude. Figure 2.12 (top) is an illustration of typical coherent reception. Here, the fiber-coupled light is pre-amplified using an optical amplifier before the out-of-band optical noise from the amplifier is filtered away using an optical filter. Finally the signal is combined with an local oscillator (LO) in the coherent receiver which detects both the in-phase and quadrature components of the signal.

The setup for direct detection in the bottom of Fig. 2.12 simply uses a photo-detector, e.g. a SN-SPD for sensitive free-space communications, as mentioned previously. Either type of reception will suffer from a range of different noise sources which will determine the sensitivity of a particular combination of modulation format and reception.

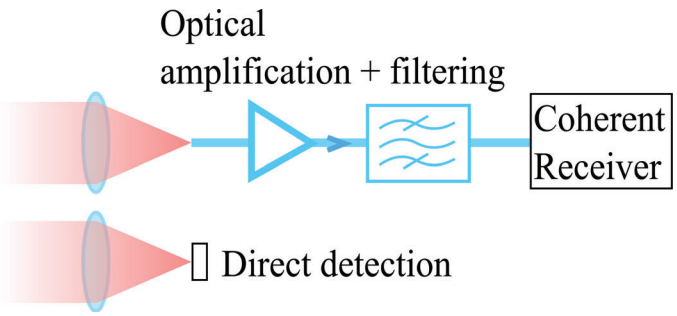

Figure 2.12: Top: coherent reception using optical fiber pre-amplification. Bottom: direct detection.

2.3.1 Noise

Both in the direct-detection and coherent detection cases the conversion of optical power to current (and later voltage) is manifested in a photo-detector. The below list summarizes the variances of the noise-contributions to the generated current-signal:

- Shot noise $\sigma_s^2 = 2qR_dP\Delta f$
- Thermal noise $\sigma_T^2 = \frac{4K_BT}{R}\Delta f$

- Signal-Noise beating $\sigma^2_{\text{S-N}} = 4R_d^2 P S_{\text{N}} \Delta f$
- Noise-Noise beating $\sigma^2_{\text{N-N}} = 4R_d^2 S^2_{\text{N}} \Delta f \left(\Delta\nu_0 - \frac{\Delta f}{2} \right)$

Here, q is the electron charge, R_d is the photo-detector responsivity, P is the power of the signal (amplified or not) or the LO power (whichever is higher) incident on the detector, Δf is the signal bandwidth (symbol rate), K_B is Boltzmann's constant, T is the photo-detector temperature in Kelvin, R is the load impedance, S_N is the (white) PSD of the optical noise incident on the detector and $\Delta\nu_0$ is the optical filter bandwidth.

The shot noise contribution arise from the discrete arrivals of photons with associated uncertainty in time described by a Poisson distribution. Note that at large number of arrived photons per unit time this distribution tends toward the normal distribution.

The thermal noise contribution is caused by black-body radiation from the photo-detector itself and its environment. The radiation is partly re-absorbed in the photo-detector, exciting additional electron-hole pairs that acts as noise.

In the case where optical noise is present in the channel alongside the signal, this will also be detected and add to the current-signal. A typical wide-band optical noise ($> \Delta\nu_0$) beats both with the signal and with different spectral components of itself in the photo-detector, thus generating corresponding noise variances. The optical noise may consist of stray light or of the optical noise generated in an optical amplifier. In the latter case, the amplified optical noise PSD S_N (in one polarization) is given by $S_N = GF_n h\nu/2$, where F_n is the amplifier noise figure (NF), h is Planck's constant, ν is the optical frequency of the signal light and G is the amplifier gain. The NF describes how much noise is added for any given amplifier. For an ideal EDFA or phase-insensitive parametric amplifier (PIA), the vacuum fluctuation-limited NF=2 (3 dB), while an ideal phase sensitive amplifier (PSA) can achieve NF=1 (0 dB). The 0 dB NF of PSAs will be elaborated further on in chapter 5.

The cause for added noise from an optical amplifier is explained by the vacuum fluctuations that permeates the universe. Vacuum fluctuations can be seen as a virtual electromagnetic field with a PSD of $h\nu/2$ originating from Heisenberg's uncertainty principle and is core to quantum mechanics. Vacuum fluctuations cannot excite electron-hole pairs in photo-detection, but they can trigger stimulated emission in an erbium doped fiber amplifier (EDFA) as well as stimulate nonlinear-interaction in parametric optical amplifiers like the PSA, thus giving rise to optical

noise. Hence the amplified optical noise from an amplifier is typically denoted as amplified spontaneous emission noise (ASE) in the context of EDFAs or as amplified vacuum noise (AVN) in the context of parametric amplifiers. As vacuum fluctuations stimulates both processes, we will maintain the AVN-notation in this thesis.

Using the above variances for the stated (approximately) normal-distributed noises the SNR of the recovered signal is given as

$$\mathrm{SNR} = \frac{R_d^2 P_o^2}{\sigma_s^2 + \sigma_T^2 + \sigma_{\text{S-N}}^2 + \sigma_{\text{N-N}}^2}, \quad P_o^2 = \begin{cases} P_s^2, & \text{incoherent detection} \\ P_s P_{\text{LO}}, & \text{coherent detection,} \end{cases} \tag{2.7}$$

where P_s is the optical signal power and P_{LO} the LO power.

Different noise sources will dominate the total noise power depending on the reception. For sensitive free-space SN-SPD-based direct-detection without stray light and optical amplification, only shot noise and thermal noise are present, with the thermal noise being dominant at low received powers. To maintain high SNR in this case, the SN-SPD is typically cooled down to a few Kelvin to eliminate the thermal noise. At low photon arrival rates the SNR is then dictated by the Poissonian shot noise photon-arrival statistics.

In the case of coherent detection, both amplifier gain and a strong LO help boost the signal power to an extent where thermal noise and shot noise is negligible and provided the use of an optical filter, the noise-noise beating is also limited. This leaves the signal-noise beating dominant and we get $\mathrm{SNR} = 2P_s/F_n h\nu\Delta f$.

2.3.2 Channel compensation

In addition to the noise sources discussed above there are other detrimental effects imposed on the signal by the communication channel itself. Free-running frequency drifts and phase noise of signal and LO lasers will cause a time-varying phase-rotation of the received symbols in a coherent receiver. Indeed, practical lasers have a finite spectral distribution, often modelled using a Lorentzian shape (see Fig. 2.13) with associated FWHM

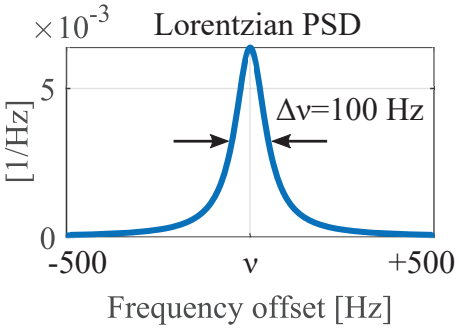

Figure 2.13: A Lorentzian laser line-shape with a full width-half maximum (FWHM) linewidth of $\Delta\nu = 100$ Hz.

linewidth $\Delta\nu$ centered at the nominal emission frequency $\nu = \nu(t)$ which drifts randomly in time.

Turbulence induced power and phase fluctuations or receiver misalignment may likewise affect the received symbol shape. These effects differ from the aforementioned noise in that they can be fully or partially compensated in digital domain using digital signal processing (DSP) in the receiver. This compensation is possible since the detrimental effects are either deterministic (like the Doppler shift), or bandwidth-limited well below the signal bandwidth. This allows the signal to probe the channel with high-enough SNR ($\propto 1/\text{bandwidth}$) to accurately measure and thus cancel such detrimental channel effects in all instances where the SNR is high enough to also detect the transmitted data. Thus, if SNR is reduced to the extent where the characteristic channel bandwidth is no longer recovered, the data communication breaks down as well.

2.3.3 Data recovery

After channel compensation is applied to the raw digitized signal, the now noisy transmitted symbols are recovered. Fig. 2.14 shows an example of recovered BPSK-symbols with added white Gaussian noise of SNR = 10 in the left and the corresponding normal distributions of either symbol is shown in the right. The optimum symbol-decision threshold for the symmetric modulation format BPSK conveniently follows the imaginary axis (red line). Any recovered symbol to the left of the axis is interpreted as a 0 and any symbol to the right of the axis is interpreted as a 1.

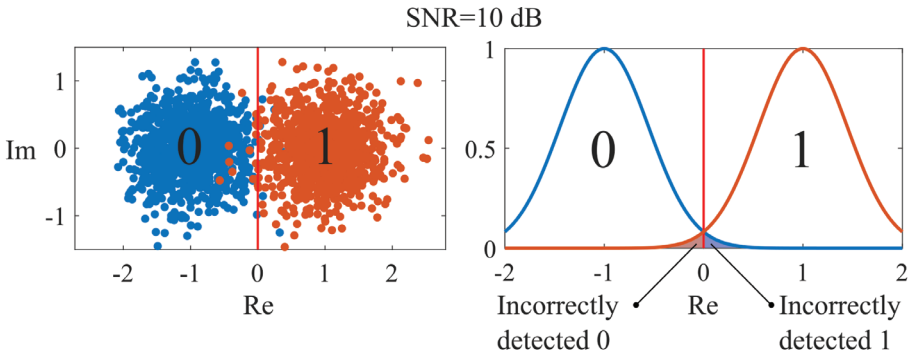

Figure 2.14: Left: the recovered symbols (dots) with white Gaussian noise and 10 dB SNR. Blue dots represent transmitted 0-symbols and orange dots 1-symbols. Right: corresponding probability distributions along the real axis for a 0-symbol (blue) and 1-symbol (orange). Dark areas indicate probability of errors.

From the figure we note that some of the 0-dots ended up on the wrong side and are incorrectly interpreted as 1s and vice-versa for some of the 1-dots. These symbols contribute to the bit error rate (BER) of the received signal which for an error-free communication channel must remain zero. The BER of BPSK is found by integrating the indicated tail-ends of the two symbol distributions of Fig. 2.14 and dividing by the integrals of the total distributions. The result becomes

$$\mathrm{BER} = \frac{1}{2}\mathrm{erfc}\left(\sqrt{\frac{\mathrm{SNR}}{M'}}\right), \quad \mathrm{erfc}(x) = \frac{2}{\sqrt{\pi}}\int_x^\infty e^{-t^2}dt \tag{2.8}$$

which applies both to BPSK and QPSK with $M' = 1$ and $M' = 2$ respectively, as $M' = \log_2(M)$.

As an example, for pre-amplified coherent reception of BPSK (SNR= $2P_s/F_n h\nu\Delta f$), with $\Delta f = 10$ GHz and two different NF (e.g. an ideal PSA and EDFA), the BER vs. received power P_r is shown in Fig. 2.15.

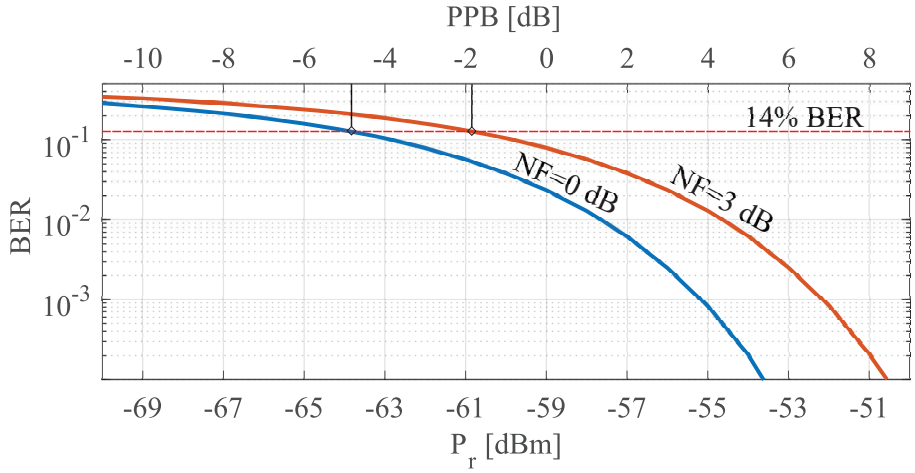

Figure 2.15: BER vs. received power in dBm and photons per bit (PPB).

2.3.4 Sensitivity

The receiver sensitivity is defined as the lowest power (or energy per bit) for which error-free reception is achieved. Commonly, the energy per bit is represented by photons per bit PPB as : PPB= $P_s/h\nu\Delta f M'$. For the powers indicated in Fig. 2.15 there is no error-free reception for the system as described up to this point. To achieve error-free reception even at very low powers one can employ forward error correction forward error correction (FEC) codes. The use of FEC introduces specific bit-coding in the transmitted data, that is, pre-determined sequences of bits that the

receiver knows where and when to expect. Although the introduction of such bit-sequences reduces the allocation of the actual information to be transmitted, this significantly aids the DSP and is necessary in low-power communications. For instance, when allocating 50% of the bit sequence to FEC, i.e a 100% overhead, near-error-free reception can be achieved for pre-FEC BER-values $< 14\%$ in the case of BPSK (and QPSK). In Fig. 2.15 this corresponds to all BERs below the dashed red line, or all powers above -64.3 dBm (-5.3 dB PPB) and -61.3 dBm (-2.3 dB PPB) for the 0 dB NF and 3 dB NF-curve respectively. These threshold powers now represent the receiver sensitivity for the two curves in Fig. 2.15. Note that there is a distinction between PPB and photons per information bit (PPIB), especially when considering FEC as in the 100% overhead case, where the sensitivity in terms of PPIB is 2PPB.

Theoretical best sensitivity vs. spectral efficiency (bits/s per used signal bandwidth in Hz) have been derived both for coherent receivers with modulation formats such as BPSK and QPSK as well as for direct detection PPM. Instead of reviewing the exact expressions here they are instead visualized in Fig. 2.16 (based on [34]).

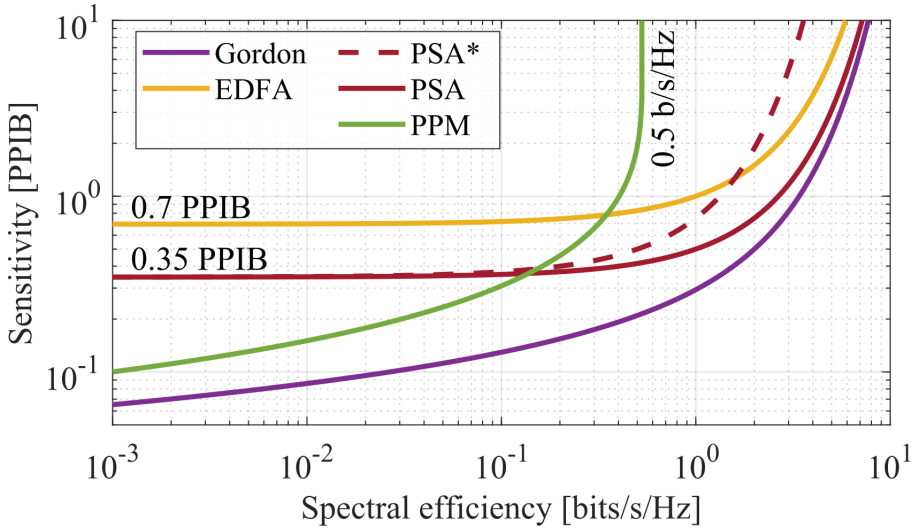

Figure 2.16: Theoretical sensitivities vs. spectral efficiency for different coherent EDFA and PSA reception as well direct detection PPM. Gordon represents the lowest possible sensitivity regardless of receiver type. The solid PSA curve does not account for the idler wave optical bandwidth occupancy in the spectral efficiency while the dashed does. The idler is not detected in the receiver.

The purple curve is the ultimate sensitivity limit as described by Gordon in [50]. Meanwhile, PPM can achieve arbitrarily low sensitivities in theory but has an upper spectral efficiency bound of 0.5 b/s/Hz. In

contrast, EDFA and PSA pre-amplifed coherent reception can in theory achieve arbitrarily high spectral efficiency but are bounded by 0.7 PPIB and 0.35 PPIB respectively in terms of sensitivity. Clearly, above some threshold sensitivity, coherent reception can provide much higher data rates than PPM and among coherent receivers, the PSA pre-amplified one enables the highest spectral efficiency at lowest power.

Indeed, by converting spectral efficiency to data rate (multiplying with a signal/detector bandwidth) and converting the sensitivity to communication reach via Eq. (2.1) (with specific parameters), one can produce a reach vs. data rate plot such as Fig. 1.3 in chapter 1. For the purpose of free-space optical communications Fig. 1.3 provides a more relevant comparison and illustrates the benefit of coherent and in particular the PSA in a direct manner. Here, the PSA enjoys a $\sqrt{2}$ times longer reach than the EDFA, or a 2 times higher data rate. Furthermore, the reach is proportional to receiver size D_{Rx} for all curves. Hence, by leveraging a larger receive-area such that the link distance falls into reach of the PSA, where its data-rate surpasses that of PPM, high speed communication can be established for a given deep space mission.

CHAPTER 3

The dither-optical phase-locked loop

In section 2.3.2 we discussed the necessity to correct for certain channel effects to recover an optical signal. There, a focus on digital compensation was emphasized. However, there are instances in which signal distortions accumulated through the channel must be compensated already in the optical domain. For the purposes of both large area coherent reception, as well as phase sensitive amplifier (PSA)-implementation, this is the case and here, the optical phase locked loop (OPLL) plays a core component.

In the investigated multi-aperture and multi-mode fiber (MMF)-reception solutions for larger receivers in this thesis (discussed further in chapter 4), the coherent combining of individual signal channels requires phase-locking. Likewise for PSAs, the pump wave created at the receiver must be locked in phase to the received signal (and idler) wave to achieve phase-sensitive amplification. In either application, the requirement of zero phase and/or frequency offset excludes the use of frequency offset-locking OPLLs [51]. The alternative of optical injection-locking (OIL) is furthermore not compatible with typical data-modulated signals and would require an accompanying continuous wave (CW) reference wave, something that has been used in the context of PSAs [26] but which remains undesirable. Instead, a convenient solution to zero-offset phase/frequency locking is presented by the dither-OPLL [52].

The dither-OPLL was first investigated for the purpose of local os-

cillator (LO)-laser phase-locking to a received optical communication signal in order to enable optical homodyne reception. Without optical pre-amplification, homodyning can in principle achieve the same sensitivity as a PSA, however, this requires a 100% photo-detector quantum efficiency which is never seen in practice. Although the dither-OPLL could correct phase and frequency offsets between signal and LO, the added complexity of an OPLL was easily replaced by compensation post detection using digital signal processing (DSP).

Despite the modest interest in the dither-OPLL during the past years, its unique property of achieving zero-offset locking without the need for a CW wave lend itself perfectly for the situations investigated in this thesis. Its operation and performance characteristics are described in this chapter.

3.1 Example setup

Though the dither-OPLL can be fashioned into various system configurations we will here consider a relatively simple system that connects well with the topics in this thesis. Consider the system depicted in Fig.3.1, initially neglecting the shaded laser-part. Here, two input optical waves guided by their respective single mode fibers (SMFs) experience a time-varying relative phase $\phi = \phi(t)$. After further propagating the waves, the lower wave attains an extra phase shift ϕ_c via an optical phase-modulator (ϕ_c-mod) before they are both interfered in a 50/50-directional coupler. The optical power in either wave is P_s and the power P_d is determined by the new relative phase $\phi - \phi_c$ as

$$P_d = P_s[1 - \cos(\phi - \phi_c)]. \tag{3.1}$$

In this example, we want to lock the relative phase between the waves by minimising P_d, i.e. when $\phi = \phi_c$. This is achieved by detecting the power P_d and from this information, adjust ϕ_c using a control system to cancel the relative phase. The control of ϕ_c makes this a 1st order OPLL.

Although the described system in principle can compensate for any phase variation ϕ, in case the two input waves originate from separate and uncorrelated lasers, variations in ϕ typically become too fast for any practical control system to adjust for. This is representative of the case of laser-locking, i.e., when one wish to lock a laser to a reference-laser, thus making them correlated. To achieve both phase and frequency-locking

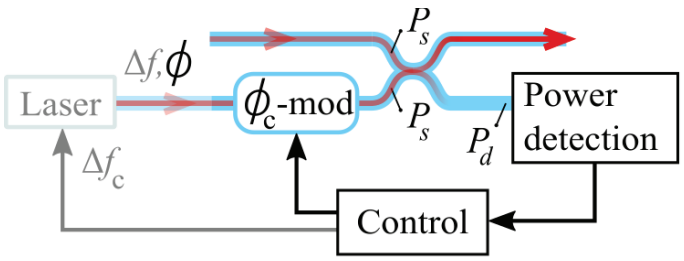

Figure 3.1: Schematic of an OPLL-setup for phase locking, or phase-frequency locking when including the shaded part.

in this example, we assume a free-running relative frequency drift $\Delta f = \Delta f(t)$ and that we have access to and control of the frequency of the laser creating the lower wave (the shaded part in Fig.3.1). Now the locking can be achieved by compensating Δf using Δf_c. Note that frequency is just the time-derivative of phase, hence frequency is incorporated in $\phi - \phi_c$ and Eq.(3.1) still applies. The control of ϕ_c both via ϕ_c-mod and Δf_c makes this a 2nd order OPLL.

3.2 OPLL in time domain

Assuming a digital phase control with discrete update time Δt, a phase error $\phi_e(t) = \phi(t) - \phi_c(t)$ at time $t = n\Delta t$ (n being an integer) is compensated at $t = (n+1)\Delta t$ if ϕ_c is updated as $\phi_c([n+1]\Delta t) = \phi_c(n\Delta t) + \phi_e(n\Delta t)$ assuming ϕ varies negligibly during a time Δt. To update ϕ_c according to this equation requires information of ϕ_e, both its magnitude and sign. From measurement of P_d and knowledge of P_s one can extract $|\phi_e|$ but not its sign. To overcome this, an additional phase signal in the shape of a sinusoidal modulation $\phi_d(t) = \phi_{\text{mag}} \cos(2\pi f_d t)$ with magnitude ϕ_{mag} and frequency f_d is added in ϕ_c-mod. This is called a phase-dither. Via dithering, the sign of ϕ_e can be extracted as illustrated in Fig.3.2a).

For a small dither magnitude $\phi_d \ll \pi$, the phase dither is converted into a power-oscillation P_e proportional to $d(\cos\phi_e)/dt = \sin\phi_e$ which is $\propto \phi_e$ for small phase errors. Hence, by demodulating the detected P_d as $P_d \cdot \cos(2\pi f_d t)$ and low-pass filtering, a baseband signal proportional to ϕ_e is obtained. Note that this concept relies on the phase variation $d\phi/dt$ being negligible during the dither cycle $1/f_d$ for accurate recovery of ϕ_e. In general, the recovered base-band signal can be written as $s = s_e + s_n$ where $s_e \propto \phi_e$ is the error signal and s_n is the system noise.

With the phase error contained in the base-band signal s we can write

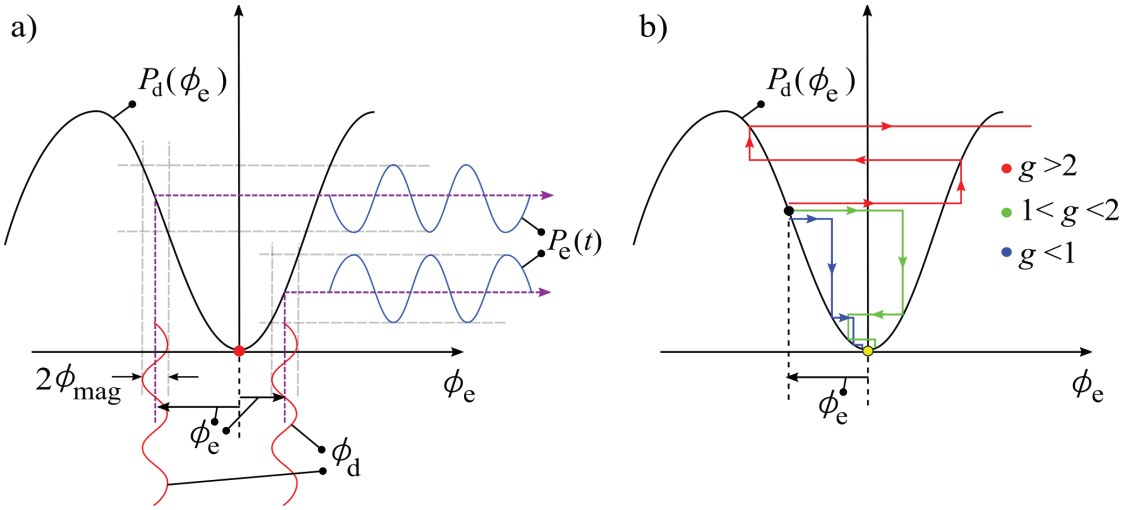

Figure 3.2: a) Illustration of the power oscillation in P_d vs. ϕ_e generated via phase dithering. b) Illustration of loop convergence for different step gains g.

the new control phase update as

$$\phi_c([n+1]\Delta t) = \phi_c(n\Delta t) + g \cdot [\phi_e(n\Delta t - \tau) + \phi_n(n\Delta t)] \tag{3.2}$$

where ϕ_n is an added phase noise from the OPLL system noise s_n, τ is the loop delay and g is a the step-factor that incorporates all gain and conversion factors and is tuneable to optimize the OPLL. The importance of the step-factor tuning is illustrated in Fig.3.2b) which shows the phase error convergence towards zero for $g < 2$ and unbound divergence in the case of $g > 2$ (assuming $\tau = 0$ and $\phi_n = 0$). Evident is the importance of g concerning the convergence speed, i.e. how quickly the OPLL can track the phase variation $\phi(t)$ as well as concerning loop stability.

The scenario discussed so far is fairly ideal. For instance, in the case where the power P_s fluctuates rapidly in time, e.g. from atmospheric scintillation, this could jeopardize the stability of the OPLL as g is directly proportional to P_s. A way to circumvent this problem is to use the following update equation

$$\phi_c([n+1]\Delta t) = \phi_c(n\Delta t) + g_s \cdot \mathrm{sgn}([\phi_e(n\Delta t - \tau) + \phi_n(n\Delta t)]) \tag{3.3}$$

where g_s represents a static step-gain and $\mathrm{sgn}(x)$ is the sign-function. This type of update equation refers to a category of phase locked loops (PLLs) referred to as Bang-bang PLLs. For small step-gains g_s and a well-performing control system, i.e. when ϕ_e is small, the Bang-bang PLL behaves as a linear PLL like in Eq.3.2 [53] but where any magnitude fluctuations in s_e are conveniently removed.

In terms of the frequency compensation $f_c(t)$, the same update equation as for ϕ_c is used, where ϕ_c is exchanged for Δf_c and a separate step-factor is defined g_f. The continuous time model for both the 1st and 2nd order loops is thus given by

$$\phi_c(t) = k_\phi \int_0^t \phi_e(t' - \tau)dt' + 2\pi \int_0^t \left(k_f \int_0^{t'} \phi_e(t'' - \tau)dt'' \right) dt' \quad (3.4)$$

where ϕ_n is neglected and k_ϕ and k_f are the continuous time loop gains corresponding to g and g_f respectively ($k_f = 0$ for 1st order loop). The first term represents the first-order response, i.e. a direct phase compensation. Meanwhile the large parenthesis in term two is $\Delta f_c(t')$ and the outer integral converts its influence to phase, being the second order response. Note how both control signals ϕ_c and Δf_c are generated using integrals. In terms of a PID-controller, where P is proportional, I is integral and D is derivative gain respectively, the dither-OPLL consists of a phase and frequency integrator. However, observe that the first term in Eq.3.4 could be realized also without ϕ_c-mod, by instead applying a proportional gain in the laser frequency control. This can be more practical in some cases.

3.2.1 1st order control loop

The behaviour of OPLLs can many times be confusing and difficult to interpret. Here we discuss some typical scenarios that highlights the challenges, depicted in Fig.3.3, for phase control in a 1st order loop. In the figure, both ϕ and ϕ_c are plotted vs. time as well as their phase error difference ϕ_e with corresponding standard deviation σ_{ϕ_e}.

In the top is shown a well-performing phase-tracking system where detrimental effects such as system noise and loop delay are negligible, resulting in a low σ_{ϕ_e} of 4 degrees. Here, ϕ_c matches ϕ almost perfectly.

In the row beneath, two plots are compared. Both feature a low SNR of 2 ($s_e \sim s_n$) but the leftmost one has a 5 times larger step-factor than the rightmost one. It can be seen that the choice of lower step-factor (k_ϕ) in the right results in a lower phase error. As k_ϕ represents the loop gain or bandwidth of the OPLL, a lower bandwidth filters away more of the system noise s_n that would otherwise be transferred to the control phase ϕ_c. This also filters away fast variations in s_e, however, which hampers the system's ability to perfectly match ϕ_c to ϕ as can be seen in the rightmost figure in some instances, where the red curve does not perfectly match the blue one.

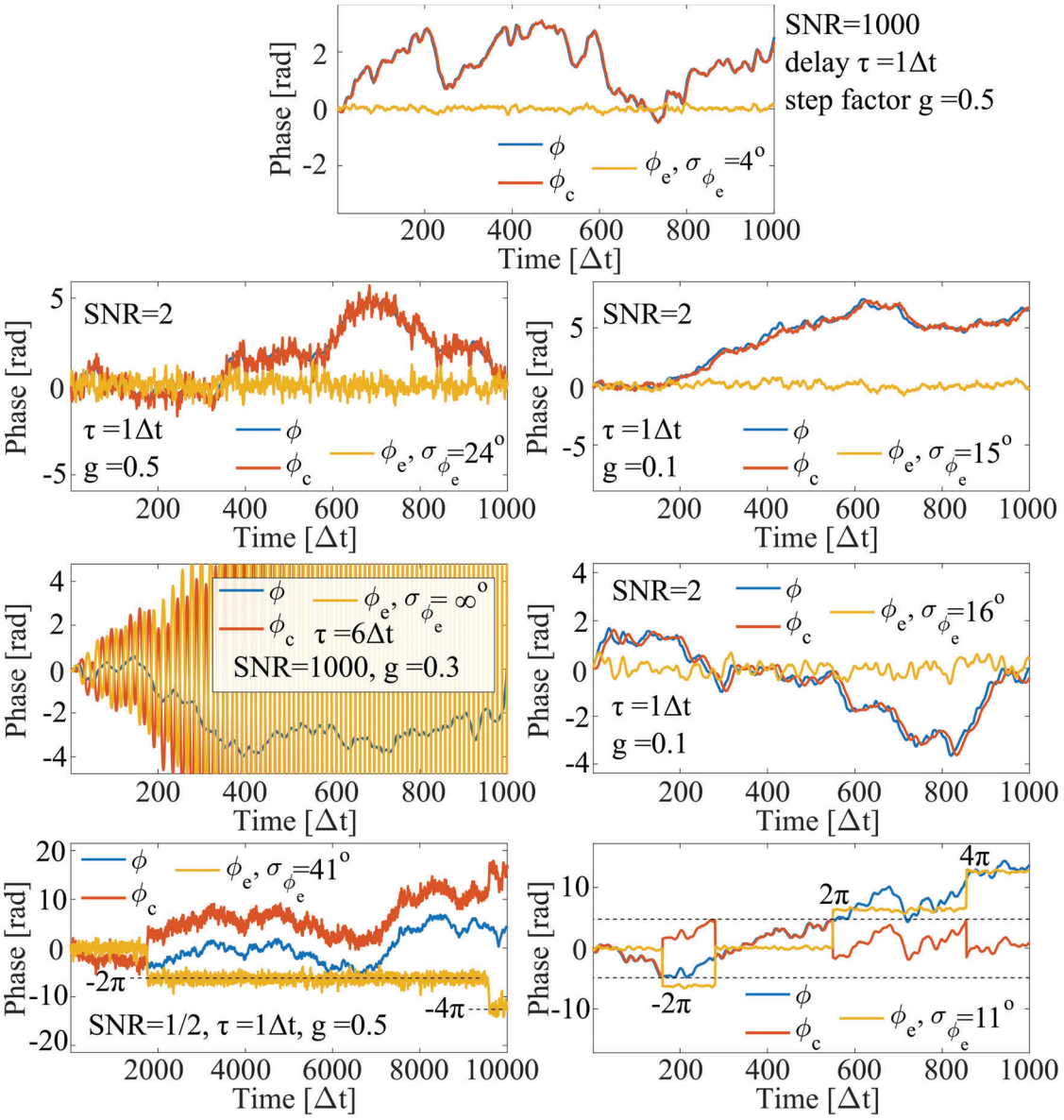

Figure 3.3: Different phase-locking scenarios of a 1st order control loop with varying signal to noise ratio (SNR), loop delay and step-factors. In the bottom right also a maximum phase compensation range is imposed.

Next, in the second row, two plots with high SNR but large loop delay are shown. In the leftmost plot, the loop delay results in an unstable OPLL with unbounded phase error whereas in the rightmost plot, with a 3 times smaller step-factor, stable OPLL-operation with $\sigma_{\phi_e} = 16^o$ is shown. A larger loop delay hence severely affects loop stability. One can see the repeating overshoots of ϕ_c in the left with higher step-factor. Lowering the step factor, as in the right, limits these overshoots and stable phase tracking can be maintained, albeit with delayed and slower

response which ultimately results in a larger phase error than in an ideal case.

In the bottom row we discuss both a fundamental effect present in OPLLs as well as an effect induced by practical implementation. In the leftmost plot we again consider a low SNR scenario but over a longer time. Recalling that the actual error signal is $\propto \sin\phi_e$ we realise that s_e is zero for $\phi_e = m2\pi$ where m is an integer. In the presence of noise and given long enough time, there will come a moment where the noise pushes the phase error close enough to a neighbouring operating point for a transition to take place. For the purposes of phase locking, we usually are fine with static phase-offsets, however, during the moment of transition the system is unlocked which in terms of a communication channel may result in lost bits. The expected time between such phase-slips is derived in [54] and is proportional to $e^{2\mathrm{SNR}}/B_n$ (where B_n is the OPLL noise bandwidth) whereas the slip duration approximately equals the inverse loop bandwidth [55]. Operating at higher SNR thus virtually removes the problem of noise-induced phase slips.

In the bottom right plot we are again presented with phase-slips and operation at neighbouring 2π phase points, however, in this case SNR is high. The phase slips occuring here are instead imposed by physical constraints of the locking system. Specifically for a locking system using a separate phase-modulator ϕ_c-mod. Either the voltage signal to the modulator or the modulator acceptance range is limited, thus enforcing the use of 2π-phase jumps from the control-system side to maintain phase-locking. This scenario suffers likewise as from the noise-induced phase-slips. The frequency of slipping is however dependent on the rate of change in ϕ and the ϕ_c-mod voltage range and the slip duration is limited to that of the control signal bandwidth.

In the scenario of laser-locking, phase control in ϕ_c-mod is easily replaced by proportional frequency control in the laser, as previously mentioned, thus removing the issue of such phase-slips. When phase compensation in ϕ_c-mod is required, however, phase-slips remain a problem that in principle could be solved by the use of an extra phase-modulator as in [56], yet this further complicates the implementation.

3.2.2 2nd order control loop

Although everything that applies to a 1st order loop also does so to a 2nd order loop, there are some additional challenges tied to the simultaneous phase and frequency compensation. Each plot-row in Fig.3.4 represents

a specific scenario, where the leftmost plot shows the phase vs. time similar to Fig.3.3 and the rightmost plot shows the frequencies Δf, Δf_c and $\Delta f - \Delta f_c$ vs. time.

The top row in the figure again shows a well performing system with high SNR and short loop delay. Here both phase and frequency are compensated near perfectly.

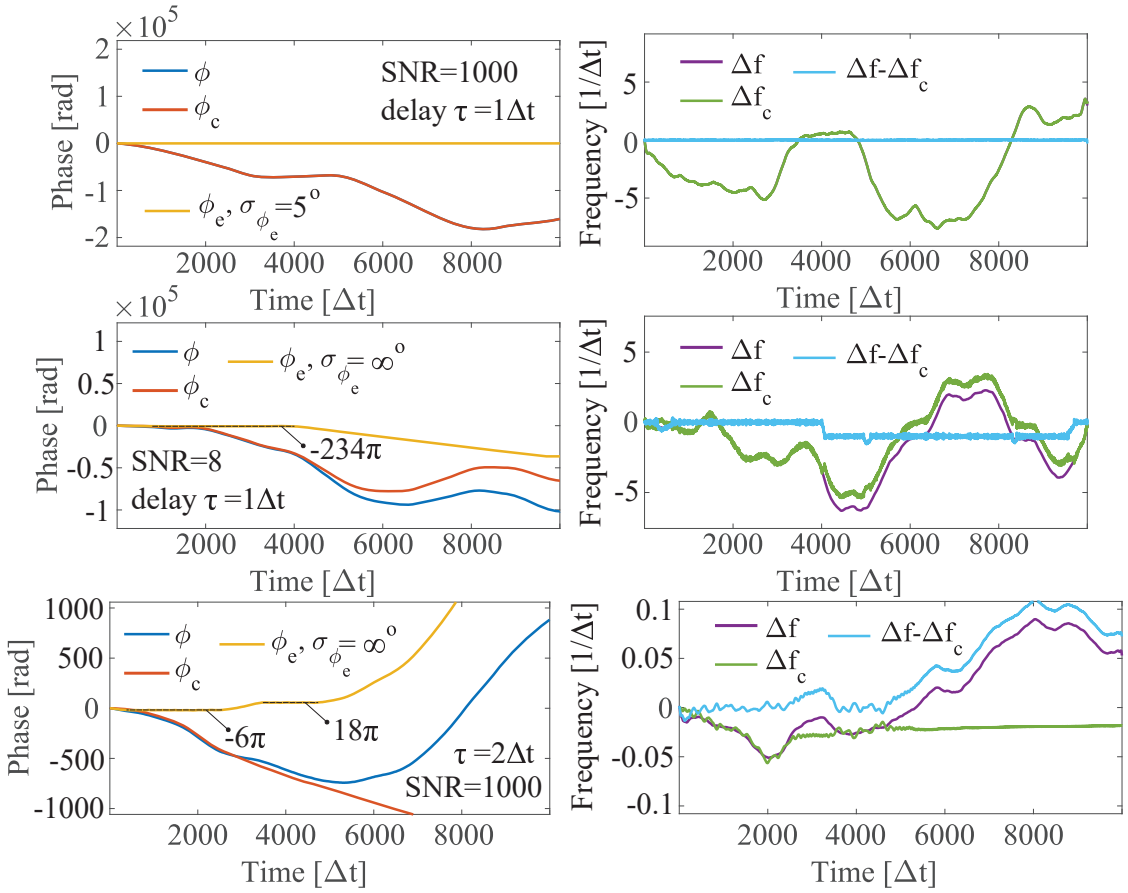

Figure 3.4: Different phase-locking scenarios of a 2nd order control loop with varying SNR and loop delay. Both phase vs. time and frequency vs. time are shown.

In the second row the SNR is much lower. Here the system goes from an initial zero phase error and momentarily locks at -234π before at a later point, losing lock again. What complicates the laser locking case is the free-running relative frequency drift Δf. Remember that the operation of the OPLL assumes that the phase variations occur with a frequency much lower than f_d. If a disturbance such as noise pushes the frequency compensation off keel such that $\Delta f - \Delta f_c \ll f_d$ then locking is lost and may not be recovered again unless the system happen to drift back to the operating point or if a nearby Phd-student intervenes by man-

ually turning the current-control knob of the laser. The right plot in this case shows an apparent stable offset frequency-lock at $\Delta f - \Delta f_c = 1/\Delta t$ which happens to average out the phase error to zero for the given simulation in which $\Delta t = 1/f_d$. For certain loop-gain combinations the lock at such offset-points remained more stable than the desired operating point, removing any prospect of the frequency naturally drifting back to $\Delta f - \Delta f_c = 0$.

In the bottom row the SNR is again high but the loop delay longer. Here moments of stable locking are experienced before the system again unlocks. As for low SNR, a long loop delay is detrimental to the OPLL stability and easily causes the system to unlock. A combination of both low SNR and significant loop delay is especially problematic for the operation of a laser-locking system.

The loop dynamics regarding probability of unlocking-events and expected time of locking are important for the practical implementation of an OPLL, however, these aspects are not investigated here and remain outside the scope of this thesis. Instead focus is put toward the optimisation and performance of the OPLL during locking.

3.3 Optimising the dither-OPLL

In an ideal OPLL the phase should be perfectly compensated and $\sigma_{\phi_e} = 0$, hence optimisation of the OPLL targets the minimisation of the residual phase error ϕ_e. This implies that for a given phase variation ϕ and received power P_s, the OPLL parameters k_ϕ, k_f and ϕ_{mag} should be optimised. The dither frequency f_d has no impact as long as it remains much larger than the bandwidth of ϕ.

In order to optimise, a relation between σ_{ϕ_e} and the aforementioned variables is required. For the dither-OPLL, this is easily developed in the frequency domain.

3.3.1 OPLL in frequency domain

The operation of the OPLL can be condensed into the block-diagram of Fig.3.5. Here, $\phi_e = \phi - \phi_c$ as previously while ϕ_c is driven by ϕ_e with corresponding phase-error specific gain K_e and system noise n through the common open-loop transfer function H_c. To avoid pesky differential equations and the use of

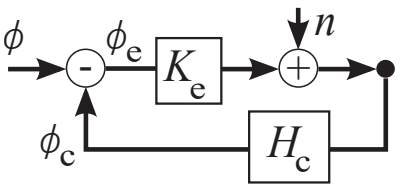

Figure 3.5: OPLL block-diagram.

impulse-responses in favour of transfer functions, we Laplace-transform the block-diagram relations to obtain

$$\Phi_e(s) = H_\phi(s)\Phi(s) + H_n(s)N(s) \tag{3.5}$$

where $s = j2\pi f$, j is the imaginary number, f is frequency, Φ_e, Φ and N are the Laplace transformed ϕ_e, ϕ and n respectively and H_ϕ and H_n are the phase and noise transfer functions given by $\Phi_e(s)/\Phi(s)$ and $\Phi_e(s)/N(s)$, respectively. From the following relations, discerned from the block diagram,

$$\Phi_e(s) = \Phi(s) - K_e H_c(s)\Phi_e(s) \tag{3.6}$$

and

$$\Phi_e(s) = -H_c(s)[N(s) + K_e\Phi_e(s)], \tag{3.7}$$

the transfer functions H_ϕ and H_n are obtained via some simple algebraic manipulations as

$$H_\phi(s) = \frac{1}{1 + K_e H_c(s)}, \quad H_n(s) = -\frac{H_c(s)}{1 + K_e H_c(s)}. \tag{3.8}$$

The common open loop transfer function is meanwhile obtained by Laplace-transforming Eq.(3.4) as

$$K_e H_c(s) = k_\phi \frac{e^{-\tau s}}{s} + 2\pi k_f \frac{e^{-\tau s}}{s^2}. \tag{3.9}$$

The contributions to the phase error variance $\sigma^2_{\phi_e}$ from phase ϕ and noise n can be computed by integrating the power spectral densities (PSDs) of ϕ (S_ϕ) and n (S_n) multiplied with their corresponding transfer functions

$$\sigma^2_\phi = \int_0^\infty S_\phi(f)|H_\phi(j2\pi f)|^2 df, \quad \sigma^2_N = \int_0^\infty S_n(f)|H_n(j2\pi f)|^2 df. \tag{3.10}$$

Usually, but not always (see paper [C]), the phase dithering itself also constitutes a phase-error contribution and is given by $\sigma^2_{\phi_d} = \phi^2_{\text{mag}}/2$. As all mentioned contributors are typically uncorrelated, the variances can simply be added to obtain the final phase error variance $\sigma^2_{\phi_e} = \sigma^2_\phi + \sigma^2_N + \sigma^2_{\phi_d}$.

To illustrate the effect of the transfer functions, let us assume a 1st order loop $k_f = 0$ with zero loop delay for which $|H_\phi|^2 = (2\pi f)^2/[(2\pi f)^2 +$

$k_\phi^2]$ behaves as a high-pass filter and $|K_e H_n|^2 = k_\phi^2/[(2\pi f)^2 + k_\phi^2]$ behaves as a low-pass filter. Fig.3.6 shows how a $f^{-8/3}$ phase-PSD and white noise PSD are filtered by their respective filters at different $B = k_\phi/2\pi$. The top right plot shows the residual phase error standard deviation vs. B, neglecting the dither, as $\sigma_{\phi_e}^2 = \sigma_\phi^2 + \sigma_N^2$.

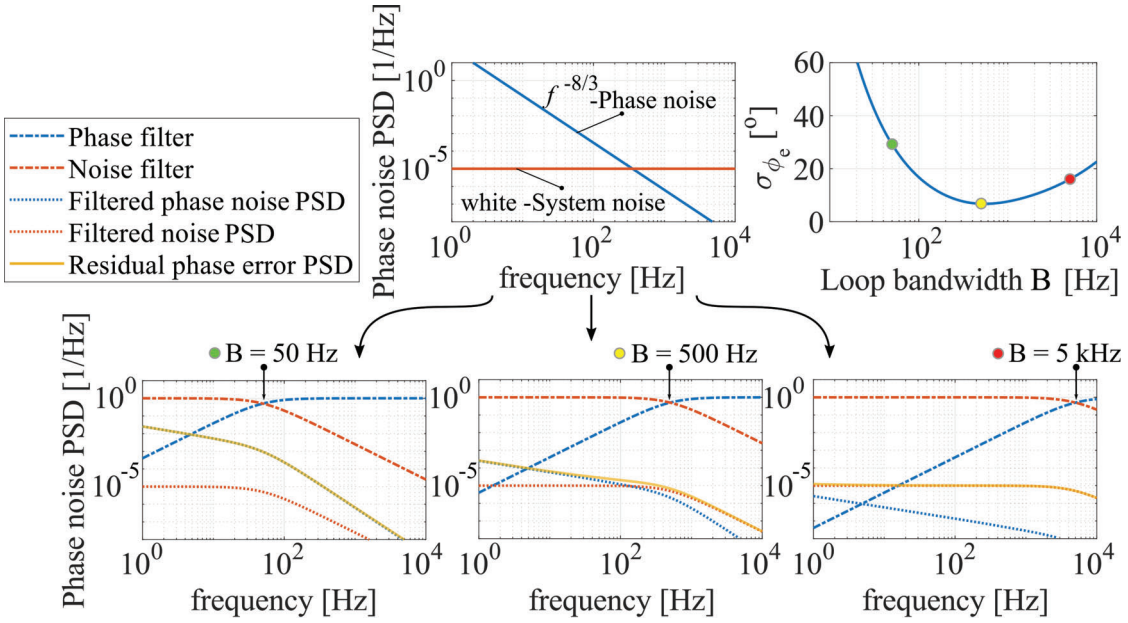

Figure 3.6: Visualization of phase and system noise suppression using corresponding loop filters. Center top: input noise PSDs. Bottom row: The resulting filtered system and phase noise PSDs at different loop bandwidth B. Top right: residual phase error deviation vs. B.

From these plots we see clearly how the optimal choice of B (k_ϕ) is a compromise between filtering away as much phase noise S_ϕ as possible or as much system noise S_n as possible. This constitutes a fundamental trade-off between SNR and bandwidth, similar to that of an optical communication link.

The graphical representation in Fig.3.6 can also be made clear from the equations. Optimal OPLL parameters are found by solving the following system of equations

$$\frac{d\sigma_{\phi_e}^2}{d\phi_{\text{mag}}} = 0, \quad \frac{d\sigma_{\phi_e}^2}{dk_\phi} = 0, \quad \frac{d\sigma_{\phi_e}^2}{dk_f} = 0 \tag{3.11}$$

for which the minimum phase error standard deviation is obtained. Analytical derivation of Eq. (3.11) requires a simple model of $S_\phi(f)$. For simulated S_ϕ (as in paper [B]) or measured S_ϕ (as in paper [C,D]), numerical optimization can be used instead, where in this thesis a grid

search was commonly employed. However, to provide an example, here we assume a 1st order loop ($k_f = 0$), a Lorentzian phase noise PSD $S_\phi \simeq 2\Delta\nu/\pi f^2$ (single-sided with linewidth $\Delta\nu$) and incoherent power detection $K_e \approx \phi_{\text{mag}} P_s/2$ ($\phi_{\text{mag}} \ll \pi$) which gives

$$\sigma_\phi^2 = \frac{2\pi\Delta\nu}{k_\phi}, \quad \sigma_N^2 = \frac{S_n k_\phi}{(\phi_{\text{mag}} P_s)^2}, \quad \sigma_{\phi_d}^2 = \frac{\phi_{\text{mag}}^2}{2}. \tag{3.12}$$

Again, Eq. (3.12) illustrates the trade-off between minimizing σ_ϕ^2 vs. σ_N^2 via the loop bandwidth k_ϕ similar to Fig. 3.6. Another trade-off exists between σ_N^2 and $\sigma_{\phi_d}^2$ through the dither magnitude ϕ_{mag} which can be increased to boost the OPLL SNR ($\text{SNR}_{\text{OPLL}} \equiv 1/\sigma_N^2$) at a price of a larger dither penalty $\sigma_{\phi_d}^2$. The ability to tune ϕ_{mag} is one of the main merits of the dither-OPLL, which emphasizes its usefulness in low SNR scenarios.

By solving Eq. (3.11) for the optimized k_ϕ and ϕ_{mag} with $\sigma_{\phi_e}^2$ given by Eq. (3.12), the minimized phase error variance is found as

$$\sigma_{\phi_e}^2 = 3\Big[\frac{\pi\Delta\nu S_n}{P_s^2}\Big]^{1/3} = 3\Big[\frac{1}{\text{SNR}_{\text{OPLL}}}\Big]^{1/3}. \tag{3.13}$$

This final expression highlights the fundamental limitation to the dither-OPLL performance imposed by limited signal power P_s and the optimized system noise power ($\pi\Delta\nu S_n$), where the noise PSD S_n is set by the power detection scheme (e.g. any of the variances in section 2.3.1) and the bandwidth $\pi\Delta\nu$ is set by the phase noise PSD. The expression implies that to achieve similar OPLL performance when the bandwidth of phase noise increases, the received power must also increase (assuming S_n fixed). This is the same as saying: there exist a minimum received power, i.e. locking sensitivity, to operate below a certain $\sigma_{\phi_e}^2$ for a given phase noise bandwidth.

Although we assumed a specific phase noise PSD in this example, the conclusions listed here apply also in general for the different kinds of phase noise covered in this thesis. In this example, S_n can be obtained by dividing any of the noise variances in section 2.3.1 by $R_d^2 G^2 \Delta f$ where G is the optical preamplifier gain (if applicable). For coherent detection, $P_s \to \sqrt{P_s P_{\text{LO}}}$ in K_e with P_{LO} being the LO power.

3.4 Phase error statistics

Although the phase error standard deviation is central to the dither-OPLL optimization and provides a simple estimate of its performance,

it does not convey information about temporal, spectral or phase error probability distribution characteristics. In this chapter, we have seen examples of simulated temporal phase error traces in Fig. 3.3 (yellow curves) and spectral distributions in 3.6 (yellow curves). In paper [C] these characteristics are also investigated experimentally in a laser-locking dither-OPLL, alongside other performance metrics. While different metrics are important for different applications, in the context of optical communications, the bit error rate (BER) depends primarily on the phase error probability distribution for the situations covered in this thesis, as will be discussed in chapters 4 and 5.

The phase error probability distribution has been investigated previously in [54] for non dither-OPLLs where it is concluded that the phase error abides a normal distribution when SNR$\gg$ 1, which is mostly the case in this work. This implies that phase error contributions from noise sources such as phase and system noise transfers into normal distributed phase errors and are uniquely characterized by their respective phase error deviations.

Based on the same simulation as Fig. 3.3, examples of simulated phase error distributions (without dither) are shown in the left of Fig. 3.7, where the bandwidth of phase fluctuations was sequentially increased for red and yellow curves. The same result can be obtained when instead sequentially lowering the system SNR. The distributions are indeed normal, something which was verified also in paper [C], experimentally.

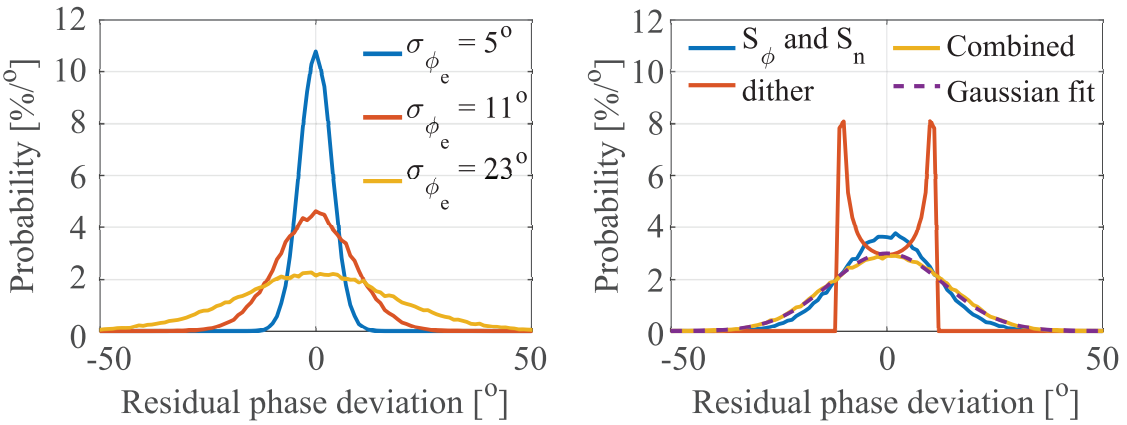

Figure 3.7: Left: phase error distribution from phase and system noise at different standard deviations. Right: phase error distribution resulting from phase and system noise contributions, from the presence of the dither as well as the combined phase noise, including a fitted normal-distribution with the same standard devieation.

For a dither-OPLL with an added phase error contribution from

dithering, the resulting phase error distribution remains normal despite the phase dither not being normally distributed, as can be seen in the right of Fig. 3.7. The original phase error distribution from phase and noise (blue) is broadened (yellow) by adding the phase dither with distribution shown in red. The Gaussian fit uses the combined σ_{ϕ_e} from the three contributions as standard deviation. Hence, phase error distributions for dither-OPLLs may also be uniquely described by the phase error standard deviation and corresponding normal distribution.

CHAPTER 4

Large receiver area for coherent reception

In chapter 2 we discussed how a large receiver aperture size (denoted as D in this chapter) alongside efficient receive-optics (η_r) is necessary to collect enough power for sensitive free-space optical communication links. We also discussed how coupling the light from a large aperture into a single-mode receiver faces several practical challenges in a space to ground link. These included stringent alignment tolerances as well as turbulence-induced angle of arrival (AOA) fluctuations and spatial phase perturbations, all of which must be overcome to enable sensitive, optically pre-amplified coherent detection.

This chapter introduces the three main approaches for large-area single-mode coupled receivers that overcome these challenges; adaptive optics (AO) [57], multi-mode fiber coupling [58] and multi-aperture reception [59]. An overview of the three approaches is illustrated in Fig. 4.1.

Each approach aims to compensate the effects of the free-space channel that limit η_r and cannot be compensated digitally. This involves coarse pointing for transmitter-receiver alignment, tip-tilt compensation of AOA fluctuations and spatial reconstruction of the distorted field. The required active compensation, in turn, relies on the implementation of sophisticated control systems that need to be able to cancel the atmospheric effects at kHz rates [60] while operating at low received powers.

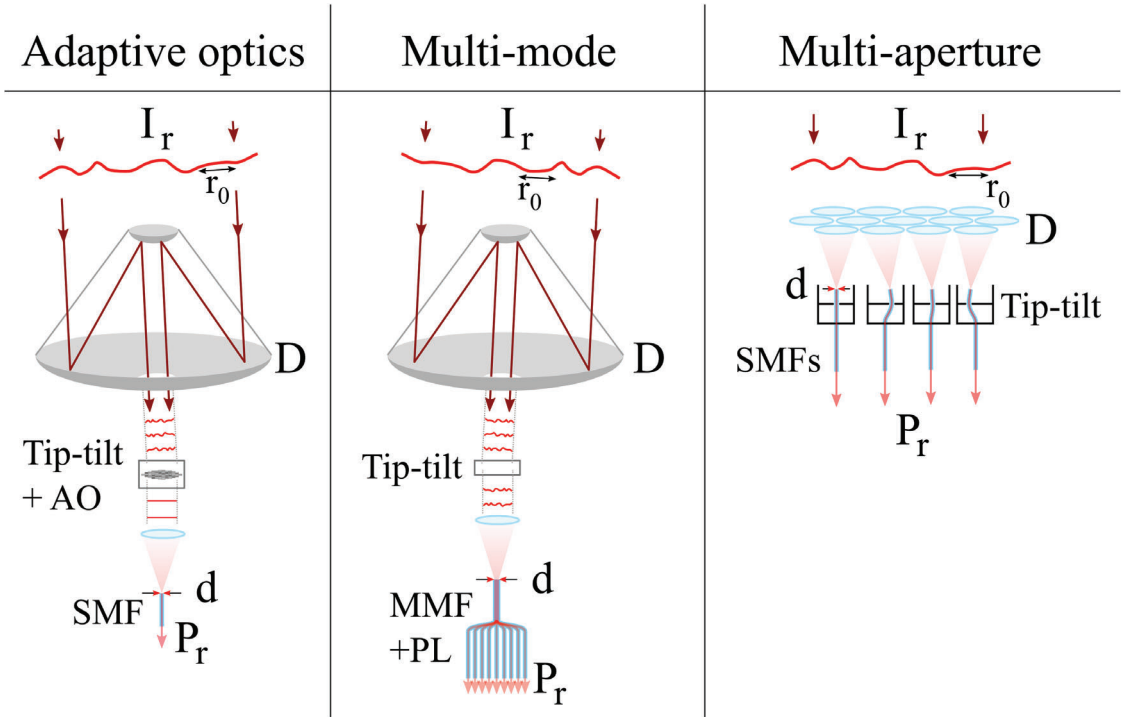

Figure 4.1: Left: single mode fiber (SMF)-coupled large-area receiver with AO turbulence compensation and tip-tilt control. Middle: multi-mode fiber (MMF)-coupled large-area receiver with tip-tilt control and MMF to SMF transformation via a photonic lantern (PL). Right: SMF-coupled multi-aperture array receiver with individual tip-tilt control.

A spatial mode perspective

To understand how the three receiver implementations can undo the effects of the turbulent channel we will look at the atmospheric propagation from a spatial mode perspective. As the transmitted, single spatial mode signal (∼plane wave) enters the atmosphere it is redistributed upon the spatial frequency spectrum while propagated through the channel, with individual spatial components gradually becoming uncorrelated from one another, see Fig. 4.2. In regular spatial domain, these individual spatial components are characterized by the coherence length r_0.

When receiving the field using a finite-sized aperture of diameter D (smaller than the incident beam), we apply a form of spatial filtering which collects a portion of the spatial components. The collected field power (∼ 100% but not all) can be divided into a finite set of uncorrelated orthogonal spatial modes in some discrete basis. The number of spatial

modes that contain $\geq\sim 75\%$ of the collected power can be estimated as

$$N = \left(\frac{D}{r_0}\right)^2 \tag{4.1}$$

i.e. the same as the number of speckles present in the turbulence-limited spot-size we discussed in chapter 2. This is the same as the number of r_0-sized disks that fit inside a D-sized aperture. The received (or incident) power per mode can thus be defines as $P_{r_0} = I_r \pi r_0^2/4$ where I_r is the average incident intensity.

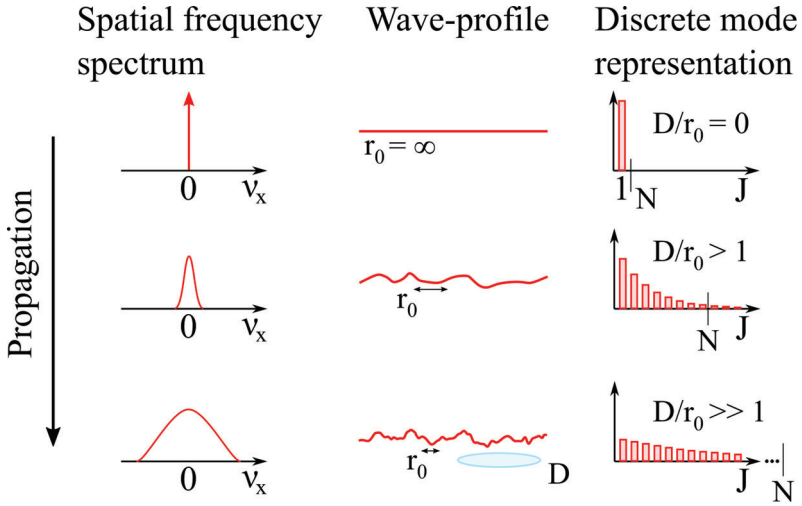

Figure 4.2: Visualization of spatial decomposition of different wave-profiles in different modal basis. The discrete representation in the right column is an example and refers to after spatial filtering using an aperture of size D. J: mode number.

To couple the power contained in the N collected modes into a single mode, each receiver implementation must cancel the turbulence-induced field de-correlation between all the modes. Although the way in which this is achieved differs between the different systems, it will require the equivalent of $N-1$ active control systems. One can achieve higher efficiencies ($> 75\%$) by correcting for a larger number of modes N_c: $N_c > N$, see e.g. Fig. 4.2. However, this leads to a lower average received power per corrected mode ($P_{r_0} \cdot N/N_c$), in turn resulting in a lower average signal to noise ratio (SNR) per control system.

As discussed in chapter 3, a control system generally operates at a trade-off between large bandwidth and high SNR. This is true also here, implying that a certain received power is required per corrected mode for compensation at the bandwidth necessitated by the turbulence. This minimum required power, or system sensitivity, thus limits the number

of modes and, hence, how low powers that can be efficiently received. This, in turn, sets a limit for the ultimate reach and speed of the link. Granted that the system sensitivity is met and that reasonable efficiency is achieved, one can in practice just scale the receive-area A_r until enough power is received ($P_r = I_r A_r \eta_r$) to meet the sensitivity of the communication link.

The objective of each receiver implementation, AO, multi-mode reception and multi-aperture reception, is therefore to enable as high receiver efficiency η_r with as low sensitivity as possible. In the following sections we talk about each approach, their advantages, limits and performance in this context for optical free-space communications.

4.1 Adaptive Optics

AO is a technology that was originally developed for ground-based telescopes to improve atmospheric seeing for optical astronomy [57]. For astronomy, large telescopes are needed to reduce the diffraction-limited spot size to improve angular resolution, something which is crucial in order to resolve distant objects. At an ideal observatory, a plane wave incident on the atmosphere should remain a plane wave when imaged on a camera focal plane array (FPA) to reach the diffraction limit.

The objective of AO for astronomy extends beyond that of a free-space optical link in that turbulence-compensation is necessary for a larger range of spatial frequencies and wavelengths to capture a wider field of view and spectral range [57]. Instead sensitive optical communication links through the atmosphere are concerned with correction for one direction and wavelength only. However, the required performance of this correction for coupling into SMF is high, leading to slightly different targets for the two applications. Nonetheless, with maturing AO technologies from decades worth of development as a shared solution between the two applications, adaptations for single-mode reception is being investigated [61,62], including a demonstration of a downlink from the ISS to earth in [63].

A typical ground-based large telescope AO-enabled receiver for optical communications is illustrated in Fig. 4.3. First, the telescope is pointed toward the transmitter (incoming wave), this step represents the coarse pointing control. For links with slow angular movement, as for deep space, coarse pointing control can operate on knowledge of the transmitter position. The necessary information is generated from calcu-

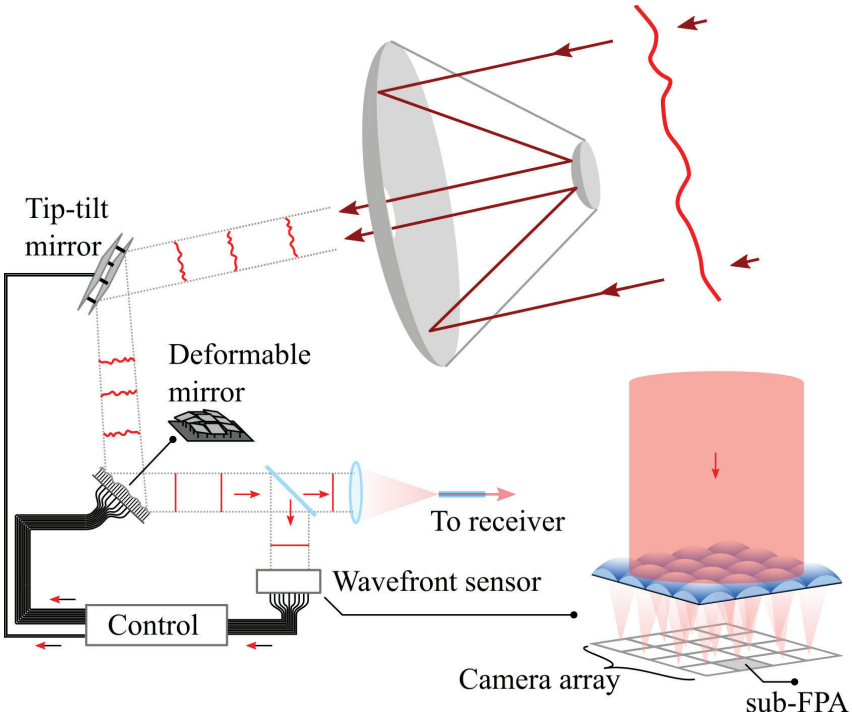

Figure 4.3: A large-area receiver featuring SMF-coupling, active tip-tilt and turbulence compensation using AO driven by direct wave-front sensing.

lated relative trajectories and calibration is done by visual referencing to nearby observable space. As such, coarse pointing will not be a limiting factor for the type of links considered here. For faster angular movement, as present in Low earth orbit (LEO) to ground links, telescope pointing may need a reference beacon to lock onto [21].

After coarse pointing, the received wave is collected by the telescope and reflected off a fast-steering mirror for tip-tilt-correction of AOA fluctuations. As discussed in chapter 2, fluctuations in AOA come about as the net phase-front normal of the wave, averaged across the aperture, may fluctuate around the optical axis as a result of the turbulence. The tip-tilt mirror thus have to perform this angular compensation at at the timescale of the atmospheric fluctuations, ranging from hundreds of Hz up to kHz [21]. The tip-tilt of the mirror, typically realized using fast piezoelectric actuators, is operated using a control loop which uses the received signal as feedback, as will be discussed shortly.

After overall tilt is compensated the remaining spatial phase distortion is cancelled by reflecting the field off a deformable mirror which is adaptively controlled to form the conjugate shape of the spatial phase front. Different types of deformable mirrors exist, with some based on densely spaced piezoelectric actuators, MEMS or motor-driven voice-

coils, both with segmented (lossy) or continuous surfaces (low loss). The common principle of operation is to control the individual mirror elements, their normal-offset (piston), to achieve the desired mirror shape. The close spacing of control elements enabled by the different implementations also allow for small footprint and easy scaling to large number of elements.

To continuously update all mirror elements correctly, a wavefront sensor measures the wavefront of a portion of the corrected field (tapped using a beam-splitter) for control feedback. The overall measurement of the wavefront may also be used to update the tip-tilt mirror control. Meanwhile, the other portion of the corrected field is focused into a SMF and is sent to the communications receiver.

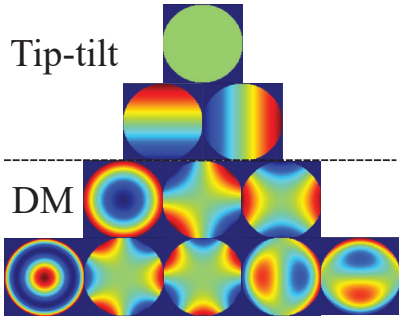

Figure 4.4: Low-order Zernike modes. DM, deformable mirror.

One of the more intuitive wave-front sensing types is the Shack-Hartmann wavefront sensor [57] and is illustrated in the figure. Here, the beam is incident on a microlens array whose individual elements images each sub-field onto the respective sub-FPA. Any residual phase distortion, i.e. phase angle across a lenslet, will result in a deflected focus spot on the sub-FPA, providing information of the magnitude and direction of the distortion. Pretending there is a one-to-one correspondence between individual deformable mirror-elements and sub-FPAs it is straightforward to understand how the mirror control is updated. In reality, this is generally not the case, instead a real-time computer is used to calculate the appropriate mirror update state from the collected information from the entire wavefront sensor. Other wavefront sensors such as the pyramid [57] and curvature [57] wavefront sensors employ a more complex setup but offer different benefits and trade-offs. As with the deformable mirror, the wavefront sensor is generally realized using small footprint optics and electronics and is easily scaled to accommodate higher spatial resolution.

To compensate the $\sim N$ spatial modes collected by the telescope one would in principle need N mirror elements. However, a square array of mirror elements typically does not form an optimal spatial mode basis for turbulence compensation. A typical decomposition of the N uncorrelated spatial modes, collected by the telescope, instead relies on the Zernike

polynomials, see Fig. 4.4. In this case, the control of individual mirror elements need not be completely uncorrelated, instead the shape of the mirror can be encoded by a superposition of N Zernike modes to reach efficiencies $\geq\sim 75\%$. Having a large number of mirror elements $\gg N$ alleviates the construction of smooth mode shapes and also provides the freedom in adapting how many Zernike modes to compensate, as both P_{r_0} and N (via r_0) may vary with time.

For AO to be both efficient and sensitive, it is important for the wavefront sensing system to be as sensitive as possible. Based on the analysis of the fundamental information limit of wavefront sensing in [64], it is found that roughly 1 photon per mode is required for efficient AO ($\lambda/14$ rms wavefront error or 0.8 Strehl ratio). Practical wavefront sensors have yet to reach such performance but further developments may push the technology close to this limit [65].

4.1.1 Performance of adaptive optics

The performance of the AO system will depend on the exact implementation and the used wave-front sensor. Here we estimate the efficiency for a theoretical and practical AO system to provide an example for later comparison with the multi-aperture and multi-mode reeceivers. The theoretical system assumes a wave-front sensor composed of CMOS integrated avalanche photo-detector (APD) or single photon avalanche detector (SPAD) [66] arrays, which is typical for AO systems. Such detectors are typically cooled to eliminate the thermal noise. The dominating noise will instead be given by the excess detector noise (e.g. multiplication noise for APDs), represented by a factor c, and background optical intensity I_b. For this system, we further assume a maximum receiver efficiency of 0.81 (optical losses), a detector quantum efficiency of 0.8 and a beam-splitting ratio of 0.1 (see Fig. 4.3), i.e. 10% of the light is tapped for AO control.

In Appendix A.1.1 we present a model for the optimized receiver efficiency for the theoretical AO system w.r.t. incident power per mode and specific turbulence channel parameters (similar procedure as for optimizing the dither-optical phase locked loop (OPLL) in chapter 3). The optimized efficiency is shown in Fig. 4.5 and compares cases of different c and I_b for a receiver of size $D = 0.8$, signal wavelength $\lambda = 1550$ nm, turbulence of $r_0 = 20$ cm and Greenwood frequency $f_G = 34$ Hz. The Greenwood frequency is a common measure of the timescale of the

atmospheric turbulence and is given by

$$f_G = 2.31\lambda^{-6/5}\left[\int_{\text{path}} C_n^2(z)v^{5/3}(z)dz\right]^{3/5}, \tag{4.2}$$

or, as $f_G \approx 1.99[S_\phi(f = 1) \cdot 1\text{ Hz}]^{3/5}$ with S_ϕ from Eq. (2.4). The estimated I_b for night and day are discussed in Appendix A.1.3 but will depend on the level of ambient light and how well it is spatially filtered.

For comparison, we estimate the AO efficiency of the demonstration in [63] (ISS to Table mountain CA downlink), see details in Appendix A.1.2. For this demonstration, −36.6 dBm of received power was required to be allocated to the AO system. Here, $D = 1$ m, $r_0 = 4.5$ cm (worst case) and since all parameters are not available, we assume a maximum efficiency of 0.81 and that $N_c = (D/r_0)^2$ modes were corrected for.

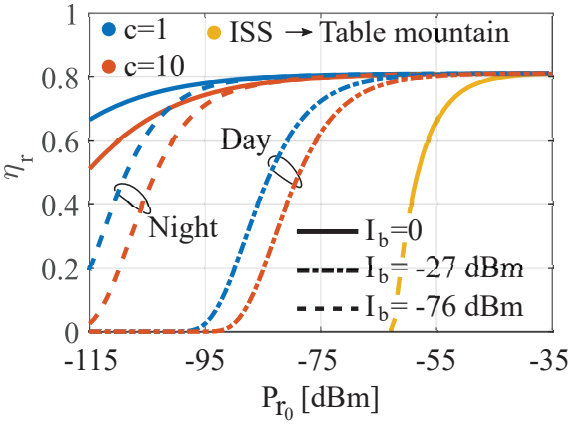

Figure 4.5: Estimated system efficiency vs. incident power per mode $P_{r_0} = I_r\pi r_0^2/4$ for the system in [63] (yellow) and the theoretical system example (all other curves).

Although we assumed a fixed beam-splitter ratio for the theoretical system, the splitting ratio deserves careful consideration as a trade-off between high AO SNR and high SNR for the communication channel. Its role can be compared to that of the dither magnitude ϕ_{mag} in a dither phase locked loop (PLL), only being much harder to dynamically tune.

4.1.2 Guide stars

We have so far assumed that the AO system uses the communication signal as a probe for sensing the atmospheric distortion, however, any other spatially coherent light entering the atmosphere from the same direction can be used as a reference for AO error feedback. Optical astronomy, which lack man-made reference signals, have historically relied on bright stars as reference for AO systems. The use of these natural guide stars (NGSs) restrict the observation to an angular cone aimed

at the NGS and is limited by the isoplanatic angle, beyond which the atmospheric turbulence channel is no longer correlated.

Since bright enough NGSs are few and far between the amount of observable space using AO is severely limited. This prompted the advent of the laser guide star (LGS), an artificial star in the sky generated by a strong receiver-side laser source aimed in the direction of interest and subsequently back-reflected by the atmosphere, see Fig. 4.6.

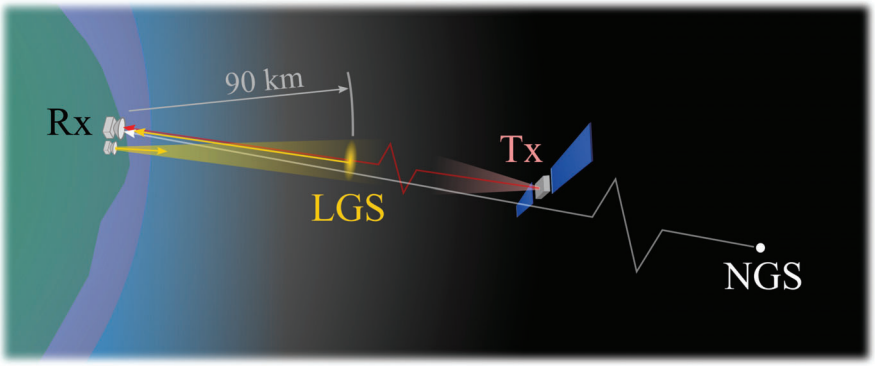

Figure 4.6: A space to ground link with high AO system SNR ensured by a strong communication signal (red), the light from a star (white) or the light from a LGS (yellow).

The laser guide stars enable the observation of any patch of the sky as well as wider field of view by the use of multiple LGSs and multi-directional AO correction. For optical communications, one LGS would be enough and could help enable highly efficient AO independent of the received signal power which is expected to be extremely low for deep-space communications. For optical communications the most promising LGS-implementation to date is the Sodium LGS [67] which excites Sodium atoms ($\lambda \sim 589$ nm) located in the mesosphere, at an altitude of 90-110 km. The optically pumped patch of the Sodium layer emits fluorescence, part of which propagates back through the atmosphere and functions as a reference. The high altitude of the Sodium layer enables probing of the entire length of the significant turbulence channel and the narrow Sodium resonance secures spectral separation between the LGS and communication signal. The low chromatic dispersion of air and the use of reflective receive-optics implies a good correlation of phase correction between different wavelengths.

The use of LGSs has been investigated for enabling the point-ahead angle in ground-to-satellite links [68, 69] and while there is no work reported on its use for deep-space to ground AO enabled links yet, interest

for this promising development is expected to increase.

4.2 Multi-mode reception

In multi-mode reception (investigated in [B]) the free-space to fiber coupling is alleviated by several guided fiber modes which can better accommodate the number of modes N collected by the aperture, see Eq. (4.1). Fig. 4.7 illustrates a multi-mode receiver which, similarly to the AO-receiver, makes use of a tip-tilt mirror for compensating AOA fluctuations before the light is coupled to an MMF.

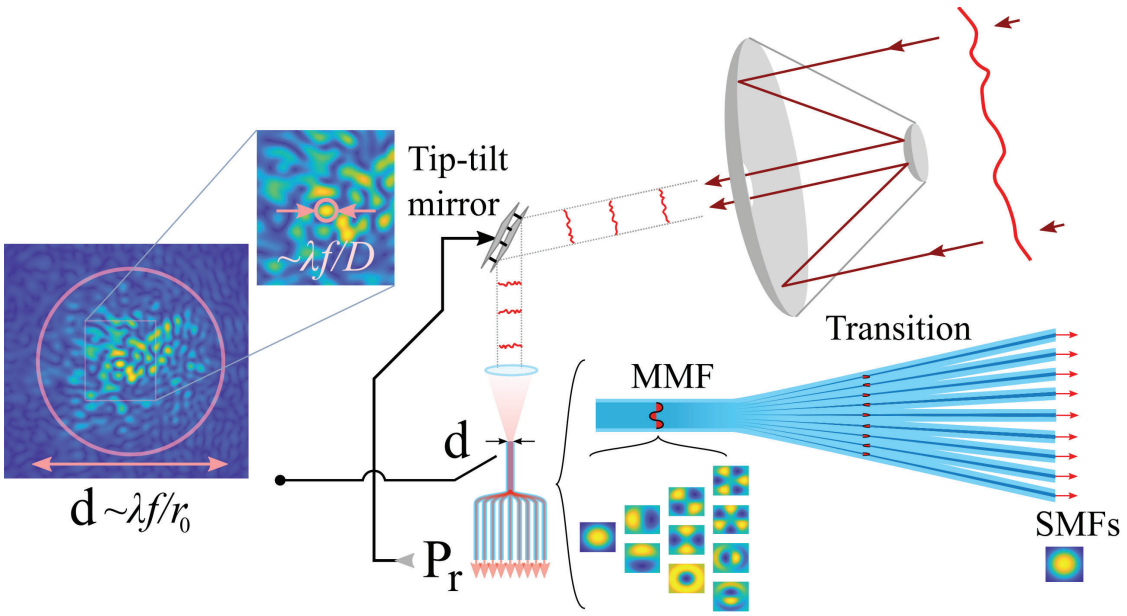

Figure 4.7: A large-area receiver featuring MMF-coupling and tip-tilt control. The MMF-collected light is split into SMFs using a PL (bottom right). The focused spot is illustrated in the left, featuring turbulence-caused speckle-patterns.

In the SMF reception case, the focal length is chosen such that the diffraction limited spot size $\sim \lambda f/D$ matches the fiber mode profile $\sim d$, i.e. $f \propto D$. For a turbulent channel, the focused spot is instead limited by the coherence length r_0 (as $\sim \lambda f/r_0$) and contains $N \approx (D/r_0)^2$ speckles/modes. Hence, choosing to receive this focused spot using an MMF supporting $N_c \geq N$ modes will passively couple most of the power into the fiber. This can be seen in Fig. 4.8 (from [B]) which shows the simulated coupling efficiency into MMF with two different number of modes vs. aperture size and r_0.

Matching the turbulence-limited spot to the fiber core results in an

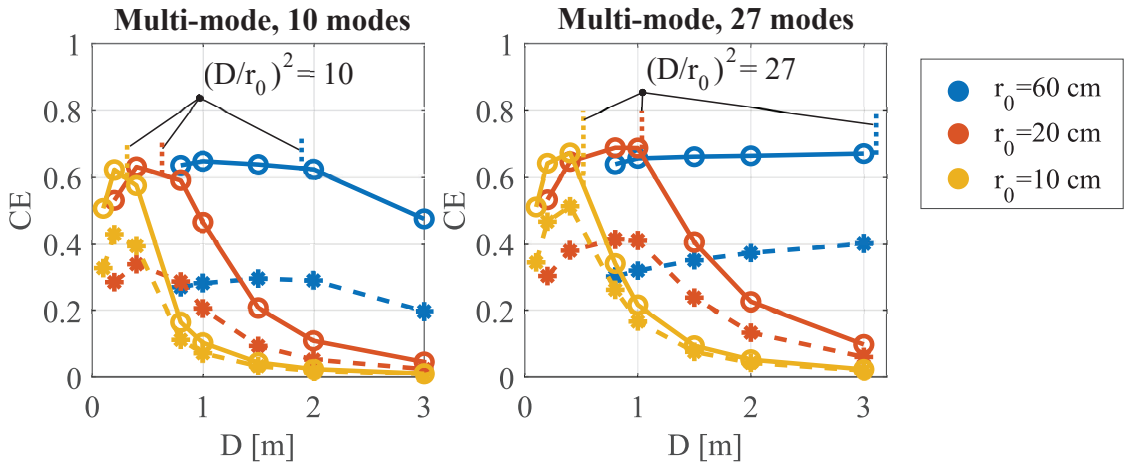

Figure 4.8: Simulated CE from [B] of MMF reception.

optimal focal length $f \propto r_0$ (for $D > r_0$) [70][B]. For the MMF-case, we thus have an acceptance angle $\theta_{\text{MMF}} \sim \lambda/r_0$ which is not penalized by increasing aperture size, as opposed to $\theta_{\text{SMF}} \sim \lambda/D$ from section 2.2. The use of MMF in this way therefore reduces the impact of misalignment and AOA fluctuations by a factor r_0/D compared to SMF-reception and a factor $(r_0/D)^2$ in terms of the corresponding power spectral density (PSD).

The power captured by the MMF depends only on the number of modes used and the efficiency of the tip-tilt compensation. As such, the free-space to fiber coupling efficiency may be quite high and turbulence-resilient. However, the multi-mode-field contained in the MMF must be transformed into single-mode for coherent detection. This "transformation" is performed using coherent combining, either in the optical domain or in the digital domain, post detection. Coherent combining is explained later in this chapter (see section 4.4). In either case, to enable coherent combining of the different spatial modes it is practical to separate them into individual SMFs, something that can be done using a photonic lantern (PL) [71].

As shown in Fig. 4.7, a PL is realised by merging several SMFs into a MMF or by tapering out a MMF into several SMFs. Important is that the transition is adiabatic which results in low-loss coupling between the SMFs and corresponding MMF modes.

In general, the PL is not mode-selective, meaning that a random superposition of the MMF-guided Laguerre polynomial (LP) modes will correspond to a certain SMF. For a completely random field this does not matter, however, since the field is only partially perturbed by the

atmosphere and the power distribution across modes (see Fig. 4.2) tends to low-order modes, mode selectivity can be beneficial. Hence, when operating at the sensitivity limit, selecting the low-order LP modes with more power is important [72]. Mode-selective PLs have been realized [73] and may be adapted to such situations.

The feedback signal for the tip-tilt correction can be tapped from the end received power, after optical pre-amplification, to not contest the power budget for the communication link.

So far, experimental investigations on MMF-coupling efficiency for free-space reception have been reported in [70, 74, 75]. In [58] a MMF + PL free-space reception setup was experimentally investigated for coherent communications using digital coherent combining. Further studies including demonstrations in real atmospheric links for MMF + PL-enabled coherent receivers are expected in the future.

4.2.1 Performance of MMF-reception

For the multi-mode receiver, η_r can be divided into $\eta_r = \mathrm{CE}\eta_{tt}\eta_c$ where CE is the free-space to fiber coupling efficiency under perfect tip-tilt compensation, η_{tt} is the tip-tilt efficiency and η_c is the combining efficiency in the coherent combining stage. Both tip-tilt compensation and coherent combining can make use of the efficient dither-OPLL for loop control. While we will treat the combining efficiency further down (section 4.4), the tip-tilt efficiency can be modelled as

$$\eta_{tt} = \eta_{\text{tip-tilt}}(1-\mathrm{CE}_0/\mathrm{CE})+\mathrm{CE}_0/\mathrm{CE}, \quad \eta_{\text{tip-tilt}} = e^{-(\sigma^2_{\phi_{e,x}}+\sigma^2_{\phi_{e,y}})/2} \tag{4.3}$$

where CE_0 is the average coupling efficiency without tip-tilt compensation and $\sigma^2_{\phi_{e,x}}$ and $\sigma^2_{\phi_{e,y}}$ are the residual phase error variances of the dither-OPLL compensating the tilt in the x, and y-direction, respectively [B]. The directional phase in this context, as seen by the OPLL, is related to the AOA fluctuation $\theta_x = \theta_x(t)$ as[B,appendix A.2]

$$\phi_x \approx 1.21\frac{r_0}{\lambda}\theta_x, \text{for MMF} \quad \phi_x \approx 2.41\frac{D}{\lambda}\theta_x, \text{for SMF.} \tag{4.4}$$

The factor 2.41 results from the overlap between spot and fiber mode(s).

Based on the above relations the tip-tilt efficiency is numerically simulated in paper [B] for space to ground atmospheric channels. Examples of simulated tip-tilt efficiency for both multi-mode and multi-aperture reception are compared in section 4.3.1. To highlight the benefit of MMF-reception with regard to tip-tilt control we shall here make use of the

results in [76], which provides the AOA variance σ_θ^2 for a 1st order PLL both with high PLL bandwidth compensation and without compensation. Although it is not shown here, the AOA PSD is suppressed by the use of larger apertures, as a form of aperture averaging.

Using Eq. (4.4) we relate the angle variance to the equivalent PLL phase variance and for both the MMF and SMF case, with and without compensation the variance scales according to table 4.1. Here, $f_T = g(C_n^2(z), v(z), \text{path})/D^{1/6}$ is a measure of the AOA PSD cut-off frequency and $f_{3\text{dB}}$ is the 3 dB bandwidth of the PLL filter in use. The table shows how the use of MMF provides a clear advantage in rms tip-tilt phase with increasing D. It also shows the interesting result that the variance decreases also in the uncompensated case for MMF-reception with larger apertures, as opposed to the uncompensated SMF-case.

σ_ϕ^2 [rad^2]	SMF	MMF
compensated	$\propto \left(\frac{f_T}{f_{3\text{dB}}}\right)^2$	$\propto \left(\frac{f_T}{f_{3\text{dB}}}\right)^2 \left(\frac{r_0}{D}\right)^2$
uncompensated	$\propto \left(\frac{D}{r_0}\right)^{5/3}$	$\propto \left(\frac{r_0}{D}\right)^{1/3}$

Table 4.1: The tip-tilt phase error variance for single-mode and multi-mode reception both with active tip-tilt control on or off.

Optimizing the bandwidth and dither magnitude, as in chapter 3, for the OPLL using the expression for σ_ϕ^2 (compensated case) and assuming $P_r \sim \pi D^2 I_r/4$ yields the minimized residual phase error as

$$\sigma_{\phi_{e,x}}^2 \propto \sqrt{\frac{f_T S_n}{D^2 I_r^2}}, \text{SMF} \quad \sigma_{\phi_{e,x}}^2 \propto \sqrt{\frac{r_0}{D^3}\frac{f_T S_n}{I_r^2}}, \text{MMF} \tag{4.5}$$

where S_n is the system noise PSD (for direct detection of the error signal) and P_r is the end received power. The expression relies on the implicit assumption that CE ≈ 1 regardless of aperture size and while this can be ensured by capturing enough modes in the MMF case, it is typically not true for SMF when $D > r_0$.

As with AO it is reasonable to ask whether a guide star can be used to ensure high SNR of the tip-tilt and coherent combining control systems. As we will see in section 4.6.3, the coherent combining structure is very narrow-band w.r.t. wavelength and will in practice be unable to coherently combine signals of separated wavelengths simultaneously. A functional reference wave would thus be limited to occupy the same

wavelength as the signal, which may end up constituting noise on the communication channel.

4.3 Multi-aperture reception

The multi-aperture receiver (investigated in [A,B]) makes use of an array of smaller apertures with each one coupling the light into a single mode, see Fig. 4.9.

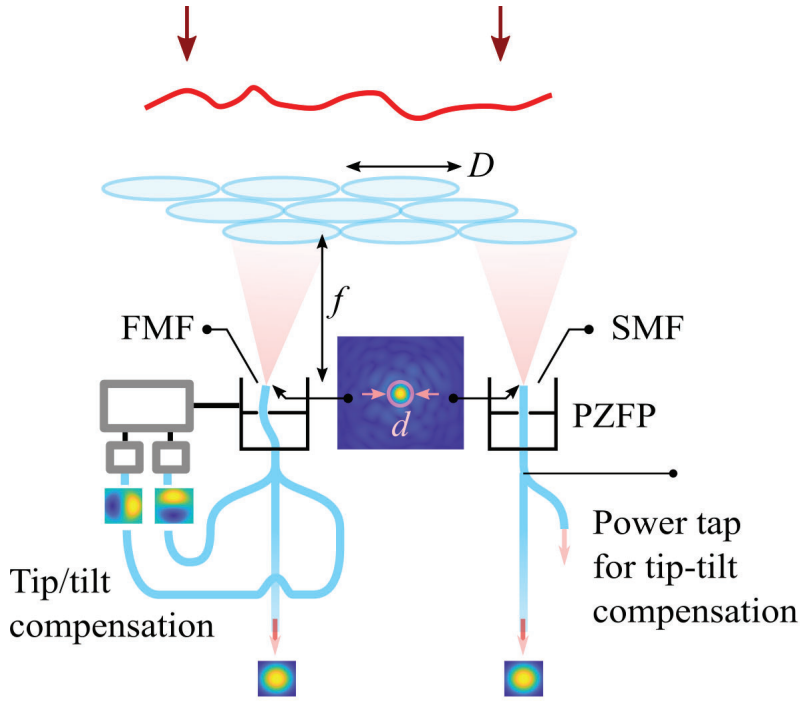

Figure 4.9: A large-area multi-aperture receiver with tip-tilt control enabled by piezoelectric fiber tip positioners. Tip-tilt error feedback is provided by power collected by higher order modes in an few mode fibers (FMF) (lower left) or by tapping the SMF power (lower right). A focused spot is shown in the center.

The concept of using multiple smaller apertures relies on the reduced pointing and turbulence penalties that come with the use of smaller D. The absence of wave-front compensation of the received field theoretically limits efficient single-mode coupling to the use of $D \leq r_0$ (recall chapter 2), also seen in Fig. 4.10 from paper [B]. Therefore, shrinking the aperture size to fit D to r_0, as can be done in an array receiver, can ensure efficient reception. The total size, or number of apertures, is straightforward to scale to the receive-area required by the communication link and is typically preferred cost-wise as large area telescopes are

increasingly difficult and costly to manufacture [77].

The multi-aperture receiver is also a good candidate for a receiver in a turbulence free channel. In vacuum, the received field is perturbation-free and the purpose for both AO and MMF reception would only be to compensate telescope deformations resulting from manufacturing errors or temperature gradients (both scaling with telescope size [35, 77]), something which is mitigated with the use of smaller telescopes. This scenario is investigated in [A] which targets the compensation of phase fluctuations between apertures, mostly caused by system imperfections and individual pointing control. If realized, a large area receiver in earth orbit, e.g. using an aperture array, could function as an intermediary for relaying deep-space communication signals down to earth and circumventing the issue of power-starved turbulence compensation at the ground. The aperture array would allow for easier piece-wise assembly in space and constitute a relatively flat receiver, avoiding the necessary depth of a large monolithic telescope.

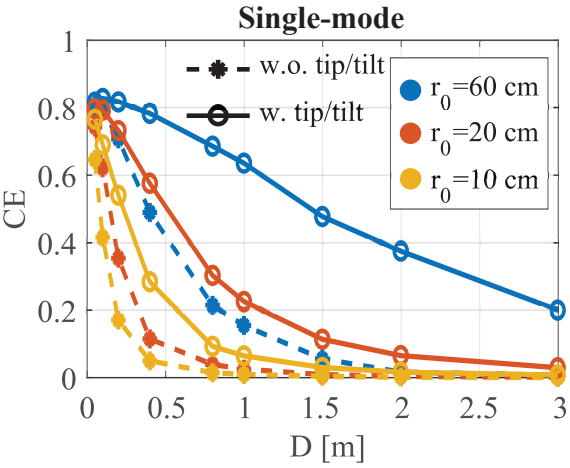

Figure 4.10: Simulated CE from [B] of single-mode reception.

For ground-based reception tip-tilt control is still necessary to maintain efficient coupling and must be performed individually for each array element which experiences unique AOA fluctuations. Practically, the tip-tilt can be compensated by adjusting the fiber tip position using piezoelectric actuators as in [78] and similarly to the MMF-receiver, the tip-tilt control can be realized using a dither OPLL.

Extracting an error signal to feed the tip-tilt control system is however less practical in this case. One could make use of a power tap, e.g. a 10 dB coupler, to allocate power to the control as is shown in the right of Fig. 4.9. This however reduces the efficiency of the receiver. An alternative would be to equip each SMF front-end with a preamplifier to avoid the loss of SNR. If erbium doped fiber amplifiers (EDFAs) are used we limit us to a, in the best case, 3 dB noise figure (NF) and subsequent sensitivity penalty of the communication signal. A phase sensitive amplifier (PSA) for each aperture to reach the best possible sensitivity

for coherent reception is less feasible due to the PSA complexity.

Another solution would be to use a FMF to SMF mode-selective PL for fiber-reception [73], as shown in the left of the figure, which in addition to collecting the fundamental mode also receives the first higher order LP11 modes. Any power collected in the higher order modes can be directly related to a focused spot offset due to imperfect tip-tilt compensation and would serve as efficient error feedback, non-invasive to the communication signal. The performance of this type of error feedback is investigated numerically in [B]. Such a solution should be verified experimentally as mode-scrambling may impede the separation of ideal LP-modes.

As for the MMF-receiver the individual SMFs are sent to a coherent combining stage where the signal is reconstructed.

Both multi-aperture transmission [79,80] and reception [59,81–83] has seen significant attention in recent years. Multi-aperture reception with coherent combining in urban horizontal links have been demonstrated in [81] and [82] using optical combining and in [84] and [85] using digital combining. Experimental work targeting low SNR reception and real-time operation include [A], [85] and [86].

4.3.1 Performance of multi-aperture reception

The multi-aperture receiver efficiency can be analyzed the same way as for the MMF-receiver. The expressions for the tip-tilt efficiency for SMF in section 4.2.1 apply also here, but with a slightly larger power penalty to the error signal when using the FMF approach as error tap (see paper [B]). In fact Eq. (4.5) emphasises the choice of D which benefits either approach best (in terms of tip-tilt): SMF for $D < r_0$ and MMF for $D > r_0$.

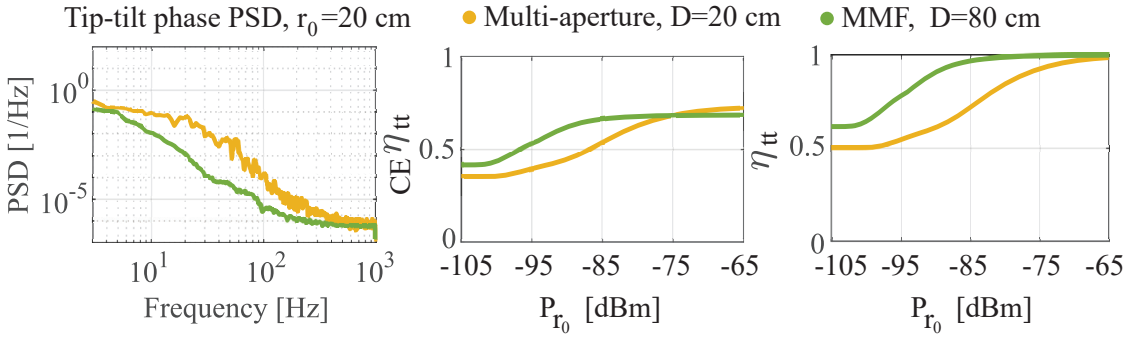

Figure 4.11: Simulated tip-tilt phase PSD, η_{tt} and $\eta_{\text{tip-tilt}}$ vs. P_{r_0}, based on the work in [B].

Simulated tip-tilt performance from the work in [B] is presented in Fig. 4.11 which compares the MMF and multi-aperture reception case. Here, the multi-aperture array consist of 16 $D = r_0$ receivers whereas the MMF receiver uses a $D = 4r_0$ aperture and 16 modes, i.e, both receivers have the same collection area and channel number, equal to the incident number of modes N. Fig. 4.11 indicates MMF-reception as superior in this case. This is expected as the OPLL SNR for each element of the multi-aperture array is $\sim 1/16$ lower than for the large MMF aperture, while their phase PSDs are also more severe.

As for MMF, the use of guide stars for the described multi-aperture approach is implausible. However, both AO and/or MMF-equiped large-area telescopes could constitute elements of a multi-aperture system, in which the different technologies could be synthesized for better performance.

To find the complete receiver efficiency, as for the MMF-case, we must also consider the coherent combining stage.

4.4 Coherent combining

Coherent combining is another word for in-phase coherent addition, or constructive interference. Which wording you use may depend on how the combining is performed. To date, coherent combining is typically performed either optically, pre-detection, or digitally, post-detection, see Fig. 4.12.

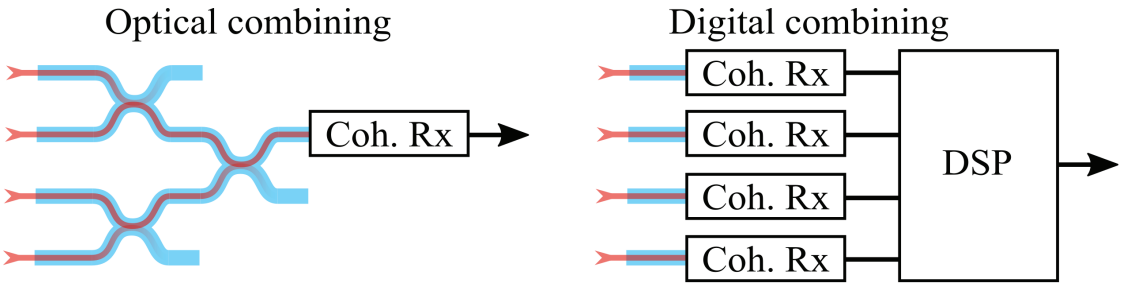

Figure 4.12: Left: Optical coherent combining via constructive interference in cascaded 50/50-couplers. Right: Digital coherent combing of digitally recovered signals from separate coherent receivers.

4.4.1 Digital Combining

In digital combining, each channel is coherently received individually, featuring optical pre-amplification and filtering if desired. The digital

signals produced in each receiver are then temporally aligned with respect to both the data symbol as well as the instantaneous phase before being summed together. The alignment and summation is carried out using digital signal processing (DSP) which is challenged by both low signal SNR as well as the relative phase variation between received channels. The relative phase variation is caused by the atmospheric phase fluctuations between receive-apertures, as well as phase noise from the used local oscillator (LOs). As such, the same laser should be used as the LO for all receivers, and channel delays should be short (within the equalizer window).

Up-scaling of this combining approach can be difficult for real-time operation. Typically, very large MIMO DSP is needed when increasing the channel count, e.g. 32x2 for 16 channels. In addition, a high cost is associated with the number of coherent receivers needed (same as number of channels). Yet many studies on this type of combining have been done [83–91]. A significant low-SNR performance was obtained in [84] which achieved lossless combining of a 11.52 Gbaud signal binary phase-shift keying (BPSK) signal transmitted over a 3.2 km urban horizontal link and received using 4 apertures at a power level of below 0.1 photons per bit (PPB) per receiver (-73 dBm). This demonstration used offline DSP, however, where for real-time systems it was concluded in [87] that there exists a trade-off between combining loss and real-time operation. Since then a real-time operated digital combining receiver featuring 2 apertures was experimentally demonstrated in [85] where a combining loss (or combining efficiency) of 75% was reported at down to -56 dBm received power per aperture for a 2.5 Gbaud quadrature phase-shift keying (QPSK) modulated signal. This result from 2024 represents the forefront of the digital coherent combining development.

In the context of the work in this thesis, where a PSA is desired as a receiver preamplifier, the digital combining approach would require one PSA per channel, which is implausible, as was previously mentioned.

4.4.2 Optical Combining

In optical combining two signals are combined via constructive interference, e.g., in a 50/50-coupler, see Fig. 4.13. Here, the two signals E_A and E_B of equal amplitude but different phase are assumed. A phase-shifter element present in one of the channels (ϕ_a-mod) is used to correct for this phase difference such that the two signals constructively add on one of the outputs in a subsequent 50/50-coupler $E_c = (E_A + E_B e^{j\phi})/\sqrt{2}$, while de-

structive interference takes place on the other output $(E_A - E_B e^{j\phi})/\sqrt{2}$. The phase control for compensating the varying phase difference $\phi(t)$ is a task perfect for the dither-OPLL and was in fact taken as example when explaining the dither-OPLL operation in chapter 3.

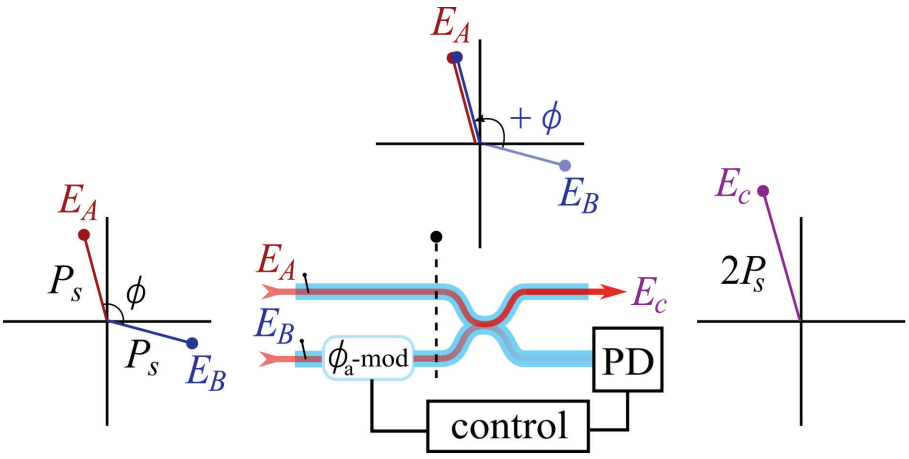

Figure 4.13: The 2-channel combining stage based on a phase-modulator and a 50/50-coupler. The operation of the combining is illustrated using the complex plane illustrations. PD: power detection.

Applying the dither-OPLL as control to the 2-channel combining stage will result in a residual phase error ϕ_e with variance $\sigma^2_{\phi_e}$ as explained in chapter 3. The residual phase error dictates the instantaneous and time-average combining efficiency as

$$\eta = \frac{1}{2}[1 + \cos\phi_e], \quad \langle\eta\rangle \simeq \frac{1}{2}[1 + e^{-\sigma^2_{\phi_e}/2}]. \tag{4.6}$$

which solely describes the performance of the combining stage.

Coherent combining of multiple channels is carried out using a combining cascade as shown in Fig. 4.14, where each combination is performed using a 2-channel stage. The total combining efficiency for the complete system is obtained as

$$\eta_c = \prod_{k=1}^{\log_2(N)} \eta_k \tag{4.7}$$

where N is the number of channels. Since the phase dither of earlier stages propagates down the cascade, different dither frequencies must be used for different stages to avoid undesired coupling between control systems.

This type of coherent combining system has been investigated together with multi-aperture receivers in fiber-based platforms [59, 81, 82] as well as in integrated photonics-based platforms [92–94], where different kinds of phase-control is implemented. The use of this type of system is also in focus in paper [A] which investigates the performance of 4-aperture combining of a 10 GBaud QPSK signal under emulated phase fluctuations at low received power. Via the use of optical pre-amplification of the error signal in the power detection unit (PD) we show a 4-channel combining efficiency larger than 97% for received powers per aperture > -80 dBm or > -70 dBm for the case of mild and moderate phase fluctuations respectively. This represents the most efficient combining demonstration at the received powers and data rates investigated so far, including both optical and digital combining.

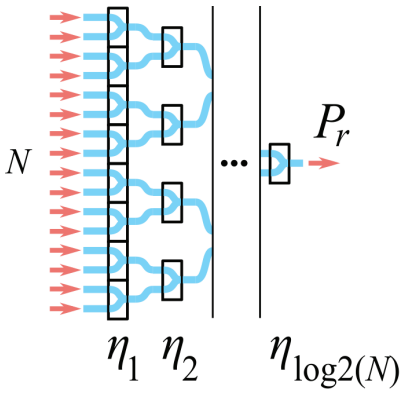

Figure 4.14: Cascaded coherent combining of N channels using $N-1$ 2-channel combining stages.

The use of optical combining results in a single signal channel, which lends itself well to PSA-pre-amplification.

Practical issues

In contrast to digital combining, optical combining must in practice also ensure that the data-modulated signals are aligned in polarization as well as being temporally aligned with respect to symbol, which at a symbol rate of 10 GHz would require less than a few mm of path difference between the two channels for efficient superposition. The latter requirement we will discuss further below (in section 4.6.3) and may pose a significant challenge for practical optical combining in large aperture arrays and possibly also for MMF-reception.

Another challenge in optical combining is the optical propagation loss in the combining cascade $L_s^{\log_2(N)}$ from a loss per stage L_s. Although the use of fibers and 50/50-couplers could be made lossless in principle, they are never lossless in practice, which would negatively impact the efficiency and signal SNR. Again, inserting EDFAs at the front-end of the receiver would negate the loss but also the use of PSAs. If this loss cannot be minimized, a solution could be a combined use of both optical and digital combining where the final stages of optical combining

is replaced by a number of receivers and subsequent digital combining to reduce the number of stages in the optical combining cascade.

Up-scaling the optical combining structure requires $N-1$ individual power detection units for combining of N channels. While the use of optical pre-amplification and filtering error feedback avoids the use of many expensive coherent receivers as used in digital combining, the need for $N-1$ EDFAs, optical filters and photo-detectors is still demanding hardware wise. While there are ways in which the number of required filters and detectors can be reduced, there is yet no practical way of reducing the number of EDFAs without reducing the error signal SNR.

Compensation of amplitude and phase

Previously we assumed coherent combining of equal amplitude signals. In an atmospheric link, the field amplitude will fluctuate in addition to phase. Taking this into account the actual combining efficiency becomes

$$\eta = \frac{1}{2}[1 + R\cos\phi_e], \quad \langle\eta\rangle \simeq \frac{1}{2}[1 + Re^{-\sigma_{\phi_e}^2/2}], \quad R = \frac{2r}{1+r^2}, \tag{4.8}$$

where $r = |E_A|/|E_B|$.

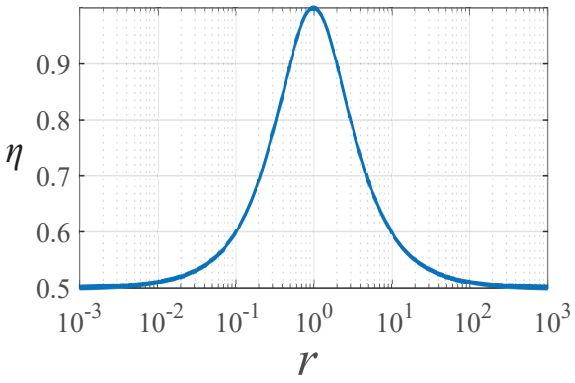

Figure 4.15: Combining efficiency vs. relative amplitude r based on Eq. (4.8).

Due to the amplitude mismatch r, perfect constructive and destructive interference cannot be achieved, resulting in a reduced combining efficiency, see Fig. 4.15 which shows $\eta(r, \phi_e = 0)$.

An example of simulated power and relative phase vs. time for two signals captured using adjacent apertures with $D = r_0 = 20$ cm is shown in Fig. 4.16, including the relative amplitude r and resulting η according to Eq. (4.8) with perfect phase compensation. In this case the time average efficiency becomes limited to $\langle\eta\rangle = 0.91$, which in a cascaded scenario can become detrimental for the total efficiency.

To remedy this, the combining stage can be adapted for both relative amplitude and phase compensation, see Fig. 4.17. In this configuration, two phase-controls are needed for the compensation of phase (ϕ_a-mod) and amplitude (ϕ_b-mod), respectively. We know that to achieve perfect constructive interference in the final 50/50-coupler, the input waves to

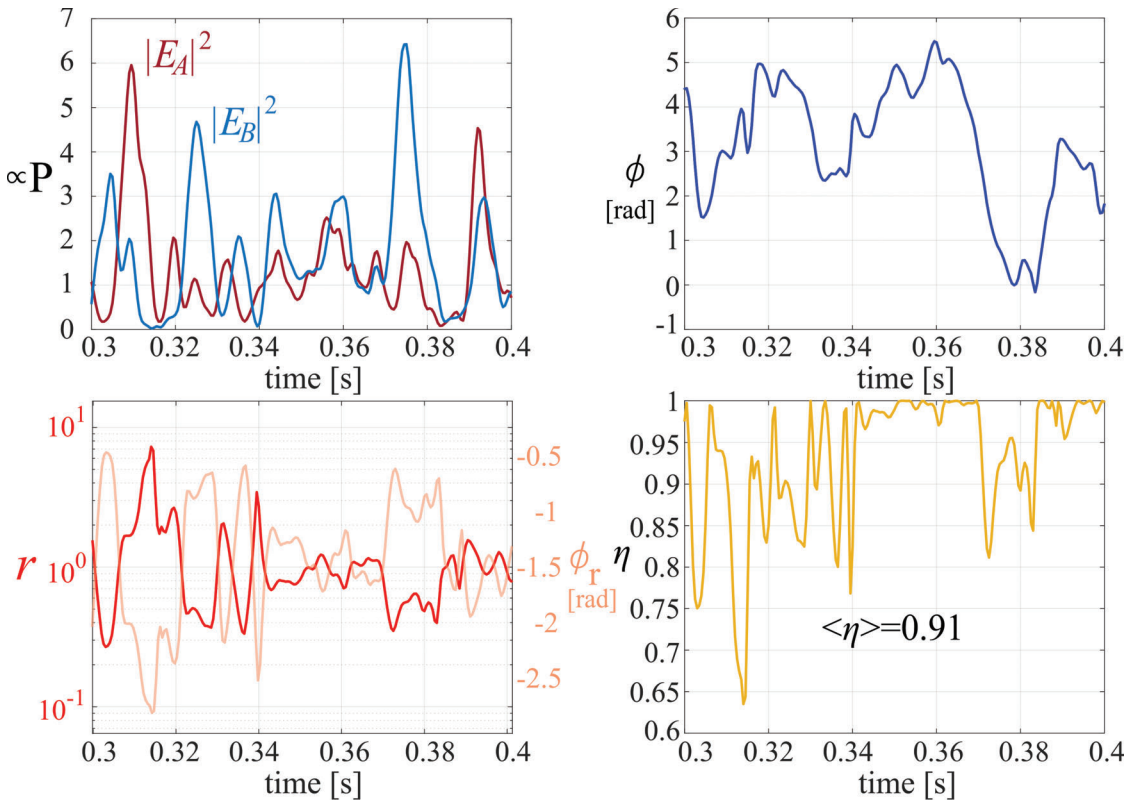

Figure 4.16: Top left: Simulated power fluctuations in two adjacent SMF-coupled receivers with $D = r_0$. Top right: Simulated relative phase for the same case. Bottom left: relative amplitude and corresponding phase ϕ_r. Bottom right: The combining efficiency resulting from the relative amplitude variation in the bottom left in the combining system shown in Fig. 4.13 with otherwise perfect phase compensation.

that coupler must exhibit equal amplitude. Hence, the task of the first phase control is to ensure this. This is done by aligning the two input waves E_A and E_B 90° out of phase to each other. This prohibits interference of the two waves in the first 50/50-coupler which causes the power of each wave to be split in half, thereby achieving its objective of equal amplitudes for $E_{AB} = (E_A + E_B e^{\phi_a})/\sqrt{2}$ and $E_{BA} = (E_A - E_B e^{\phi_a})/\sqrt{2}$. The remaining phase offset ϕ_r (also see Fig. 4.16) is given by

$$\phi_r = -\arccos\left(\frac{1-r^2}{1+r^2}\right) \tag{4.9}$$

and is compensated using ϕ_b-mod.

Applying two separate dither-OPLLs for the two phase controls in this system will enable simultaneous amplitude and phase correction. Each OPLL applies its own dither, of different frequency or using or-

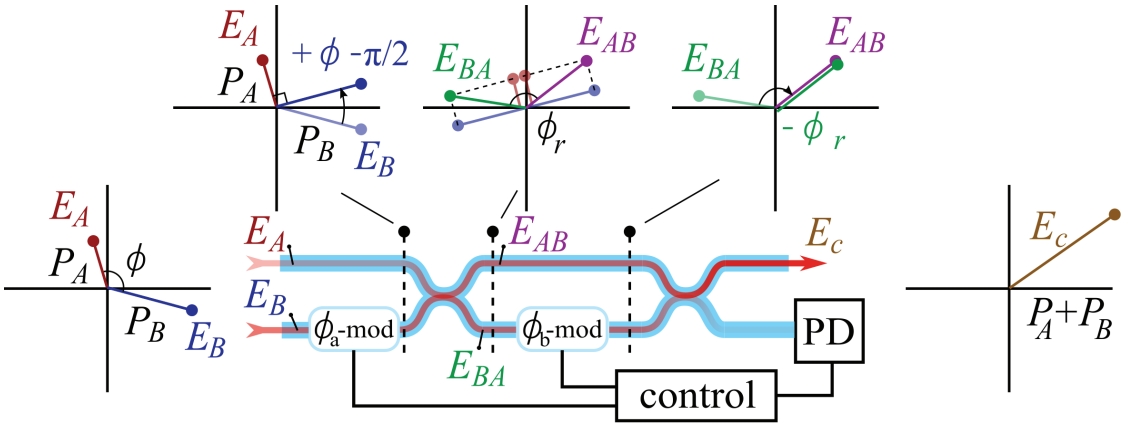

Figure 4.17: A 2-channel combining stage with relative phase compensation in ϕ_a-mod and relative amplitude compensation in ϕ_b-mod. The operation of the combining is illustrated using the complex plane illustrations. PD: power detection.

thogonal phase, in their respective phase control ϕ_a and ϕ_b. It is shown in [B] that for a well-performing system (small phase errors) there is no coupling between the two controls, meaning each system may be independently optimized as described in chapter 3.

The resulting combining efficiency for the combining stage is expressed as[B]

$$\langle \eta \rangle \approx \frac{1}{2}[1 + e^{-(\sigma^2_{\phi_{eb}} + \sigma^2_{\phi_{ea*}})/2}], \quad \sigma^2_{\phi_{ea*}} = R^2 \sigma^2_{\phi_{ea}}. \tag{4.10}$$

Here, $\sigma^2_{\phi_{ea}}$ and $\sigma^2_{\phi_{eb}}$ are the residual phase error variances for the dither-OPLLs independently compensating phase and amplitude respectively.

The combining system in Fig. 4.17, or different versions thereof, plays an important role in the area of programmable photonic circuits [95] for optical computing where addition and subtraction of optical signals rely on the precise control of phase and amplitude. For the purpose of coherent combining for multi-aperture or MMF-reception this combining architecture has been studied in [96] and [B]. The work in [96] demonstrated efficient turbulence mitigation for a 10 Gbaud on-off keying (OOK) signal received using a photonic-integrated multi-aperture array of 16 elements in an indoors free-space link with emulated turbulence. Meanwhile the work in paper [B] demonstrates efficient ($> 97\%$) 2-channel combining for a continuous wave (CW) signal at received power per channel down to $\sim (-70, -75)$ dBm under emulated turbulence conditions for two realistic space-to-ground links.

4.4.3 Final MMF and multi-aperture performance

The performance of the coherent combining system, including the final performance of the MMF and multi-aperture receiver, is illustrated in Fig. 4.18.

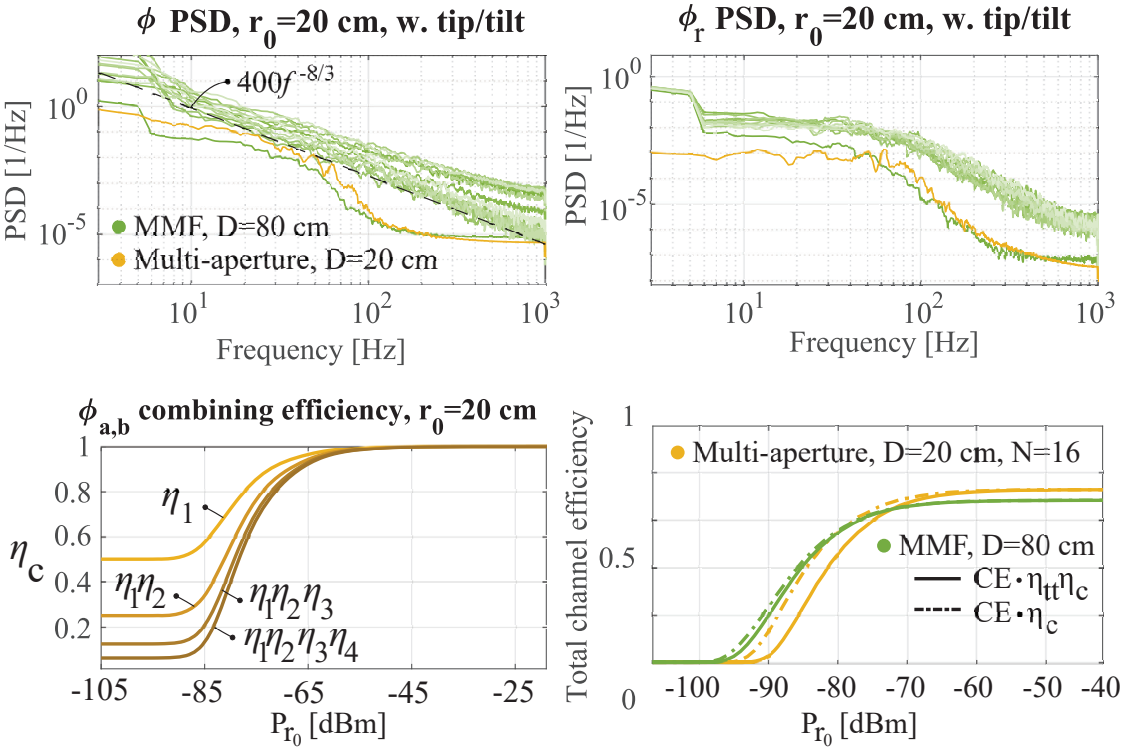

Figure 4.18: Top left: relative phase PSD for the initial combining stage of the coherent combining system for the multi-aperture array (yellow) and the MMF-receiver (green). The PSD of relative phase between adjacent apertures is on average identical whereas the PSD of phase between modes is not, hence the many green curves representing combining between different pairs of modes. Top right: as for the top left plot but for ϕ_r. Bottom left: the coherent combining efficiency in the multi-aperture case, showing the reduced efficiency with each subsequent combining stage. Bottom right: The total receiver efficiency η_r (solid lines) for the compared MMF and multi-aperture receivers. Dashed lines exclude the tip-tilt efficiency.

With respect to phase PSDs for ϕ and ϕ_r, the multi-aperture combining enjoys slightly less severe PSDs due to some residual field-correlation between adjacent apertures (present for $D \lesssim r_0$). Meanwhile most MMF-received modes are uncorrelated and follow the $1/f^{-8/3}$-profile. The evolution of η through the coherent combining stage can be seen in the lower left of the figure. The multi-aperture and MMF-receiver are compared in the lower right, also when excluding the tip-tilt compensation, in which

the performance of the two approaches is very similar. In this example, the number of modes used to collect the incident field in either case matches $N = (D/r_0)^2$. In fact, to achieve both high η_r as well as low sensitivity it was concluded in [B] that one should strive to fulfill this condition. Recalling the trade-off between the number of corrected modes (high efficiency) and the power per corrected mode (sensitivity), this rule is intuitive. The fact that both approaches perform similarly (excluding tip-tilt) suggests there is no fundamental difference in how the uncorrelated modes are collected and compensated. With tip-tilt taken into account, however, we do see a small advantage for multi-mode reception w.r.t. sensitivity, at least for the types of tip-tilt correction studied.

4.5 Comparing the methods

Shown in Fig. 4.19 is a comparison of the final efficiency for all three receivers, AO, MM and multi-aperture. Here, the number of modes corrected in the ideal AO system (discussed in section 4.1.1) was fixed to 16 for a fair comparison. In this example all systems have the same receiver area and number of modes/apertures, except the black curve which represents the work in [63]. The simulations of the multi-mode and multi-aperture receiver are fairly accurate w.r.t. the maximum efficiency. Of course, practical implementation penalties are not accounted for here which makes a truthful comparison of maximum efficiency between methods difficult. The optimal approach in this respect will likely depend heavily on the implementation.

To compare the sensitivity between approaches, the power at which the normalized efficiency has dropped 10%, is marked by *. This indicates a 20 dB sensitivity-advantage for the simulated multi-mode and multi-aperture systems compared to the demonstration in [63].

It should be noted that the channel parameters for the simulations in Fig. 4.18 and the real link scenario in [63] are different, wherein [63] the phase PSD was likely more severe due to fast relative speed of the ISS to ground link and 75° zenith angle. For such a link the simulated sensitivity can be expected to degrade, still the comparison provides an indication of the sensitivities that can be realistically reached, as well as the ultimate limit as represented by the ideal AO-system (using a linear, ideal SPAD).

The day-night representations depend on the spatial and spectral filtering used to calculate the background radiation I_b. In a direct-

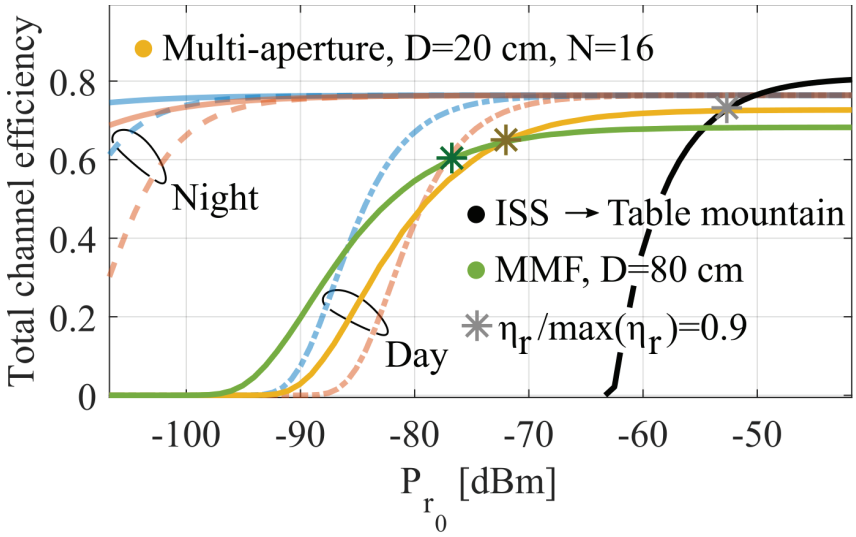

Figure 4.19: The total receiver efficiency η_r (solid lines) for the compared MMF and multi-aperture receivers. The blue and red curves represent the AO system described in section 4.1.1 and the black curve is an adapted result of the AO system sensitivity from the demonstration in [63].

detection AO wavefront sensor without fiber coupling the ability to narrowly filter both spatial and spectral components is limited, hence this approach suffer more in daytime links. Meanwhile the fiber coupled multi-aperture and MMF systems have very narrow spatial filtering and with added narrow optical spectral filters the background light can be significantly reduced.

While we have discussed the different receiver implementations, how they solve the problem of efficient single-mode reception and how they perform in terms of efficiency and sensitivity, there is no decisive conclusion regarding a preferred system at this point. Each approach offer unique advantages that may suit different scenarios. Cost is an important driving factor and to fully evaluate the potential of each solution, for the purpose of ground-based reception of deep-space signals, field demonstrations are essential. Luckily, the research is pushing the development in this direction.

4.6 Additional details

In this final section of the chapter, we expand the discussion to cover some few additional details that may be of technical interest. These include the OPLL impact on the bit error rate (BER), how the control system performance scales with signal bandwidth and how coherent com-

bining behaves when faced with multiple wavelengths and/or broadband optical signals.

4.6.1 OPLL impact on BER

For a pre-amplified coherent receiver, the communication channel SNR is proportional to $P_r = I_r A_r \eta_r$ and the BER is given as (Eq. (2.8))

$$\mathrm{BER} = \frac{1}{2}\mathrm{erfc}\left(\sqrt{\eta_r \frac{\mathrm{SNR}}{M}}\right) \tag{4.11}$$

where the SNR inside the expression is calculated for $\eta_r = 1$.

The final efficiency η_r will impact the BER in a multi-mode, multi-aperture or AO-enabled receiver in the same way, as described by Eq. (4.11). It is generally not adequate to believe that this impact can be expressed through the time-average efficiency. Instead, the normal-distribution of the phase error ϕ_e (per corrected/combined mode) will transfer to the BER and cause a resulting BER distribution. The BER is however not defined for a short time span, instead the time-average BER is obtained by averaging this BER-distribution.

Figure 4.20 shows how a phase error of normal distribution with different standard deviation is transferred into a resulting BER-distribution via Eq. (4.11) with SNR=5 and $M = 1$. In the right of the figure is also shown the resulting BER as calculated properly $\langle \mathrm{BER}(\eta) \rangle$ compared to $\mathrm{BER}(\langle \eta \rangle)$. It shows that for phase error deviations above $\sim 20°$ the use of $\langle \eta \rangle$ to estimate the BER becomes erroneous at low SNR. This effect is further exacerbated at higher SNR.

The above result is descriptive of the influence of, e.g., a single combining stage. When incorporating compensation of phase between many modes the fluctuations in the aggregate efficiency η_r will even out as a form of aperture averaging, assuming a well performing system. This pertains also to other imperfections of the control systems. The residual dither (if used) and phase error on the combined channel (or compensated mode) will cause added phase noise to the signal. This phase noise is however uncorrelated between individual channels/modes and will be added incoherently, as opposed to the signal, thereby being averaged out before influencing the final BER significantly. Any remaining phase variation is then compensated in the DSP.

Since the free-space link is highly dynamic, it will experience outages. Signal fading properties relate to the received wave itself and the area size

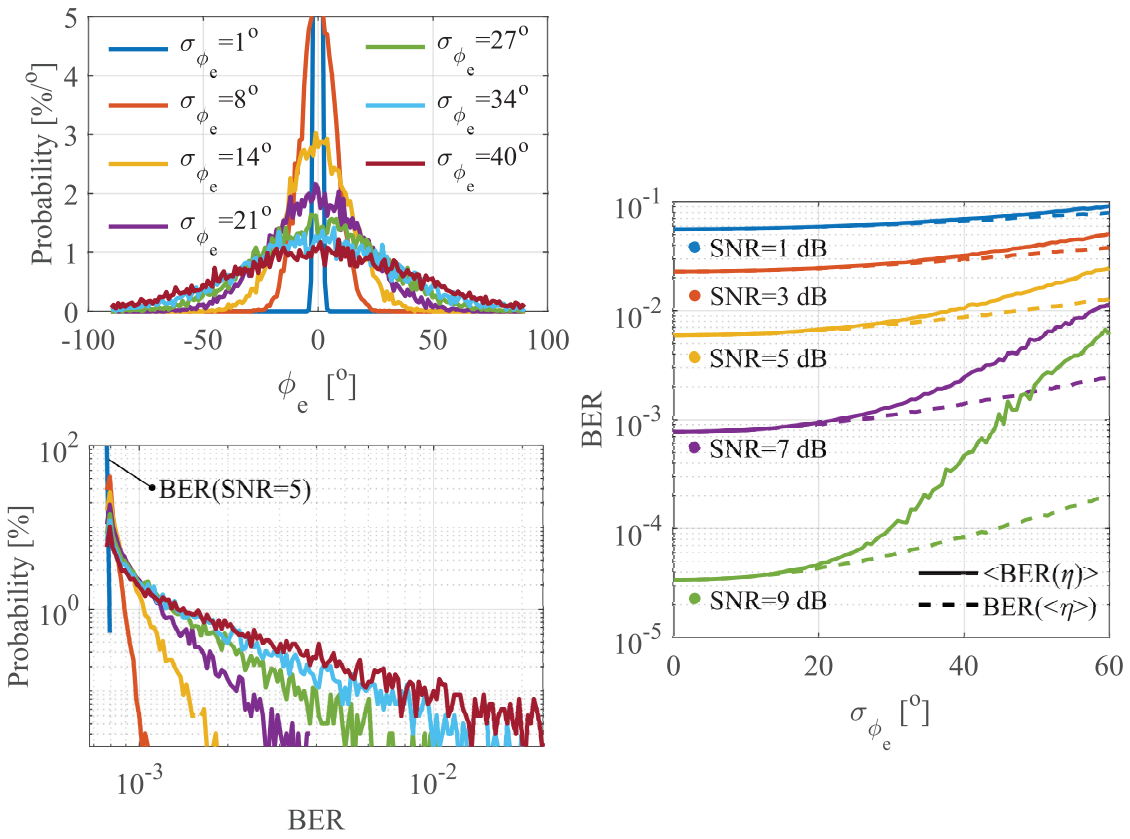

Figure 4.20: Top left: phase error distributions for different phase error deviations σ_{ϕ_e}. Bottom left: The BER distributions corresponding to the ϕ_e distributions in "top left" via the coherent combining efficiency. Right: The BER vs. phase error standard deviation at different SNRs for two ways of evaluation.

of the receiver and can be treated separately from the efficiency. Signal fading, although important in situations of bad weather and obscuration of the free-space channel, is expected to be of smaller impact for large-area receivers and remains outside the scope of this thesis.

4.6.2 Performance for varying signal bandwidth

The work of the appended papers focus its attention to demonstrations at 10 GHz symbol rate data communications. We know from chapter 2 that the link SNR is proportional to $P_s/\Delta f$ where Δf is the symbol rate and P_s the received signal power. Based on this expression, one can trade half the data rate to close the link at half the power otherwise required. For the optically pre-amplified error feedback-based dither-OPLL discussed here, the detection is limited by Noise-Noise-beating of bandwidth $\Delta\nu_o$ (see section 2.3.1). If the optical filter bandwidth is minimized to the

symbol bandwidth $\Delta\nu_o = \Delta f$, then the OPLL SNR abides a $P_s^2/\Delta f$-ratio, meaning half the bandwidth can only be traded to close the link at $1/\sqrt{2}$ times the power otherwise required. Hence, the SNR of the link and the SNR of the dither-OPLL do not scale proportionally w.r.t. the trade-off between symbol rate and signal power. From the perspective of 10 GHz symbol rate, this will imply an overall worse performance at lower data rates whereas for increasing data rates the penalty from phase-locking is relatively small. In practice, the difficulty in realizing narrow optical filters smaller than 10 GHz also limits any gains in decreasing the signal bandwidth w.r.t. the locking system.

4.6.3 Coherent combining at multiple wavelengths

Problems arise when attempting coherently combine multiple wavelength signals simultaneously. Here we consider an example with two signals at different wavelengths λ_1 and λ_2 ($\Delta\lambda = \lambda_1 - \lambda_2$), both being received in a multi-aperture receiver. This scenario is of interest for PSAs as many times, two or even more waves need to be co-propagated in the channel to facilitate the PSA process at the receiver.

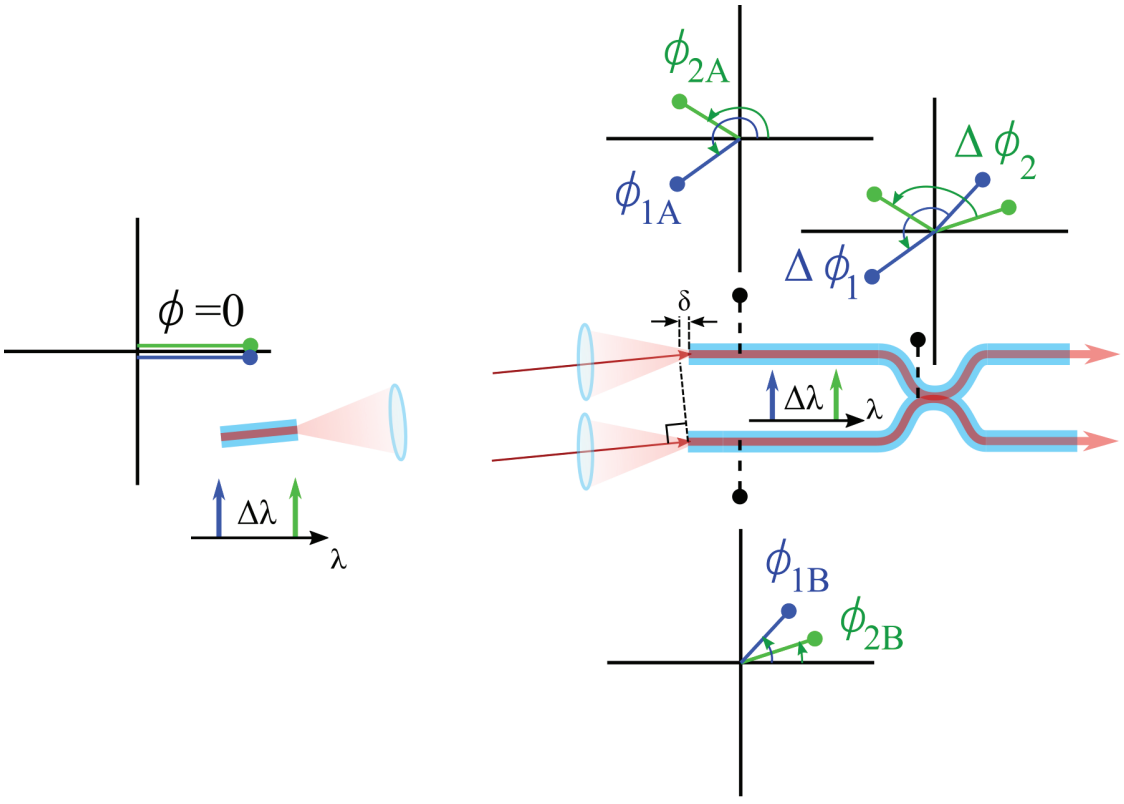

Figure 4.21: Multi-aperture reception of a dual-wavelength signal with a short path length difference between apertures present.

Consider the scenario in Fig. 4.21. Here, a slight misalignment of the array plane results in an extra propagation distance δ in the upper arm. Given δ and a common path length L between transmitter and the 50/50-coupler, the phases indicated in the figure can be written

$$\phi_{1A} = \frac{2\pi(L+\delta)}{\lambda_1}, \quad \phi_{2A} = \frac{2\pi(L+\delta)}{\lambda_2}, \quad \phi_{1B} = \frac{2\pi L}{\lambda_1}, \quad \phi_{2B} = \frac{2\pi L}{\lambda_2} \tag{4.12}$$

$$\Delta\phi_1 = \frac{2\pi\delta}{\lambda_1}, \quad \Delta\phi_2 = \frac{2\pi\delta}{\lambda_2} \tag{4.13}$$

$$\Delta\Delta\phi = \Delta\phi_1 - \Delta\phi_2 = 2\pi\delta\left(\frac{1}{\lambda_1} - \frac{1}{\lambda_2}\right) \tag{4.14}$$

assuming negligible dispersion inside the short fiber.

A phase compensating system will compensate the phase of both wavelengths when applying a phase $\phi_a = \Delta\phi_1 = \Delta\phi_2$. This can only happen when $\Delta\Delta\phi = 0$, i.e. when either $\lambda_1 = \lambda_2$ or $\delta = p(1/\lambda_1 - 1/\lambda_2)^{-1}$ where $p \in \mathbf{Z}$. Let us assume that we, despite this try to apply a phase control which perfectly corrects the phase for a wavelength λ_c in the centre, between λ_1 and λ_2. The combining efficiency at either λ_1 or λ_2 becomes

$$\eta = \frac{1}{2}\left[1 + \cos\left(\frac{\pi\delta\Delta\lambda}{\lambda_c^2}\right)\right]. \tag{4.15}$$

This effect is illustrated in the top of Fig. 4.22, which shows the sensitivity in η vs. wavelength separation $\Delta\lambda$ for different path-length differences δ. In a typical PSA scenario with signal and idler spacing of $\Delta\lambda = 8$ nm we would require path length differences on the order of 0.1 mm or shorter for the combining to function properly. Such tolerances are exceptionally difficult to achieve in a practical system.

Since in a communication scenario we deal with signals of finite bandwidth, the actual combining efficiency is obtained by integrating Eq. (4.15) as

$$\eta_{\Delta\lambda} = \frac{1}{\Delta\lambda}\int_0^{\Delta\lambda} \eta(\Delta\lambda')d\Delta\lambda' = \frac{1}{2}\left[1 + \frac{\sin(\pi\delta\Delta\lambda/\lambda_c^2)}{(\pi\delta\Delta\lambda/\lambda_c^2)}\right]. \tag{4.16}$$

This efficiency is also shown in the bottom of Fig. 4.22 and shows that for e.g. a 10 GHz signal, the path length difference should be shorter

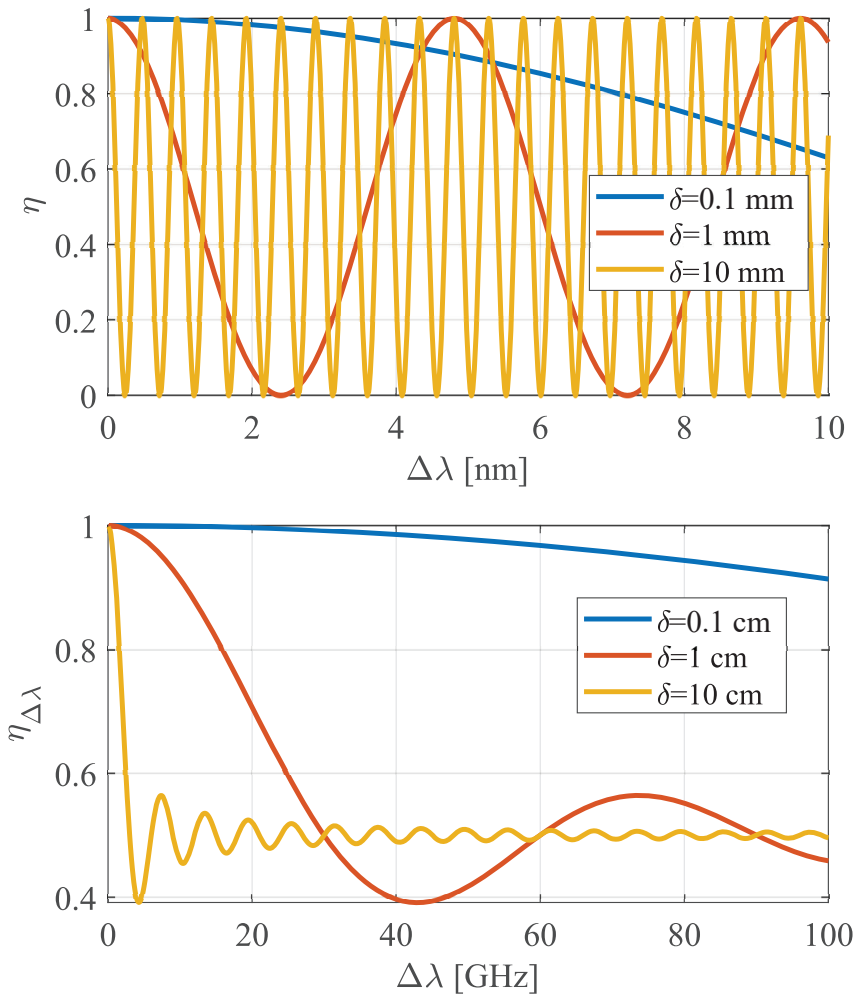

Figure 4.22: Top: η vs. $\Delta\lambda$ for $\lambda_c = 1550$ nm and different values of δ, according to Eq. (4.15). Bottom: $\eta_{\Delta\lambda}$ vs. $\Delta\lambda$ for $\lambda_c = 1550$ nm and different values of δ, according to Eq. (4.16).

than 1 cm ideally (a 10 Gbaud signal has a symbol length of 3 cm in free-space and roughly 2 cm in fiber). This tolerance is more reasonable in a practical system, however, it will still prove challenging to maintain for a large array tracking a moving transmitter. A practical system would need to implement some sort of delay-control (preferably using an infinity-corrected segment in the aperture lens-to-fiber path). The presence of path-differences appear also in MMF-reception due to dispersion between spatial modes in the MMF but is expected to be much less pronounced than for the multi-aperture system. It is however not expected to be practical to attempt combining of a 1550 nm signal and 589 nm Sodium guide star wave simultaneously.

CHAPTER 5

PSA implementation for free-space optics

The implementation of phase sensitive amplifiers (PSAs) as preamplifiers for free-space optical communications face several challenges. The requirement of several phase-locked waves to reach a low noise figure (NF) in the PSA has traditionally resulted in complex systems that are seldom attractive for implementation into practical communication links. This is especially true for communication into or out of space where any space craft-carried system should be as simple, energy-efficient and redundant as possible.

Each of the appended papers [C-E], one by one improves and/or simplifies the PSA-preamplified link, with the latest work in [E] finally demonstrating a PSA-based receiver that could in practice already be used in existing downlinks to earth. This chapter serves as an introduction to, and summary of these works.

5.1 PSA basics

In the context of optics, the PSA is a parametric amplifier which uses the nonlinear property of a propagation medium to facilitate the exchange of energy between waves of different wavelength. For instance, the 3rd order nonlinearity (Kerr effect [97]) in an optical fiber causes the refractive index n of the fiber to be modulated by the intensity I of an optical wave passing through it: $\Delta n \propto I$. The changed refractive index in turn

modulates the phase of the wave, leading to self-phase modulation. In the case of two co-polarized waves, each wave thus gets phase-modulated by the intensity of the other, leading to cross-phase modulation. The coherent superposition of the fields of the two waves also leads to an instantaneous beat intensity, in turn causing a moving refractive-index grating that propagates alongside the waves in the fiber. If more waves are added to this fiber, they will experience this travelling index grating and be partially scattered against it with appropriate Doppler shifts, i.e., frequency shifts. In a fiber this is called four-wave mixing (FWM) and enables power at one wavelength to be redistributed to others.

The efficiency of this scattering process depends on the relative phase between the interacting waves and dictates which wavelengths lose and gain power. Since different wavelengths experience different refractive indexes while propagating in the fiber, both due to the above mentioned nonlinear process but also due to chromatic dispersion, the relative phase will vary during propagation. The power transfer between waves will therefore oscillate back and forth and effectively average out, i.e., not very useful for an amplifier. To build an amplifier, one would need to ensure that the relative phase of the waves is matched throughout the fiber propagation.

5.1.1 Phase matching

The phase-matching condition can be written

$$0 = \kappa = \Delta\beta_L + \Delta\beta_{NL} \tag{5.1}$$

where β indicates the propagation constant $\beta(\lambda_i) = 2\pi n(\lambda_i)/\lambda_i$, $\Delta\beta$ refers to the relative propagation constant between all interacting waves (see section 5.1.2 and 5.1.3) and subscript L and NL refers to the linear and nonlinear dependence of β, respectively. The nonlinear propagation constant for a single wave (at wavelength λ_i) in the fiber is

$$\beta_{NL}(\lambda_i) = \gamma P_i + 2\gamma \sum_{j \neq i} P_j, \tag{5.2}$$

i.e. the contributions from self-phase modulation from its own power P_i and cross-phase modulation from the remaining waves $j, ..$ of power $P_j, ...$ Here, γ is the nonlinear constant of the fiber.

In terms of the linear propagation constant, its wavelength dependence is often described via a Taylor expansion around the zero-dispersion

wavelength λ_0 for a highly nonlinear fiber (a fiber where γ is large and where nonlinear effects become significant)

$$\beta(\lambda) = \beta_0 + \beta_1 \cdot (\lambda - \lambda_0) + \frac{\beta_2}{2} \cdot (\lambda - \lambda_0)^2 + \frac{\beta_3}{6} \cdot (\lambda - \lambda_0)^3 + .., \quad (5.3)$$

where $\beta_i = \frac{d^i \beta}{d\lambda^i}(\lambda_0)$. A zero-dispersion wavelength exist where the material dispersion and waveguide dispersion (both contributing to the overall chromatic dispersion) cancel. The zero dispersion wavelength can be engineered to match a desired wavelength during the manufacturing of highly nonlinear fibers. This freedom in selecting λ_0 is important to obtain phase-matching for the wavelength(s) one wish to amplify with a PSA.

Figure 5.1 illustrates the amplification gain of a wave (or waves) that can be obtained via FWM when the phase matching condition is unmatched, matched and quasi-phase-matched [98]. In the unmatched case (blue), the power among the waves oscillate back and forth and no significant net gain can be achieved. In the matched case (red), a large gain can be obtained as the FWM process continuously amplifies the wave throughout the entire fiber, assuming the other waves providing that power are undepleted. In the quasi-phase-matched case (yellow), the phase matching condition is not satisfied but alternated throughout the propagation to mitigate the walk-off between waves, leading to a useful net gain. This final scenario is usually implemented using periodically interfaced waveguides of different dispersion characteristics as a compromise in instances where the phase-matching condition cannot be fulfilled.

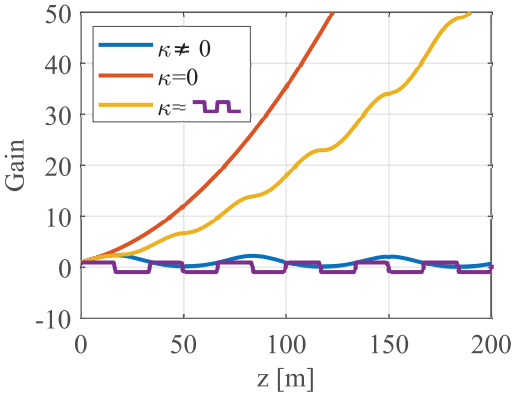

Figure 5.1: Fiber gain vs. distance z for different phase matching conditions: non phase-matched (blue), phase-matched (red), quasi-phase-matched (yellow). The purple curve illustrates the periodic variation of the relative propagation constant to obtain the quasi-phase-matched gain.

5.1.2 Four wave mixing

As the name implies, FWM is the interaction of four optical waves where power transfer occurs in an optical fiber, i.e., the Bragg scattering men-

tioned earlier. The frequencies of waves that can partake in this power transaction is determined by the law of energy-conservation as

$$\nu_1 + \nu_2 = \nu_2 + \nu_4 \tag{5.4}$$

where ν_{1-4} are the frequencies of the optical waves. Here power can be transferred either from frequencies 1-2 to 3-4 or reversely, from 3-4 to 1-2. Meanwhile the direction of power transfer is determined by the Bragg-condition (the phase-matching process above) and depends on the relative phase

$$\Delta\phi = \phi_1 + \phi_2 - (\phi_3 + \phi_4) \tag{5.5}$$

where ϕ_{1-4} are the phases of the optical waves. This relative phase is maintained throughout propagation if the phase-matching condition of Eq. (5.1) is met, which for FWM has

$$\begin{aligned} \Delta\beta = \beta(\lambda_1) + \beta(\lambda_2) - \beta(\lambda_3) - \beta(\lambda_4), \\ \Delta\beta_{\mathrm{NL}} = \beta_{\mathrm{NL}}(\lambda_1) + \beta_{\mathrm{NL}}(\lambda_2) - \beta_{\mathrm{NL}}(\lambda_3) - \beta_{\mathrm{NL}}(\lambda_4) \end{aligned} \tag{5.6}$$

where λ_{1-4} are the wavelengths of the optical waves.

The reason why the exchange involve particularly four waves is due to the 3rd order nonlinearity which is strongest in standard silica telecom fibers. In a waveguide where the strongest nonlinearity is of 2nd order you instead have three wave mixing (TWM).

Different FWM configurations of interacting waves are shown in Fig. 5.2 where optical amplification can be facilitated. Here, red waves (frequencies/wavelengths) are intended as strong pump waves (p) that amplify the weaker blue waves, denoted as signal (s) or idler (i) waves.

Configurations a) and b), involving four waves, adheres to the rules we have set up above. Configuration c) is obtained from a) when the two pump frequencies overlap ($\nu_s + \nu_i = 2\nu_p$). Similarly, d) is obtained from b) when signal and idler waves overlap ($\nu_{p1} + \nu_{p2} = 2\nu_s$). The final configuration e) is simply a combination of the previously listed FWM configurations.

For the purpose of low-noise phase sensitive amplification in fiber, configuration c) has been the most extensively used, with several significant demonstrations [30, 34, 99], including the lowest achieved NF using FWM in [28]. Its usefulness stems from the need for only three phase-locked waves, which simplifies any practical system. In this work, papers [C,D] target the implementation of this configuration whereas paper [E] demonstrates a PSA based on configuration d).

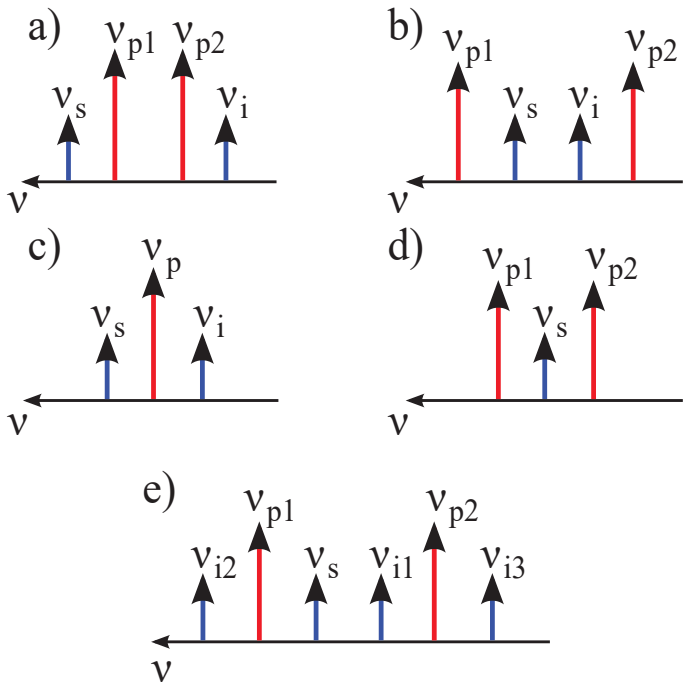

Figure 5.2: Different FWM wave configurations. Power is transferred from red to blue waves, or the reverse. a) and b) both constitute a dual-pump 2-mode parametric amplifier configuration. c) and d) are frequency degenerate cases of FWM, respectively called the single pump 2-mode and dual pump degenerate signal configurations. e) is a combination of many FWM processes, involving several waves, and is called the dual-pump 4-mode configuration.

5.1.3 Three wave mixing

The process of TWM occurs when the waveguide material exhibits a strong 2nd order nonlinearity. This nonlinearity often dominates in crystalline structures with prominent symmetry, for example in lithium-niobate which has been used as a platform to realize low-noise PSAs [100]. For a 2nd order nonlinear media the phase-matching condition is difficult to satisfy as there is no Kerr nonlinearity producing nonlinear phase shifts that can cancel the linear dispersion. To get around this issue earlier works propagated waves at different angles to achieve phase matching in bulk crystals [101]. For implementation into waveguides with co-propagating waves the solution of quasi-phase matching became prevalent [98]. The periodic change of the phase matching is typically achieved using poling, i.e. orientation inversion (flipping the crystal), hence the name periodically poled lithium-niobate (PPLN) for such lithium-niobate devices.

Similarly to FWM, TWM can be described by the frequency and

phase matching conditions $\nu_1 = \nu_2 + \nu_3$ and $\phi_1 = \phi_2 + \phi_3$, with

$$\Delta\beta = \beta(\lambda_1) - \beta(\lambda_2) - \beta(\lambda_3), \quad \Delta\beta_{\mathrm{NL}} = \beta_{\mathrm{NL}}(\lambda_1) - \beta_{\mathrm{NL}}(\lambda_2) - \beta_{\mathrm{NL}}(\lambda_3), \tag{5.7}$$

respectively. Typical TWM processes used for optical amplification are shown in Fig. 5.3.

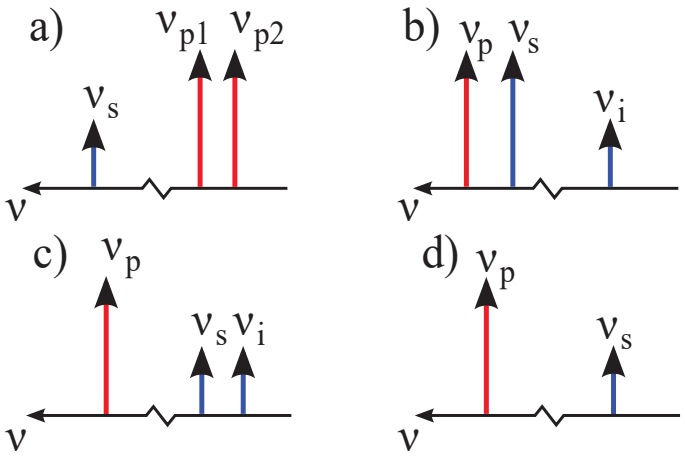

Figure 5.3: Different TWM wave configurations. Power is transferred from red to blue waves, or the reverse. a) is the sum-frequency generation process ($\nu_s = \nu_{p1} + \nu_{p2}$). b) is the difference frequency generation process ($\nu_p = \nu_s + \nu_i$). c) is the same as a) but where red and blue roles are reversed ($\nu_p = \nu_s + \nu_i$). d) is second harmonic generation ($\nu_p = 2\nu_s$).

Among these configurations the sum-frequency and second harmonic generation has been extensively used together with PPLN in TWM-based PSA demonstrations [39, 102–104], which include the lowest ever measured NF of an optical amplifier in [29].

5.1.4 Phase sensitive amplification

While both TWM and FWM can be used to implement a PSA with shot-noise limited NF=0 dB, we will limit our discussion in this section to the fiber-based platform and FWM as used in the work of this thesis.

In practice, a key necessity required to observe FWM is at minimum one strong pump wave, typically carrying $\sim$ W amounts of power. Since the nonlinearity in fibers is a weak effect, a high intensity is required to produce significant refractive index changes that can lead to efficient nonlinear processes. This is accomplished with the use of high power optical waves and highly nonlinear fibers in which the field-confinement is higher (large γ).

In Fig. 5.4, the input and output optical spectra in different scenarios of optical parametric amplification are shown. In the left, a single strong pump wave is launched into the fiber. Here, FWM will only occur within that single wave and no power transfer to other frequencies can take place, were it not for the presence of vacuum fluctuations.

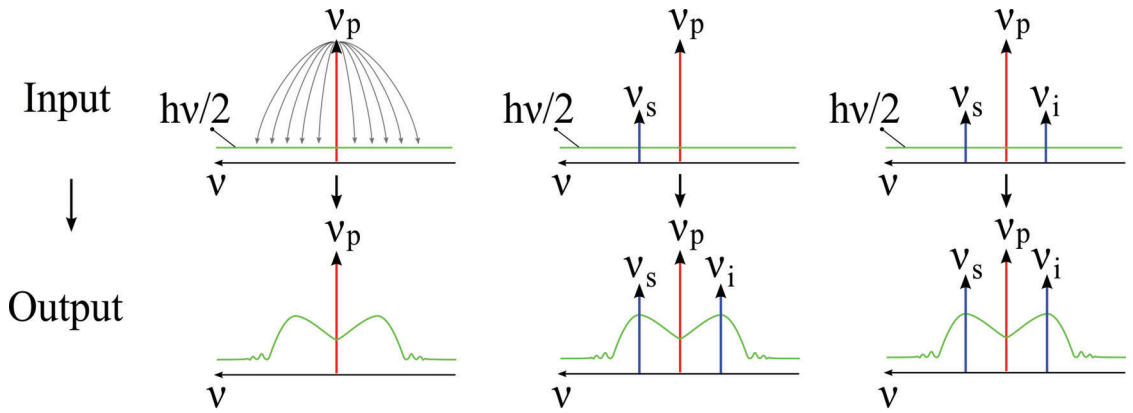

Figure 5.4: Input and corresponding output spectra from FWM in a highly nonlinear fiber. Green represents the vacuum noise power spectral density (PSD).

We discussed already in chapter 2, section 2.3.1, that vacuum fluctuations cause added noise to the amplification process. In the discussion that follows we will treat the vacuum fluctuations as an optical noise with PSD $h\nu/2$ which is present at the input to the amplifier (fiber). Although this is an incorrect description of vacuum fluctuations, it allows for intuitive derivation of the gain and NF of the parametric amplification under the assumption of high gain. The exact expressions for gain and NF are presented in section 5.1.4.

The presence of vacuum noise at the input provides a complete frequency coverage that, in this example, excites a continuous set of Fig. 5.2 c)-type FWM processes, leading to the amplified vacuum noise (AVN) spectra seen at the output. The shape of the spectra is in turn determined by the phase-matching condition of this FWM process at the different frequencies, where the highest gain corresponds to perfect phase-matching.

In the second case where we input a signal and pump wave, no signal gain would be achieved, were it not for the vacuum noise. See, a frequency at $\nu = 2\nu_p - \nu_s$ is required to stimulate FWM and since there exists an optic field component at this frequency that fulfills the phase matching condition $\phi_i = 2\phi_p - \phi_s$ (thanks to the vacuum noise) the process can be initiated. Once initiated the power builds up throughout

the fiber and the output spectra will contain the AVN, the amplified signal as well as a generated idler wave whose power will equal that of the signal at high gain. This scenario is referred to as a phase-insensitive parametric amplifier (PIA) since there will always exist a vacuum noise component that can stimulate the amplification independent of the input phases of the signal and pump.

In the third case we launch three waves into the fiber, a pump, a signal and an idler whose phase meets the phase matching condition $\phi_i = 2\phi_p - \phi_s$. This is the PSA case. Here the signal and idler fields are coherently superposed in the FWM process which results in a higher gain and lower NF. Measured output spectra from a PSA of this FWM configuration are shown in Fig. 5.5 for the discussed cases. Here the signal output power is raised by a factor 2, first when adding an uncorrelated idler and then another factor of ~ 2 when instead adding a phase-locked idler. To understand how the gain increases, consider Fig. 5.6 which shows the input fields to the amplifier in the PIA and PSA cases.

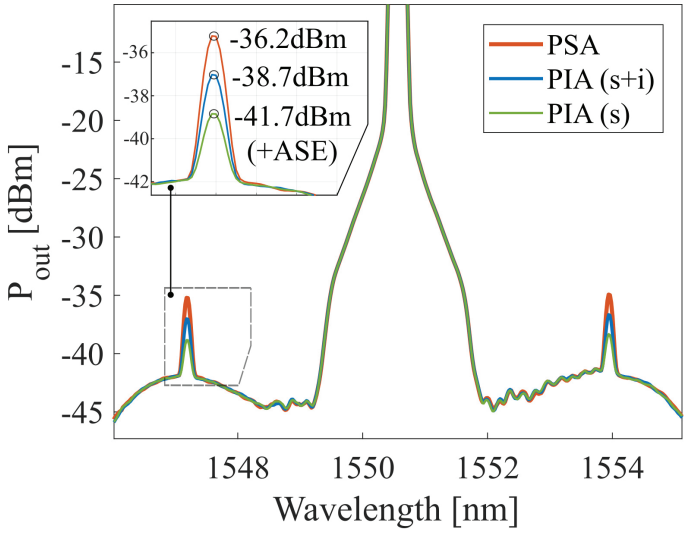

Figure 5.5: Measured PSA output spectra from [D].

Gain and noise

In the top of Fig. 5.6, only the signal is launched aside from the pump. Throughout the amplification process the fields at the two frequencies are coherently added and multiplied by the gain G, leading to the average

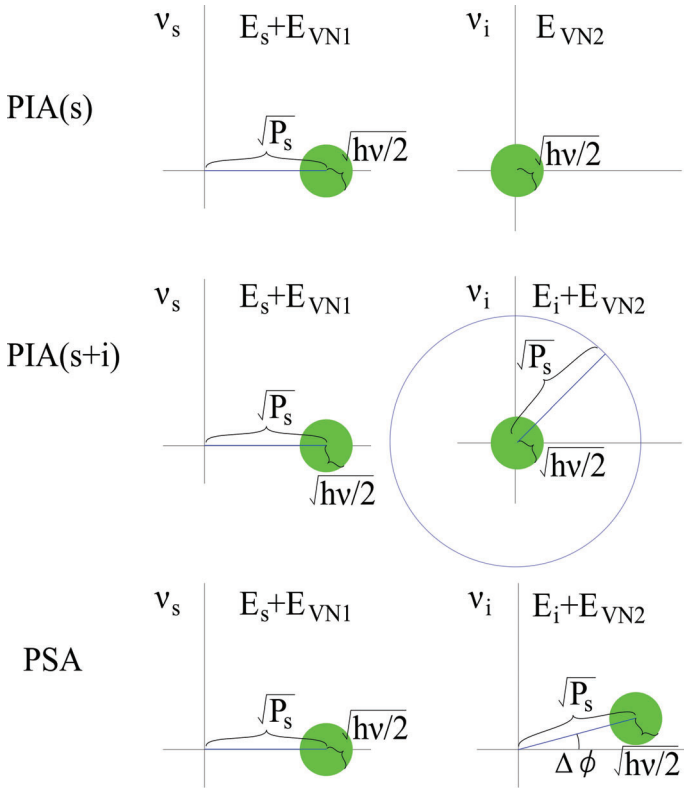

Figure 5.6: Signal and noise field representation at ν_s and ν_i in the complex plane for the different inputs; top: signal only; middle: signal and uncorrelated idler; bottom: signal and correlated idler.

output signal power

$$\begin{aligned}\langle P_{s,\text{out}}\rangle &= G\langle[E_s + E_{VN1} + E_{VN2}]^2\rangle \\ &= G\langle E_s^2 + E_{VN1}^2 + E_{VN2}^2 + 2E_sE_{VN1} + 2E_sE_{VN2} + 2E_{VN1}E_{VN2}\rangle \\ = G[\langle E_s^2\rangle &+ \langle E_{VN1}^2\rangle + \langle E_{VN2}^2\rangle + 2\langle E_sE_{VN1}\rangle + 2\langle E_sE_{VN2}\rangle + 2\langle E_{VN1}E_{VN2}\rangle] \\ &= G\left[P_s + \frac{h\nu}{2} + \frac{h\nu}{2}\right] \\ &= G[P_s + h\nu] \end{aligned} \quad (5.8)$$

where subscripts $VN1$ and $VN2$ represent the vacuum fields at ν_s and ν_i respectively and E is the optical field. The zero-averaging of the mixing terms results from the uncorrelated nature of the vacuum fluctuations. Were we to define the amplifier NF as the ratio of the optical signal to noise ratio (OSNR) at the input to the OSNR at the output, we would obtain

$$\text{NF}_{\text{PIA}} = \frac{\text{OSNR}_{\text{in}}}{\text{OSNR}_{\text{out}}} = \frac{\frac{P_s}{\Delta\nu_o h\nu/2}}{\frac{GP_s}{G\Delta\nu_o h\nu}} = 2 \quad (5.9)$$

where $\Delta\nu_o$ is an optical bandwidth for which the OSNR is defined, typically 0.1 nm. Hence, for a PIA, the gain is given by $G_{\text{PIA}} = G$ and the NF is at best 2 (3 dB). A high PIA gain is important and as high $G = G(P_{\text{pump}}, \gamma, L_z)$ is promoted by a strong pump, high nonlinearity and long fiber length L_z these parameters are of importance when building a PSA.

In the second case in Fig. 5.6 an idler wave of power P_s, uncorrelated with the signal, is added to the input. Similarly to before we get the output signal power as

$$\begin{aligned}\langle P_{s,\text{out}}\rangle &= G\langle[E_s + E_i + E_{VN1} + E_{VN2}]^2\rangle \\ &= G[\langle E_s^2\rangle + \langle E_i^2\rangle + \langle E_{VN1}^2\rangle + \langle E_{VN2}^2\rangle] \\ &= G\Big[2P_s + \frac{h\nu}{2} + \frac{h\nu}{2}\Big] \\ &= G[2P_s + h\nu]. \end{aligned} \tag{5.10}$$

However, in this case the idler power counts to the total signal input power, leading to the same NF as before:

$$\text{NF}_{\text{PIA}} = \frac{\text{OSNR}_{\text{in}}}{\text{OSNR}_{\text{out}}} = \frac{\frac{2P_s}{\Delta\nu_o h\nu/2}}{\frac{2GP_s}{G\Delta\nu_o h\nu}} = 2 \tag{5.11}$$

As such, although the output power at the signal wavelength is doubled compared to the regular PIA case, we still get the same NF.

In the third case in the figure we add a, this time correlated, idler wave at a relative phase $\Delta\phi$. This leads to the following output power

$$\begin{aligned}\langle P_{s,\text{out}}\rangle &= G\langle[E_s + E_i + E_{VN1} + E_{VN2}]^2\rangle \\ &= G[\langle(|E_s| + |E_s|\cos\Delta\phi)^2 + |E_s|^2\sin^2\Delta\phi\rangle + \langle E_{VN1}^2\rangle + \langle E_{VN2}^2\rangle] \\ &= G[P_s + 2P_s\cos\Delta\phi + P_s(\cos^2\Delta\phi + \sin^2\Delta\phi) + h\nu] \\ &= 2GP_s[1 + \cos\Delta\phi] + Gh\nu \end{aligned} \tag{5.12}$$

From this we extract the phase sensitive gain as

$$G_{\text{PSA}} = 2G_{\text{PIA}}[1 + \cos\Delta\phi] \tag{5.13}$$

and accounting for both signal and idler power, the NF becomes

$$\text{NF}_{\text{PSA}} = \frac{\text{OSNR}_{\text{in}}}{\text{OSNR}_{\text{out}}} = \frac{\frac{2P_s}{\Delta\nu_o h\nu/2}}{\frac{2GP_s[1+\cos\Delta\phi]}{\Delta G\nu_o h\nu}} = \frac{1}{\frac{1}{2}[1 + \cos\Delta\phi]} \geq 1. \tag{5.14}$$

As such, for phase-locked pump, signal and idler $\Delta\phi = 2\phi_p - \phi_s - \phi_i = 0$, a NF of 1 (0 dB) can be obtained. Note that the stated gains are referencing the output signal power at ν_s to the input signal power at ν_s.

Exact expressions

Although the above derivations of gain and NF are intuitive and to some extent correct, they are simplifications. To rigorously derive gain and NF for an optical amplifier one should take to a quantum mechanical description of light [27]. If done correctly, the actual gain of the PSA becomes [26]

$$G_{\mathrm{PSA}} = 2G - 1 + 2\sqrt{G(G-1)}\cos(\Delta\phi) \simeq 2G_{\mathrm{PIA}}[1+\cos(\Delta\phi)], \quad G > 10, \quad (5.15)$$

and the NF

$$\mathrm{NF}_{\mathrm{PSA}} = 2\frac{2G-1}{G_{\mathrm{PSA}}} \simeq \frac{1}{\frac{1}{2}[1+\cos\Delta\phi]}, \quad G > 10, \quad (5.16)$$

i.e., our previous expressions apply at high gain.

It should also be said that the NF is defined, not with respect to input-output OSNR, but with respect to the signal to noise ratio (SNR) of shot-noise limited detection (with unity quantum efficiency) [26]. Doing the calculation will result in the same expressions as above, assuming the PSA output signal is coherently received. Hence, when the PSA NF reaches 0 dB, that is what we call an ideal shot-noise limited PSA NF. Although the reference to OSNR is useful, the NF cannot be defined with respect to the input vacuum noise power since the vacuum noise before amplification do not actually carry any optical power.

The gain ambiguity

Unfortunately, since the FWM-PSA deals with both signal and idler waves with regards to amplification and NF there is room for ambiguity and differing conventions when defining gain and NF. Talking about gain one may imply the output signal power at ν_s referenced to the input signal power at ν_s, or it may be the output signal power at ν_s to the input signal plus idler power that is implied, i.e., the total input power at both ν_s and ν_i. The same applies for the NF which may lead to the interpretation that NF$= -3$ dB which is nonphysical.

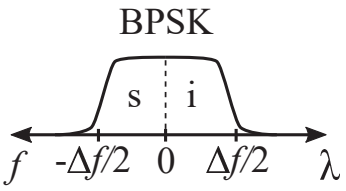

Figure 5.7: Degenerate BPSK signal spectrum.

This becomes especially important when considering e.g. the degenerate signal case (Fig. 5.2 d)) where there is only the one input signal. In this case, there is no PIA(s) (Fig. 5.6) scenario, for which the PIA gain is typically defined $G_{\mathrm{PIA}} = G$. Instead, the two halves of the signal can be seen as signal and idler (see Fig. 5.7). With this interpretation the PSA gain defined above relates the output power in one half of the output signal spectrum to the input power in one half of the input signal spectrum. The gain in this case thus also describes the total output to input power. The NF is also the same, when taking both the added signal power and noise power contained in the idler part into account.

5.2 Phase sensitive amplification of data

The condition for phase sensitive amplification has been established as $\Delta\phi = 0$. For the work in this thesis, this implies that $\phi_s = 2\phi_p - \phi_i$ for the two-mode, single pump PSA (Fig. 5.2 c)) in papers [C,D] and $2\phi_s = \phi_{p1} + \phi_{p2}$ for the one-mode, dual-pump PSA (Fig. 5.2 d)) in paper [E].

To achieve phase sensitive amplification of coherent modulation formats, such as binary phase-shift keying (BPSK) and quadrature phase-shift keying (QPSK), wherein data is encoded in the signal phase ϕ_s, some restrictions follow. These restrictions for the two types of PSA will be discussed in the sections below.

5.2.1 The two-mode PSA

For the single-pump, two-mode PSA, the typical solution is to encode the idler wave with the conjugated data, so that $\phi_i = -\phi_s$. In this case both signal and idler waves are generated at the transmitter and propagated alongside each other through the link. The alternative would be to modulate the pump with the signal data. For practical reasons in a communication link, the pump must be created at the receiver which makes this alternative implausible.

The idler can be generated the same way as the signal, using a laser at the idler wavelength and a modulator that encodes the conjugate data. While possible, the radio-frequency (RF) frequency response of the two

modulators and waveform generators must match to obtain perfect signal and idler copies, something which may be challenging in practice. In addition, the two free-running lasers at the signal and idler wavelength, respectively, will be uncorrelated and severely impact the phase-locking needed in the receiver lest they exhibit minimal phase noise. Another way to automatically create a conjugated signal copy at the idler wavelength, with correlated phase noise, is via the use of FWM in a copier stage, first proposed in [105].

Copier scheme

A free-space optical communication link employing a transmitter side copier-stage is shown in Fig. 5.8. Here, the data-encoded signal is combined with a strong pump-wave in a wavelength division multiplexer (WDM) before being launched into the nonlinear fiber. Here the fiber acts as a PIA which creates a perfect conjugate idler as $\phi_i = 2\phi_{p_{Tx}} - \phi_s$. Note also that the AVN at the signal and idler is correlated due to the FWM process. The pump is filtered away and signal and idler are transmitted through the channel.

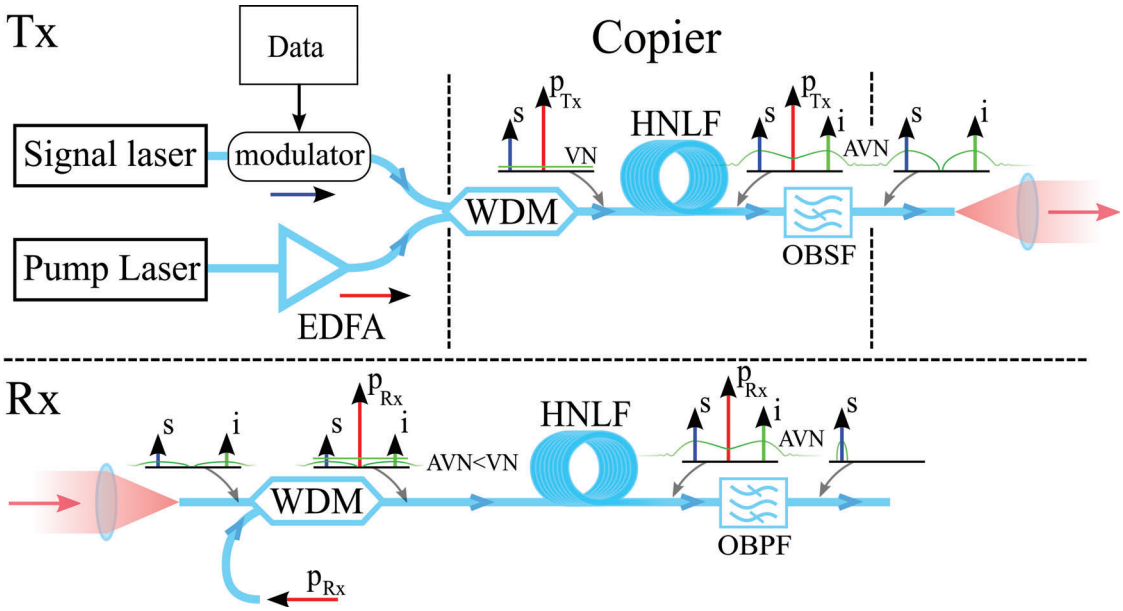

Figure 5.8: A free-space communication link with a copier-stage at the transmitter and PSA at the receiver. WDM: wavelength division multiplexer; HNLF: highly nonlinear fiber; OBPF: optical band-pass filter; OBSF: optical band-stop filter; VN: vacuum noise; AVN: amplified vacuum noise.

At the receiver the signal and idler are combined with a strong receiver-side pump wave before being sent into the PSA (the nonlin-

ear fiber). To reach a shot-noise limited NF it is crucial that the AVN generated at the transmitter has been attenuated below the vaccum noise level by the link loss, so that the noise at signal and idler wavelengths is uncorrelated. For deep-space links this will always be the case.

The relative phase at the PSA is in this case $\Delta\phi = \phi_s + \phi_i - 2\phi_{p_{Tx}} = 2(\phi_{p_{Tx}} - \phi_{p_{Rx}})$, hence, the impact of the phase-encoded data is cancelled and the remaining challenge is to compensate the relative phase of the transmitter and receiver continuous wave (CW) pumps.

The copier-scheme has been used extensively for low-noise PSA demonstrations using FWM in fiber [26, 99, 105], among them the 1.1 dB NF in [28] and the 1 photons per information bit (PPIB) receiver shown in [34]. There are, however, several implementation challenges pertaining to the use of a copier-stage and the two-mode PSA at large for space-to-ground communications.

Practical challenges

We have already emphasised the need for simple, redundant and power-efficient space-born optical transmission systems. The copier-stage, relying on a high-power pump, is far from efficient with current fiber-technologies, typically needing high power levels, on the order of Watts. In addition, a high power booster amplifier will always be needed to reach high enough launch powers. With or without copier-stage, the transmitter will still be burdened with additional complexity due to the need of a transmitted signal-idler pair.

Another challenge of a dual-wavelength signal pertains to the large-area receiver implementations we discussed in chapter 4. Except for the use of adaptive optics (AO), both multi-mode fiber (MMF) and multi-aperture reception is primarily only compatible with a single wavelength as discussed in section 4.6.3. This is with regards to optical coherent combining as opposed to digital combining which would require one PSA per channel.

In the case where PSA-pre-amplification is of interest for a ground-to-space link, the two-mode PSA is more viable. In such a scenario, we can expect the use of a smaller receive-aperture and single channel reception, avoiding the need for coherent combining. The remaining issue would be to make the PSA-amplification in the receiver power efficient and of as low complexity as possible. One step towards such an implementation is to move from bulky fiber-based systems to an integrated photonics platform [106].

5.2.2 The one-mode PSA

For the one-mode PSA (shown in Fig. 5.2 d)), there is no idler that can cancel the phase-modulated data to obtain $\Delta\phi = 2\phi_s - \phi_{p1} - \phi_{p2} = 0$. The factor of 2 in front of ϕ_s does however allow one specific type of phase modulation, namely BPSK and other single-quadrature modulation formats. In BPSK, $\phi_s = \phi_{s,\text{noise}} + \phi_{s,\text{data}}$, where $\phi_{s,\text{noise}}$ is the phase noise caused by the used laser and the free-space channel and $\phi_{s,\text{data}} = 0, \pi$ is the signal data. Using this, the relative phase becomes $\Delta\phi = 2\phi_s - \phi_{p1} - \phi_{p2} = 2\phi_{s,\text{noise}} - \phi_{p1} - \phi_{p2}$, where any 2π phase offsets have been omitted since they are irrelevant to the phase sensitive amplification. We see that the modulated data is cancelled and the remaining relative phase is left to the receiver phase-locking system to compensate.

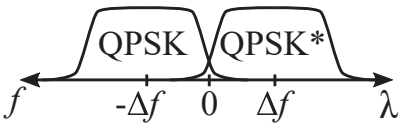

Figure 5.9: Closely spaced signal and idler carrying QPSK data.

Although the use of the one-mode, dual-pump PSA is limited to amplification of a single quadrature, it is relatively simple to alter the PSA into a dual-pump, two-mode PSA as in Fig. 5.2 b) to enable the use of arbitrary modulation formats. This can be done in practice without complicating the transmitter beyond that of a conventional, single-wave system, simply by producing adjacent signal and idler in the same modulator, see Fig. 5.9. This is done in paper [E] to demonstrate the compatibility of the single-wave, dual-pump PSA with arbitrary formats. The closely spaced signal and idler can simply be regarded as one signal wave, albeit with twice the bandwidth.

Measured constellation symbol densities for both a BPSK signal and the QPSK signal shown in Fig. 5.9, after pre-amplification using an erbium doped fiber amplifier (EDFA) (PIA) as well as a dual-pump, one-mode PSA, are shown in Fig. 5.10. In each case the received power is the same and it can be seen that the use of the PSA results in constellations of lower noise than for the EDFA. One can also observe the single-quadrature amplification effect of the degenerate BPSK signal which clearly indicates a squeezed output state in phase.

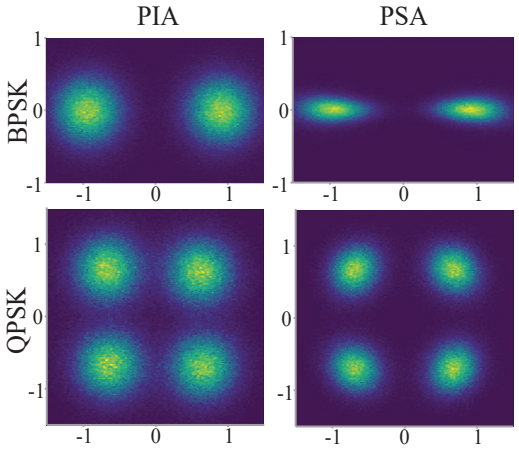

Figure 5.10

The phase-squeezing of noise happens as also the vacuum noise experiences single-quadrature amplification. In fact, the out-of-phase noise is de-amplified in the PSA as $G_{\mathrm{PSA}}(\Delta\phi = \pi) \approx 1/G_{\mathrm{PSA}}(\Delta\phi = 0)$ at high PIA gain. Phase squeezing is something of interest to quantum applications since it can reduce the uncertainty in one quadrature below the vacuum level, at the expense of excess noise in the other quadrature [62]. This feature was for instance used to obtain sensitive detection of gravitational waves in the Laser Interferometer Gravitational-Wave Observatory (LIGO) [107].

Practical challenges

The work in [E] is the first to demonstrate a below 3 dB NF for the one-mode, dual pump PSA. The reason for the absence of prior demonstrations is the added challenges that comes with two strong pump waves. The presence of two pumps enables multiple of the FWM-processes shown in Fig. 5.2, whereas it is only the process in d) that we desire. This will lead to PIA processes creating both pump-idlers and signal-idlers at new frequencies. Most detrimental to the NF are the higher order idlers created via the two-mode, single-pump FWM-process with respect to each pump (see Fig. 5.11). These FWM processes implies that the vacuum noise at these wavelengths add to the final noise at the signal wavelength throughout the amplification, severely degrading the NF. One can circumvent this by injecting correlated signal-idlers at these wavelengths but that defeats the purpose of a single-wave solution.

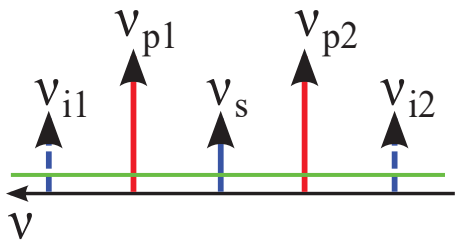

Figure 5.11: FWM with higher order idlers.

The other way to circumvent the issue is to ensure that the phase-matching condition is unfulfilled for the undesired FWM-processes while maintaining phase-matching for the desired dual-pump, one-mode PSA. How to accomplish this has been investigated in [108–110] where it is found that a wide pump separation is needed ($40 - 50$ nm) as well as a center wavelength at or just below the zero-dispersion wavelength. While this approach enabled the demonstration of 1.7 dB NF in [E], the issue limits the band of wavelengths for which low-noise amplification can be obtained. This implies that for a given wavelength the fiber zero-dispersion wavelength need to be tailored. While this is not a huge concern for a monochromatic deep-space link it limits the flexibility of

the PSA, e.g., in comparison to an EDFA.

5.3 Phase-locking of PSAs

Perhaps one of the most challenging aspects of making PSAs feasible for real-world low-noise communications is that of phase-locking. In the record-low NF demonstration in fiber [28] and for PPLN [29] signal and idler-coherent pump waves were used to circumvent this issue. While that works in the lab, enabling low-noise PSA-pre-amplification in practical link requires compensation of relative frequency drift and phase noise between the pump generated at the receiver and the received waves to be amplified. This requires some kind of laser locking system and will always infer a finite locking penalty to both the gain and NF of the PSA.

The penalty to gain and NF can be understood in terms of the locking efficiency, which we define similarly to the combining efficiency in chapter 4, i.e. the ratio of total output power at relative phase $\Delta\phi$ to the total output power at $\Delta\phi = 0$, as

$$\eta = \frac{G_{\mathrm{PSA}}(\Delta\phi)}{G_{\mathrm{PSA}}(\Delta\phi = 0)} = \frac{1}{2}[1 + \cos\Delta\phi], \quad \langle\eta\rangle = \frac{1}{2}[1 + e^{-\sigma^2_{\phi_e}/2}]. \quad (5.17)$$

The expressions for the instantaneous and time-average efficiency is the same as that for the coherent combining from chapter 4. In fact, the coherent superposition of spatial channels is very similar to the coherent superposition of spectral channels occurring in a PSA. The residual phase error variance $\sigma^2_{\phi_e}$ can be treated as described in chapter 3. The NF degradation due to imperfect locking is given as $1/\eta$, yielding SNR $\propto \eta$ for the communication link, meaning the bit error rate (BER)-impact of imperfect locking is the same as for the coherent combining system as described in section 4.6.1.

Since the locking penalty is only one of several other penalties, like Raman-scattering-induced noise [111] and pump-transfer noise [112,113], it can be difficult to quantify it. One way to measure both the phase error variance and the efficiency is provided by the measurement of the time-average extinction ratio $\langle e\rangle$. The extinction ratio is defined as $G_{\mathrm{PSA}}(\Delta\phi = 0)/G_{\mathrm{PSA}}(\Delta\phi = \pi)$, hence $\langle e\rangle$ is obtained by measuring the averaged PSA signal output power when locking the phase to constructive and destructive gain respectively and dividing the result. This is the same as

$$\langle e\rangle = \frac{\langle\eta\rangle}{1 - \langle\eta\rangle} = \frac{1 + e^{-\sigma^2_{\phi_e}/2}}{1 - e^{-\sigma^2_{\phi_e}/2}} \quad (5.18)$$

from which the efficiency and phase variance can be extracted as

$$\langle \eta \rangle = \frac{\langle e \rangle}{1 + \langle e \rangle}, \quad e^{-\sigma^2_{\phi_e}/2} = \frac{\langle e \rangle - 1}{\langle e \rangle + 1}. \tag{5.19}$$

Since the final phase-locking has traditionally employed a dither-optical phase locked loop (OPLL), switching between phase sensitive gain and phase sensitive attenuation is easily done by error signal inversion, i.e. by switching the sign in front of g in Eq. (3.2) (or g_s in Eq. (3.3)).

As for any control system, the trade-off between OPLL SNR and bandwidth is apparent also in the context of PSAs. Hence, for the purpose of deep-space communications where the received signals and possible idler waves are expected to be weak, even when collected using a large reception area, the bandwidth of the PSA locking system must be limited to reach adequate SNR. This has nurtured the interest for the use of low phase-noise lasers in the PSA context and as the development of such lasers has matured over the years, so has the PSA locking system implementations, enabling low-noise PSA-pre-amplification at lower and lower received powers.

Presented in the sections below are the main PSA pump-locking implementations that have been used for practical link demonstrations, both in TWM-PSAs and different FWM-PSAs.

5.3.1 Signal tapping

Although there are a slight variation of locking systems for the PPLN-based TWM-PSAs, the one shown in Fig. 5.12 from [38] and [102] is fairly representative.

Here, a conjugate signal-idler wave-pair carrying the signal data is received in the top left before 10% of the power is tapped off for the purpose of pump-locking (i.e. a direct NF penalty of 0.5 dB). The PSA in this case relies on the TWM process shown in Fig. 5.3 c), thus requiring a phase-locked pump at the sum of the signal and idler frequency. To achieve this, the tapped signal-idler pair is optically amplified and filtered and sent into a PPLN stage where the two amplified waves acts as pumps in a sum frequency configuration (Fig. 5.3 a)) to produce a CW tone at the sum-frequency. The tone is CW since the signal and idler are conjugated copies. A local pump laser roughly centered between the signal and idler frequencies is split, where one wave is frequency-doubled using second harmonic generation in another PPLN stage before being interfered with the CW tone generated by the tapped and amplified

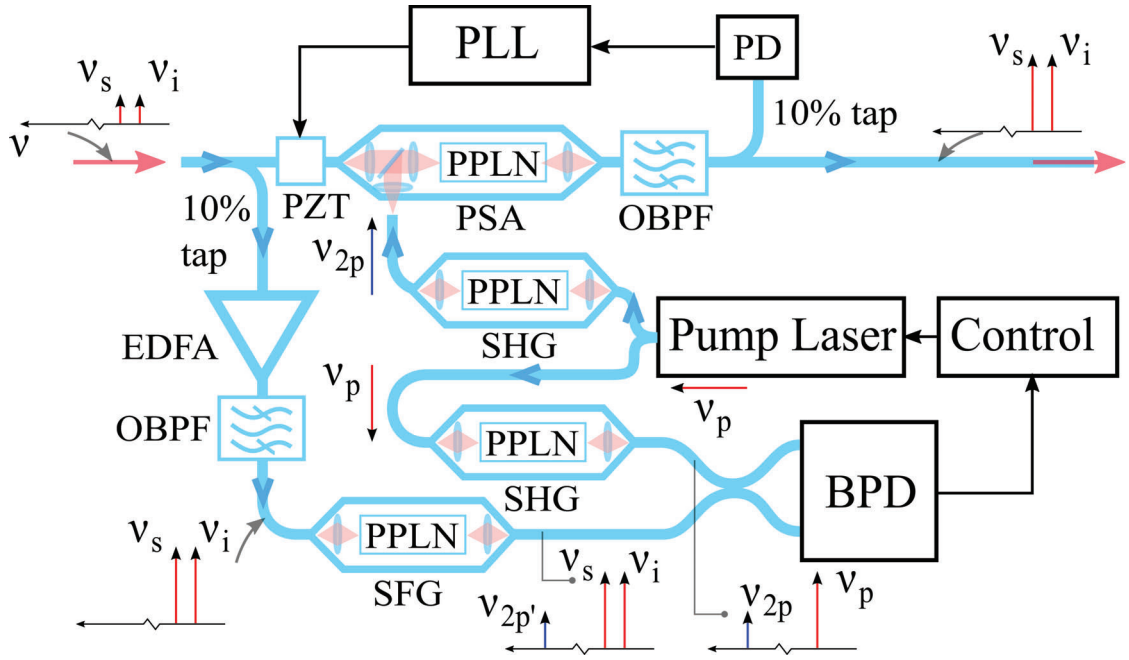

Figure 5.12: A PSA receiver setup using the PPLN platform, enabled by an OPLL stage involving several PPLN stages with second harmonic generation (SHG) and sum frequency generation (SFG), balanced detection (BPD) and pump laser control. PZT: piezeo-electric transducer.

signal-idler pair. The subsequent balanced detection of this interference provides a measure of the phase-error between the pump laser and received waves which via a control loop (OPLL) is used to adjust the phase and frequency of the pump laser such that the phase error is compensated. The other part of the now phase-locked pump is sent through another second-harmonic PPLN stage to frequency double the light into the pump for the PSA. Due to relative phase fluctuations between the different fiber paths a slow dither phase locked loop (PLL)/OPLL is used to stabilize the final phase using a piezo-electric fiber stretcher (acting as phase-shifter).

The practical feature of this setup is that the locking can be accomplished while only receiving signal and idler, which for the TWM PSA process used could be spaced close enough to act as a single-wavelength signal (as in [102]). The apparent downside here is the 10% tap which incurs a direct loss of the received power. In principle a smaller tap, e.g. 1% could be used but the OPLL SNR would receive a proportional penalty. Typical laser linewidths used in the system in [102] are on the order of kHz and dictates the necessary OPLL bandwidth. The use of optical pre-amplification of the tapped signal as well as the need for sum

frequency generation will produce optical noise which will limit the SNR of the balanced detection. This will together with the phase noise of the used lasers limit how weak received powers the system can operate for, i.e. the OPLL sensitivity. In fact, the focus of the work in [102] is on implementing this type of PSA as an inline amplifier for a fiber based link where low received powers can be avoided.

5.3.2 Pump carrier recovery

For demonstrations using the single-pump, two-mode FWM, fiber based PSA, the copier stage is often employed. As there is residual pump power available at the transmitter after this stage, part of the leftover pump is transmitted alongside signal and idler as a carrier reference for pump-locking at the receiver. The pump reference counts to the total received power however, as such the target for the demonstrations in [37] and [C] was to minimize the power needed in the pump reference to operate the PSA efficiently.

Using optical injection locking

Common to the demonstrations in [30, 34] is to use the received pump carrier reference for optical injection locking of the receiver-side pump laser [36]. A typical setup is shown in Fig. 5.13.

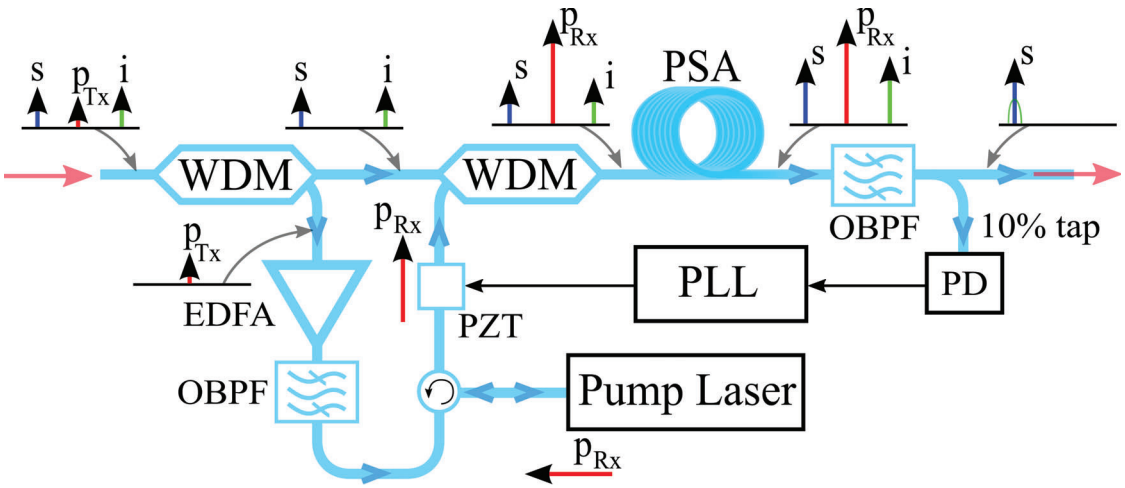

Figure 5.13: A PSA receiver setup using highly nonlinear fiber, enabled by an optical injection-locking (OIL) stage for pump-carrier recovery and a slow PLL.

Here, the received pump reference is separated from the signal and idler using a WDM before being optically amplified, filtered and injected

into the pump laser via a circulator. The short version of OIL implies that the injected wave interferes with the laser field inside the laser cavity, effectively promoting the subsequent build up of a laser field that is in phase with the injected light. The injected light must however compete with the optical AVN present in the laser cavity, as well as the AVN from the EDFA, to enforce the desired phase upon the laser. However, as long as the laser AVN is larger than that caused by the EDFA, the optical amplification of the reference will help increase the OIL SNR. When locked to the injected light the pump laser is phase-locked to the signal and idler and is circulated out through a piezo-electric fiber stretcher, compensating the relative phase fluctuations between paths before combined with signal and idler in a WDM at the input to the PSA. The fiber stretcher is again driven by a slow dither-OPLL.

The use of OIL-based pump reference recovery has demonstrated efficient locking of the PSA at received pump-reference powers ≥ -72 dBm in [34]. At this power, the presence of the pump reference together with locking penalties constituted a NF penalty of 0.3 dB at signal-idler powers of ~ -60 dBm. The performance was mainly limited by the receiver side pump laser with a linewidth of 50 kHz.

Using an OPLL

Instead of using OIL for pump carrier recovery one can use an OPLL as shown in Fig. 5.14. Such a system was first demonstrated in paper [H] to which paper [C] is an extension with focus put on the OPLL laser locking system indicated in the dashed box in the figure.

Just like for the OIL system above, the pump reference is separated and sent to interfere directly with a receiver side pump laser. The dashed box in the figure is in principle the same system we used as example for explaining the dither-OPLL in chapter 3, Fig. 3.1, including the laser frequency control. The only difference between the system in chapter 3 and the one in Fig. 5.14 is that the dither and phase compensation is divided upon phase modulator 2 and 1, respectively, and that both 50/50-coupler outputs are detected in a balanced photo-detector. In this setup, the much stronger wave from the pump laser acts as a strong local oscillator (LO), providing coherent detection gain to the balanced detection. In the case of a perfect detector (unity quantum efficiency), this system enables shot-noise limited detection of the phase error. The separation of the dither from the overall phase compensation in PM1 also removes the dither penalty from the residual phase error variance in the

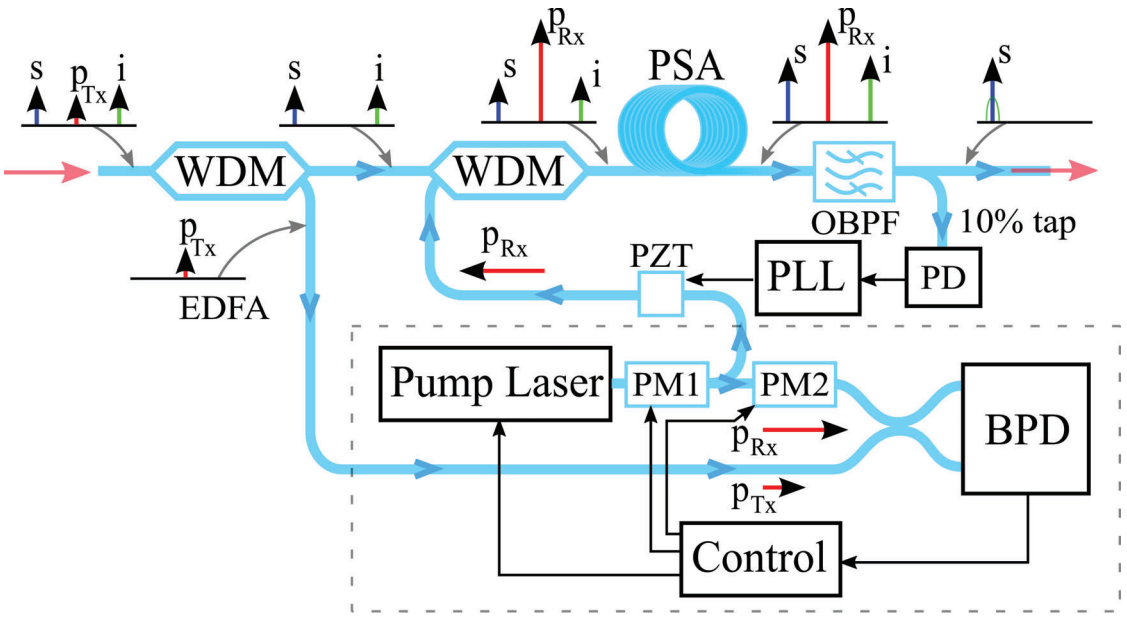

Figure 5.14: A PSA receiver setup from [C] using highly nonlinear fiber, enabled by an OPLL stage for pump-carrier recovery and a slow PLL. PM: phase modulator.

PSA. A fiber stretcher together with a slow dither-OPLL is, again, used to compensate relative phase fluctuations between paths. In principle, the use of PM1 can be replaced by proportional frequency control of the laser directly, thus avoiding one source 2π-phase slips.

The use of this OPLL-based pump reference recovery enabled efficient PSA locking at received pump reference powers ≥ -83 dBm. At this power, the presence of the pump power results in negligible NF penalty at received powers of ~ -60 dBm. The phase-locking penalty was moreover estimated to be 0.2 dBm. The system in this case was primarily limited by the pump lasers at both transmitter and receiver which featured linewidths on the order of 100 Hz.

5.3.3 Local pump locking

The setups discussed so far has in all cases relied on a slow dither-OPLL to ensure the compensation of relative phase fluctuations. The dither-OPLL we discussed in chapter 3 utilized the interference in a 50/50-coupler to create a phase-error proportional error signal via dithering. Indeed, the PSA phase dependence is physically near identical to that of interference in the 50/50-coupler (c.f. Eq. (3.1) and Eq. (5.13)). Hence by dithering the pump wave at the input to the PSA a phase-error proportional error signal can be extracted from the amplified signal

power. Moreover, if the dither-OPLL is fast enough, and the phase noise between free-running pump and received signal is small, then the use of this dither-OPLL would be sufficient to lock the PSA by itself. This is the premise in the local pump locking scheme we will discuss here and avoids the need for either tapping the signal power before amplification or a co-transmitted pump carrier reference.

The work in paper [D] demonstrates the local pump locking scheme in a PSA-based receiver using the single-pump, two-mode FWM configuration. The setup is illustrated in Fig. 5.15.

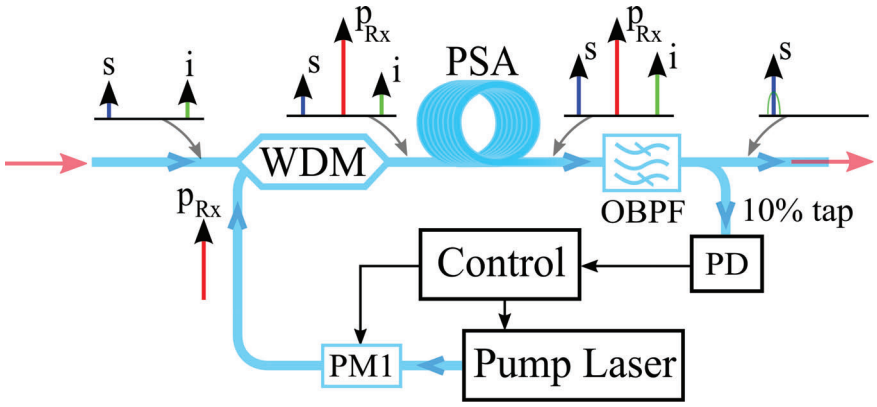

Figure 5.15: A PSA receiver setup from [D] using highly nonlinear fiber, enabled by an OPLL stage for local-pump locking.

Here, the received signal and idler waves are immediately combined with the local pump wave which is phase-locked based on the dither-OPLL that feeds on the error signal extracted at the 10% tap after amplification. This scheme was also employed in paper [E] for the dual-pump, one-mode PSA whose setup is shown in Fig. 5.16. As a note, when altering the signal bandwidth, the discussion in section 4.6.2 also holds true for the local pump-locking OPLL, even though in this case, its SNR is limited by both Noise-Noise and Signal-Noise beating.

The main challenge of the local pump locking scheme is the loop delay imposed on the OPLL due to the length of the nonlinear fiber PSA which measures up to 600 m in [D] and 350 m in [E] which adds several microseconds to the overall loop delay. The problem with loop delay was explored in chapter 3 where it was demonstrated how loop instability is directly connected to a combination of large loop delay and large loop bandwidth. Hence, the use of low linewidth lasers is crucial to operate the system at a low enough bandwidth to avoid instability. This was enabled in [D,E] thanks to the linewidths of 100 Hz for the lasers used. In [D] the system could lock at received signal-idler power down

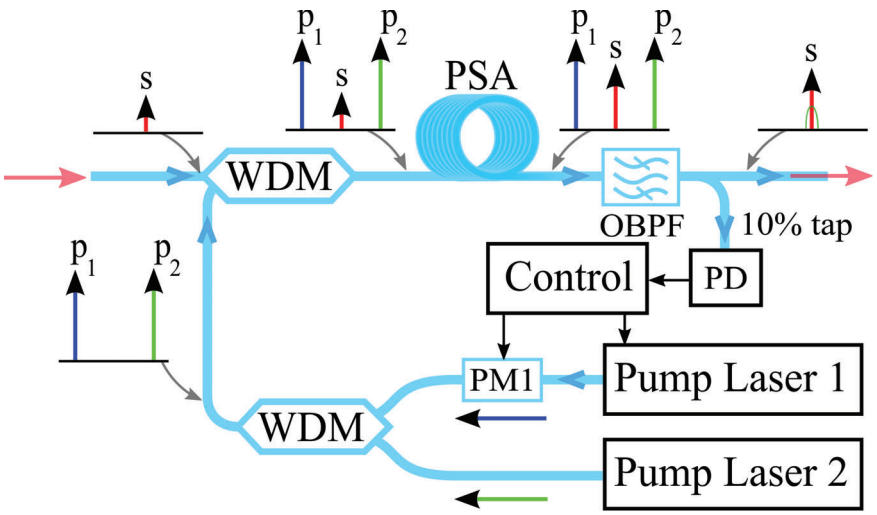

Figure 5.16: A PSA receiver setup from [E] using highly nonlinear fiber, enabled by an OPLL stage for local-pump locking.

to −65 dBm with at best 0.3 dB locking penalty, mainly limited by loop delay. Meanwhile in [E] the system could maintain locking down to −66 dBm with a stable locking penalty of 0.25 dB.

The local pump locking scheme is very appealing both from a performance as well as a complexity point of view as it removes the NF-penalties associated with previous solutions and the need for a pump reference. Specifically, the single-wave system in [E] is attractive for deep space to earth links as it is entirely compatible with a typical space-born single-wave transmitters and the large area receiver implementations discussed in chapter 4. While the implementation is currently limited by the fiber length of the PSA, this is something that hopefully can be remedied by the transition from a fiber-based platform to the use of integrated photonics [106] where loop delays would be significantly reduced. This would also ease the restrictions on the low-noise properties of the lasers. However, it should be said, as has been the point at many instances throughout this thesis, that a low phase noise allows for a small OPLL bandwidth and hence the possibility to lock at lower received powers (Eq. (3.13)).

CHAPTER 6

Conclusion & Future outlook

After many detailed discussions throughout the chapters of this thesis we now take a step back to consider the knowledge we have garnered. In a decade of rapid development of laser-based space communications, this thesis aims to further the capability of such systems in pushing high data rate-enabling, sensitive receivers as a remedy for the bottle-neck of current deep space communications. Specifically, the thesis targets the implementation of large optical receivers together with coherent reception and phase sensitive amplifier (PSA)-pre-amplified detection as the avenue towards these goals. In this regard, the work contained herein has demonstrated important practical steps towards the realization of such systems.

For practical PSA-preamplified ground-based receivers the work in papers [C-E] has both helped improve the phase-locking sensitivity for efficient low-noise amplification[C] as well as having significantly reduced the implementation complexity via the local pump-locking optical phase locked loop (OPLL) in [D] and the single-wave solution presented in [E]. These achievements represent important steps towards implementation in practical systems, for which the PSA in [E], could in principle already be employed.

In the arguably, at least as important large-area receiver aspect of realizing high-speed sensitive links, the work in papers [A,B] show promising results with regard to coherent combining as an approach to scaling

up the receiver size. The work in [A] demonstrates the possibility to efficiently coherently combine individually received data-modulated signals at down to −80 dBm signal power. This in relation to typical PSA sensitivities at around −60 dBm (at 10 Gbaud QPSK) provide ample margin to extend the receiver area via multi-aperture or multi-mode reception while maintaining high receiver efficiency. Paper [B] puts this result into context for a realistic downlink through turbulent atmosphere and highlights important aspects regarding the efficiency and sensitivity of multi-aperture and multi-mode receiver solutions.

As practical issues are engineered away, fundamental limits will remain and what pertains to the implementation of active compensation of both phase-locked waves in a PSA and spatial decoherence in a large-area receiver is the signal to noise ratio (SNR)-bandwidth trade-off that has themed the content of this thesis. In the end, the finite phase noise from lasers and atmosphere dictates the reach and speed of the deep-space link, lest they somehow are absolved of their impact.

Looking forward

There are still a number of practical considerations and additional work required along the road to implementing large-area PSA-pre-amplified receivers for deep space communications. These additional steps concern limitations such as loop delay for local pump-locking, the optimal error signal detection scheme for coherent combining and practical demonstrations in real free-space channels. Below we briefly discuss some of the important considerations left for the future.

Integrated photonics

The idea of transitioning from a fiber-based platform to a photonic-integrated solution is attractive in many aspects concerning both the implementation of PSAs as well as coherent combining architectures. With respect to the PSA, this can provide a number of benefits, ranging from smaller footprint devices, increased device production volume, larger freedom in dispersion engineering, higher

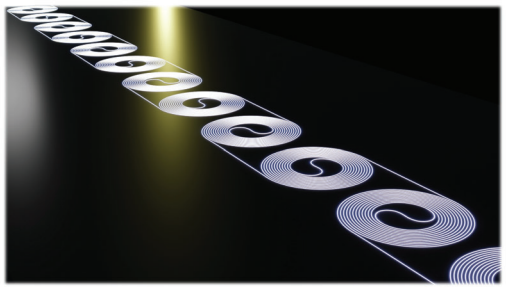

Figure 6.1: Illustration of a Si_3N_4-waveguide used for phase sensitive amplifiaction. Waveguide width is $\sim 2\,\mu m$.

nonlinearity and reduced detrimental effects such as Raman and stimulated Brillouin scattering which fundamentally limits the practical noise figure (NF) from reaching 0 dB.

Currently, important progress is being made in realizing efficient four-wave mixing (FWM)-processes in Si_3N_4 waveguides as demonstrated in [106]. The employed approach at making long but compact amplifier waveguides is shown in Fig. 6.1. The main limitations of these fabricated devices remain in the fiber to chip coupling loss as well as waveguide loss to reach a low black-box NF. Were these challenges to be overcome the Si_3N_4-PSA could enable record-low NF and potentially solve the higher order idler problem for the PSA in [E] with appropriate dispersion design. A reduction in the required pump power would also be necessary to make this kind of device attractive for an optical terminal aboard a space-craft.

The work on periodically poled lithium-niobate (PPLN)-PSAs also belong to this category of integrated solutions with similar benefits. In fact the work in [102] would significantly benefit from the local pump-locking solution which could enable this type of PPLN-PSA as a highly sensitive single-wave pre-amplified receiver that does not suffer from higher order idlers like the FWM in [E]. Other integrated platforms of highly nonlinear material such as AlGaAs are also being investigated [114].

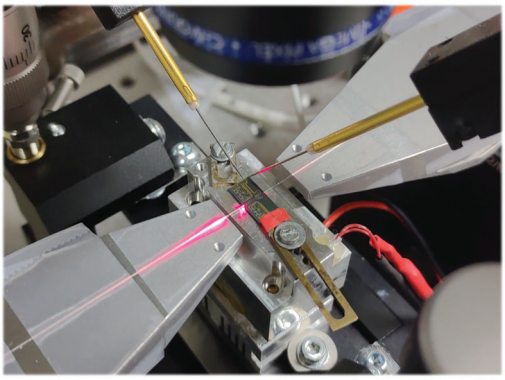

Figure 6.2: Photo of a fabricated coherent combining device under characterization.

One important benefit gained from any integrated solution is the short PSA length and thus loop-delay as opposed to fiber. This would not only reduce the loop delay-induced locking penalty reported in [D,E] for local pump-locked PSAs but also allow the use of lasers with larger linewidths. However, as has been discussed, lower linewidth lasers will always be preferred when locking at low SNR.

Turning to the prospect of chip-based coherent combining we have already seen important progress being made in demonstrations such as [95] and [96] where in the latter the combiner was realized in the silicon photonics platform with thermal heaters as phase-shifters. The integrated combiner solutions simplifies up-scaling

of the combining cascade and provides simple control of heaters via electrical interfacing.

Although not yet reported, we are currently working on our own design and implementation of such coherent combining chips in Si_3N_4. A photo of such a chip in the characterization stage is shown in Fig. 6.2. An illustration of the device is also shown in Fig. 6.3. The target is to demonstrate efficient up-scaling to 8-channel combining of data-modulated signals at low power. The use of Si_3N_4 also allows for future implementation of a combiner and PSA on the same chip. Preliminary results indicate large enough phase-shifter bandwidths (few kHz) for phase-compensation. Cross-talk between heaters is however a problem and would require improved design for future devices. An alternative to heating-based phase-shifters, that likewise offer minimal loss, is of high interest.

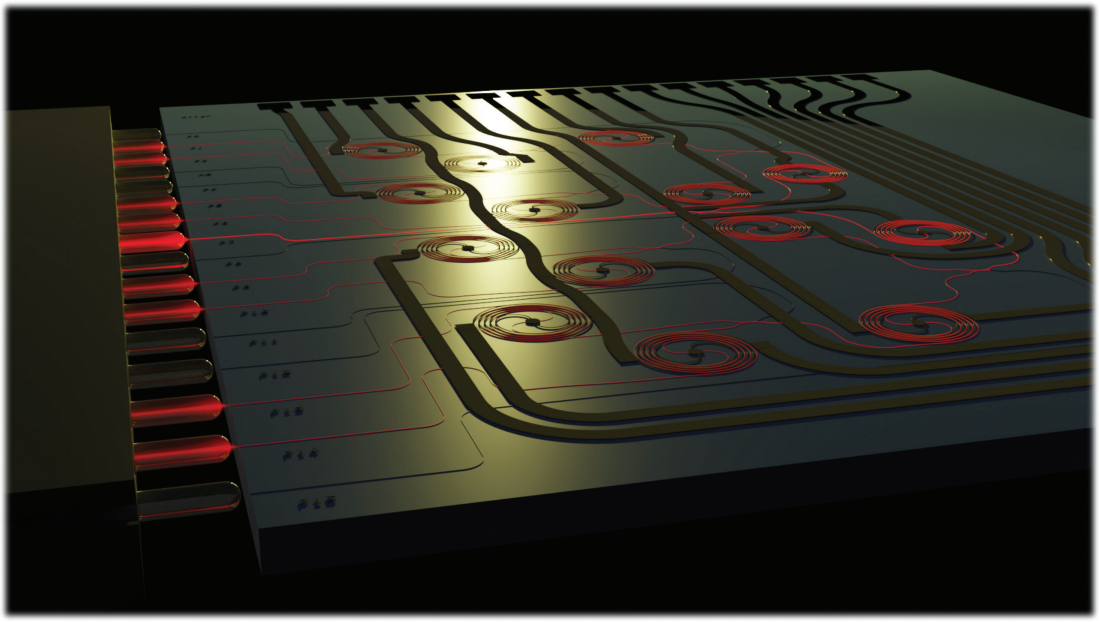

Figure 6.3: A coherent combining system of 8 channels on chip. Input and outputs interface a lensed fiber array for coupling. Phase-shifters are realized using voltage-driven resistor-based heaters fabricated on top of spiral sections of the waveguide.

It should be noted that fiber-coupling will remain important as optical fiber is necessary as an interfacing stage that bridges the gap between a larger telescope size, possibly with multiple apertures, and the cm size chip.

Polarization

The discussion throughout the thesis has in almost all cases omitted the polarization of light. Indeed, for practical realization of both coherent combining and phase sensitive amplification all waves involved need to be co-polarized. While exceptionally turbulent atmospheric links can depolarize the signal to small degrees, for links considered in this thesis, polarization remain as one of the most stable aspects in a free-space link [115–117]. The main cause of shift in polarization, or rather, orientation thereof is due to relative shift in orientation between transmitter and receiver. For polarization-insensitive reception and combining using fibers only the relative variation in polarization between channels must be compensated. This variation is deemed negligible in comparison to phase and can be performed using a slow polarization-tracking control in each stage. Although not as limiting as phase, such control should be implemented for practical links. In a single-polarization combiner (like Si_3N_4) as well as the PSA, absolute polarization control is necessary to align the incoming signal polarization to that of the waveguide and/or pump wave. Since this polarization drift is expected to be slow and to some extent predictable, it is yet something that will not limit overall performance but which is necessary to implement.

Upscaling and the demand on hardware

The error signal detection scheme investigated in [A,B] required an erbium doped fiber amplifier (EDFA), optical filter and photo-detector per combining stage, i.e. as many as the number of channels to combine (minus one). To reduce costs it would be interesting to investigate ways to circumvent the need for such a large volume of hardware without reducing the error signal SNR. Most importantly would be the EDFA in this context and for this purpose the recent development of spatially diverse amplifiers [118] could offer a new avenue of approach. When amplified, optical loss to certain degrees will not significantly degrade SNR and error signals could be incoherently combined to limit the number of necessary filters and detectors.

Sensitive error signal detection

Although optical preamplification provides sensitive operation, there may exist more appropriate error signal detection schemes in the context of coherent combining. The discussed use of single-photon detection and

amplitude modulation in chapter 1 and 2 were, in theory, superior to coherent detection for communications at very low received powers and low bandwidth. This is the exact scenario for error signal detection in coherent combining. Hence, to reach ultimate error signal sensitivity, the use of such detection should be investigated. Currently the work in [119] is pioneering this research.

Sophisticated locking

In this thesis we limited the discussion to OPLL performance during locking. Realistically, the system should also be able to bring itself into lock on up-start and in case locking is momentarily lost. For the 1st order dither-OPLL with recurring operating points $\phi = n2\pi$ (n is an integer) locking happens automatically. For phase and frequency compensating OPLLs and tip-tilt control this is not the case and would need to be implemented for a practical system.

On the other hand, these systems are not limited by the 2π-phase jumps discussed in chapter 3, as the tip-tilt does not compensate phase and frequency locking systems can compensate phase via proportional frequency control. For a coherent combining cascade with a large number of channels the momentary disruption of a phase jump in one stage may be negligible, depending on where in the cascade it happens. Further investigation on the impact and mitigation of 2π-phase jumps would be useful.

Atmospheric limitation

Were it not for the atmospheric turbulence there would not be a limit to how weak signal intensities can be efficiently received[B]. The use of laser guide stars (LGSs) could in principle lift this limitation by probing the turbulent free-space channel at high SNR. Future investigations on LGS for optical downlinks using the different large-area receivers discussed here would be of great value in the pursuit to effectively remove the atmospherically imposed minimum received power limitation. If lifted, the receiver size could in principle be made large enough to close any deep-space link regardless of distance and data rate. The remaining limitation would then concern cost and other practical limitations to how large telescopes or telescope arrays can be built.

CHAPTER 7

Summary of papers

This chapter lists the brief summary of each paper included in the thesis alongside a description of my contribution. As context, paper [A,B] concerns the investigation of increasing receiver area via means of multi-aperture or multi-mode reception and subsequent coherent optical combining of the signals thereof. Meanwhile, papers [C-E] addresses the phase-locking of phase sensitive amplifiers (PSAs) and the reduction of implementation complexity to make such preamplifiers viable in practical free-space links.

Paper A
Rasmus Larsson, Jochen Schröder, Magnus Karlsson, Peter A. Andrekson, "Coherent combining of low-power optical signals based on optically amplified error feedback", *Optics Express*, vol. 30, no. 11, pp. 19441-19455, May, 2022.

In this paper we investigate coherent optical combining in the context of a multi-aperture free-space receiver. The coherent combining control system is based on a sensitive dither-optical phase locked loop (OPLL) that uses optical pre-amplification of the error signal to maintain high

combining efficiency at low received powers. The performance of the combining system is characterized both with respect to the strength of relative phase fluctuations between channels as well as the received signal power, for two and four-channel combining. The scaling to more channels is also studied. Overall, we demonstrated that $> 97\%$ combining efficiency can be obtained when combining four 10 Gbaud quadrature phase-shift keying (QPSK)-modulated signals at ≥ -80 dBm received power per aperture.

My contribution: I designed and performed the simulations and experiments and conducted the overall analysis. I wrote the paper.

Paper B
Rasmus Larsson, Magnus Karlsson, Peter A. Andrekson, "Sensitive optical free-space receiver architecture for coherent combining of deep-space communication signals through atmospheric turbulence", *Manuscript submitted*

This paper investigates the overall receiver efficiency of large area multi-aperture and multi-mode receivers based on coherent combining for the reception of deep-space signals through the atmosphere. Monte-Carlo simulations of wave-propagation through realistic turbulence channels are used to generate the power spectral densities (PSDs) of phase-variations between channels to be coherently combined. The generated statistics are used together with phase locked loop (PLL)-theory to estimate the efficiency of the active phase-compensation and its impact on overall receiver efficiency for different received intensities and turbulence channels. Both receiver configurations are predicted to offer efficient combining of intensities down to -70 dBm/m^2 for realistic space-to-ground links when optimized and placed at adequate observatory sites a few km above sea-level. In terms of tip-tilt compensation, the multi-mode receiver appear superior to the multi-aperture receiver.

My contribution: I designed the study, performed the simulations and the experiment as well as the overall analysis. I wrote the paper.

Paper C
Rasmus Larsson, Kovendhan Vijayan, and Peter A. Andrekson, "Zero-Offset Frequency Locking of Lasers at Low Optical Powers With an Optical Phase Locked Loop", *Journal of Lightwave Technology*, vol. 42, no. 3, pp. 1183-1190, Feb, 2024.

This paper, which is an extension of the post-deadline paper in [H], investigates the performance of a zero-offset frequency-locking dither-OPLL at low reference wave powers. The system performance is thoroughly characterized with respect to phase noise in the temporal and spectral domains. For the sub-kHz linewidth lasers used we demonstrate locking down to powers of -90 dBm contained in the reference wave. The coherent amplification of the error signal using the strong slave laser light can enable the system over a broad range of wavelengths.

My contribution: I performed the simulations as well as the overall analysis. I also performed the experiments, with K. Vijayan assisting me in the RIN-measurement. I wrote the paper.

Paper D
Rasmus Larsson, Kovendhan Vijayan, Jochen Schröder, Peter A. Andrekson, "Low-noise phase-sensitive optical parametric amplifier with lossless local pump generation using a digital dither optical phase-locked loop", *Optics Express*, vol. 31, no. 22, pp. 36603-36614, Oct, 2023.

This paper demonstrates, for the first time, the novel local pump-locking scheme in which the PSA gain-maximization is used as feedback for a dither-OPLL controlling the pump frequency and phase. The demonstrated locking-scheme circumvents the need for pump reference waves or signal tapping for locking the PSA, significantly simplifying its implementation compared to previous demonstrations. With the use of this locking system, low-noise PSA amplification is shown with a noise figure (NF) below 3 dB at received powers down to -65 dBm using sub-kHz laser linewidths.

My contribution: I implemented the phase-locking system and performed the simulations. I also performed the experiment and the data processing with assistance from K. Vijayan. I wrote the paper.

Paper E

Rasmus Larsson, Ruwan U. Weerasuriya, Peter A. Andrekson, "Ultralow noise preamplified optical receiver using conventional single wavelength transmission", *Manuscript submitted*

This paper demonstrates, for the first time, low-noise ($<$ 3 dB NF) phase sensitive amplification based on the dual-pump, degenerate signal four-wave mixing (FWM)-configuration. The system employs the local pump-locking scheme from [D] and hence enables low-noise phase sensitievly pre-amplified coherent detection of single-wave signals. The low-noise performance of the demonstrated system is achieved down to -67 dBm received powers and would with the use of forward error correction (FEC) enable receiver sensitivities below 1 photons per information bit (PPIB).

My contribution: I and P. A. Andrekson conceptualized the idea. I performed the pre-study. I together with R. U. Weerasuriya built the experimental setup, optimized the pump and signal wavelength configuration as well as implemented the pump-phase modulation for suppression of stimulated Brillouin scattering. I performed the experiments with assistance from R. U. Weerasuriya as well as the data processing and analysis. I wrote the paper.

Bibliography

[1] S. di Serego Alighieri, "High resolution imaging." in *European Southern Observatory Conference and Workshop Proceedings*, ser. European Southern Observatory Conference and Workshop Proceedings, S. D'Odorico and J. P. Swings, Eds., vol. 24, Jan. 1986, pp. 173–178.

[2] C. Pilachowski, H. Dekker, K. Hinkle, R. Tull, S. Vogt, D. D. Walker, F. Diego, and R. Angel, "High-resolution spectrographs for large telescopes," *Publications of the Astronomical Society of the Pacific*, vol. 107, no. 716, p. 983, oct 1995. [Online]. Available: https://dx.doi.org/10.1086/133648

[3] G. Bonomi, P. Checchia, M. D'Errico, D. Pagano, and G. Saracino, "Applications of cosmic-ray muons," *Progress in Particle and Nuclear Physics*, vol. 112, p. 103768, 2020. [Online]. Available: https://www.sciencedirect.com/science/article/pii/S0146641020300156

[4] LIGO Scientific Collaboration, J. Aasi *et al.*, "Advanced LIGO," *Classical and Quantum Gravity*, vol. 32, no. 7, p. 074001, Apr. 2015.

[5] A. R. Vasavada, "Mission overview and scientific contributions from the mars science laboratory curiosity rover after eight years of surface operations," *Space Science Reviews*, vol. 218, no. 3, p. 14, Apr 2022. [Online]. Available: https://doi.org/10.1007/s11214-022-00882-7

[6] V. Z. Sun *et al.*, "Overview and results from the mars 2020 perseverance rover's first science campaign on the jezero crater floor," *Journal of Geophysical Research: Planets*, vol. 128, no. 6, p. e2022JE007613, 2023, e2022JE007613 2022JE007613. [Online]. Available: https://agupubs.onlinelibrary.wiley.com/doi/abs/10.1029/2022JE007613

[7] E. Stone, "The voyagers," *Nature Astronomy*, vol. 1, no. 12, pp. 896–896, Dec 2017. [Online]. Available: https://doi.org/10.1038/s41550-017-0339-2

[8] S. Shambayati, D. Morabito, J. Border, F. Davarian, D. Lee, R. Mendoza, M. Britcliffe, and S. Weinreb, *Mars Reconnaissance Orbiter Ka-Band (32 GHz) Demonstration: Cruise Phase Operations*. American Institute of Aeronautics and Astronautics, 2006. [Online]. Available: https://arc.aiaa.org/doi/abs/10.2514/6.2006-5786

[9] A. Witze, "Lift off! artemis moon rocket launch kicks off new era of human exploration," *Nature*, vol. 611, no. 7937, pp. 643–644, Nov 2022.

[10] W. A. Imbriale, *Introduction*. John Wiley & Sons, Ltd, 2003, pp. 1–69. [Online]. Available: https://onlinelibrary.wiley.com/doi/abs/10.1002/0471728497.ch1

[11] D. E. Koelle, "Specific Space Transportation Costs to GEO - Past, Present and Future," in *IAF abstracts, 34th COSPAR Scientific Assembly*, Jan. 2002, p. 253.

[12] K. Singh and A. Nirmal, "Overview of modulation schemes selection in satellite based communication," *ICTACT Journal of Communication Technology*, vol. 11, no. 3, pp. 2203–2207, Sep 2020.

[13] P. T. Thompson, *Satellite Communications Modulation and Multiplexing*. New York, NY: Springer New York, 2016, pp. 1–34. [Online]. Available: https://doi.org/10.1007/978-1-4614-6423-5_86-3

[14] M. Toyoshima, W. R. Leeb, H. Kunimori, and T. Takano, "Comparison of microwave and light wave communication systems in space applications," *Optical Engineering*, vol. 46, no. 1,

p. 015003, 2007. [Online]. Available: https://doi.org/10.1117/1.2432881

[15] K. E. Wilson, J. R. Lesh, K. Araki, and Y. Arimoto, "Overview of the Ground-to-Orbit Lasercom Demonstration (GOLD)," in *Free-Space Laser Communication Technologies IX*, G. S. Mecherle, Ed., vol. 2990, International Society for Optics and Photonics. SPIE, 1997, pp. 23 – 30. [Online]. Available: https://doi.org/10.1117/12.273703

[16] T. Tolker-Nielsen and G. Oppenhauser, "In-orbit test result of an operational optical intersatellite link between ARTEMIS and SPOT4, SILEX," in *Free-Space Laser Communication Technologies XIV*, G. S. Mecherle, Ed., vol. 4635, International Society for Optics and Photonics. SPIE, 2002, pp. 1 – 15. [Online]. Available: https://doi.org/10.1117/12.464105

[17] D. M. Boroson, B. S. Robinson, D. V. Murphy, D. A. Burianek, F. Khatri, J. M. Kovalik, Z. Sodnik, and D. M. Cornwell, "Overview and results of the Lunar Laser Communication Demonstration," in *Free-Space Laser Communication and Atmospheric Propagation XXVI*, H. Hemmati and D. M. Boroson, Eds., vol. 8971, International Society for Optics and Photonics. SPIE, 2014, p. 89710S. [Online]. Available: https://doi.org/10.1117/12.2045508

[18] I. J. O'Neill, "Nasa's tech demo streams first video from deep space via laser," 2023, https://www.jpl.nasa.gov/news/nasas-tech-demo-streams-first-video-from-deep-space-via-laser [Accessed: (2024-07-21)].

[19] D. J. Israel, B. L. Edwards, R. L. Butler, J. D. Moores, S. Piazzolla, N. du Toit, and L. Braatz, "Early results from NASA's laser communications relay demonstration (LCRD) experiment program," in *Free-Space Laser Communications XXXV*, H. Hemmati and B. S. Robinson, Eds., vol. 12413, International Society for Optics and Photonics. SPIE, 2023, p. 1241303. [Online]. Available: https://doi.org/10.1117/12.2655481

[20] A. Seas, B. Robinson, T. Shih, F. Khatri, and M. Brumfield, "Optical communications systems for NASA's human space flight missions," in *International Conference on Space Optics —*

ICSO 2018, ser. Society of Photo-Optical Instrumentation Engineers (SPIE) Conference Series, Z. Sodnik, N. Karafolas, and B. Cugny, Eds., vol. 11180, Jul. 2019, p. 111800H.

[21] A. Carrasco-Casado and R. Mata-Calvo, *Space Optical Links for Communication Networks.* Cham: Springer International Publishing, 2020, pp. 1057–1103. [Online]. Available: https://doi.org/10.1007/978-3-030-16250-4_34

[22] M. E. Grein, A. J. Kerman, E. A. Dauler, M. M. Willis, B. Romkey, R. J. Molnar, B. S. Robinson, D. V. Murphy, and D. M. Boroson, "An optical receiver for the Lunar Laser Communication Demonstration based on photon-counting superconducting nanowires," in *Advanced Photon Counting Techniques IX*, M. A. Itzler and J. C. Campbell, Eds., vol. 9492, International Society for Optics and Photonics. SPIE, 2015, p. 949208. [Online]. Available: https://doi.org/10.1117/12.2179781

[23] P. I. Hopman, P. W. Boettcher, L. M. Candell, J. B. Glettler, R. Shoup, and G. Zogbi, "An end-to-end demonstration of a receiver array based free-space photon counting communications link," in *Free-Space Laser Communications VI*, A. K. Majumdar and C. C. Davis, Eds., vol. 6304, International Society for Optics and Photonics. SPIE, 2006, p. 63040H. [Online]. Available: https://doi.org/10.1117/12.682845

[24] K. Kikuchi, "Fundamentals of coherent optical fiber communications," *J. Lightwave Technol.*, vol. 34, no. 1, pp. 157–179, Jan 2016. [Online]. Available: https://opg.optica.org/jlt/abstract.cfm?URI=jlt-34-1-157

[25] R. J. Mears, L. Reekie, I. M. Jauncey, and D. N. Payne, "Low-noise erbium-doped fibre amplifier operating at 1.54μm," *Electronics Letters*, vol. 23, no. 19, p. 1026, Jan. 1987.

[26] P. A. Andrekson and M. Karlsson, "Fiber-based phase-sensitive optical amplifiers and their applications," *Adv. Opt. Photon.*, vol. 12, no. 2, pp. 367–428, Jun 2020. [Online]. Available: https://opg.optica.org/aop/abstract.cfm?URI=aop-12-2-367

[27] C. M. Caves, "Quantum limits on noise in linear amplifiers," *Phys. Rev. D*, vol. 26, pp. 1817–1839, Oct 1982. [Online]. Available: https://link.aps.org/doi/10.1103/PhysRevD.26.1817

[28] Z. Tong, C. Lundström, P. A. Andrekson, C. J. McKinstrie, M. Karlsson, D. J. Blessing, E. Tipsuwannakul, B. J. Puttnam, H. Toda, and L. Grüner-Nielsen, "Towards ultrasensitive optical links enabled by low-noise phase-sensitive amplifiers," *Nature Photonics*, vol. 5, no. 7, pp. 430–436, Jul 2011. [Online]. Available: https://doi.org/10.1038/nphoton.2011.79

[29] T. Kazama, T. Umeki, S. Shimizu, T. Kashiwazaki, K. Enbutsu, R. Kasahara, Y. Miyamoto, and K. Watanabe, "Over-30-db gain and 1-db noise figure phase-sensitive amplification using a pump-combiner-integrated fiber i/o ppln module," *Opt. Express*, vol. 29, no. 18, pp. 28 824–28 834, Aug 2021. [Online]. Available: https://opg.optica.org/oe/abstract.cfm?URI=oe-29-18-28824

[30] K. Vijayan, A. Mirani, J. Schröder, M. Karlsson, and P. Andrekson, "Capacity of phase-sensitively preamplified optical links at low signal-to-noise ratio," in *European Conference on Optical Communication (ECOC) 2022*. Optica Publishing Group, 2022, p. We4D.2. [Online]. Available: https://opg.optica.org/abstract.cfm?URI=ECEOC-2022-We4D.2

[31] S. L. I. Olsson, B. Corcoran, C. Lundström, T. A. Eriksson, M. Karlsson, and P. A. Andrekson, "Phase-sensitive amplified transmission links for improved sensitivity and nonlinearity tolerance," *Journal of Lightwave Technology*, vol. 33, no. 3, pp. 710–721, 2015.

[32] K. Vijayan, B. Foo, M. Karlsson, and P. A. Andrekson, "Cross-phase modulation mitigation in phase-sensitive amplifier links," *IEEE Photonics Technology Letters*, vol. 31, no. 21, pp. 1733–1736, 2019.

[33] R. Slavík, F. Parmigiani, J. Kakande, C. Lundström, M. Sjödin, P. A. Andrekson, R. Weerasuriya, S. Sygletos, A. D. Ellis, L. Grüner-Nielsen, D. Jakobsen, S. Herstrøm, R. Phelan, J. O'Gorman, A. Bogris, D. Syvridis, S. Dasgupta, P. Petropoulos, and D. J. Richardson, "All-optical phase and amplitude regenerator for next-generation telecommunications systems," *Nature Photonics*, vol. 4, no. 10, pp. 690–695, Oct 2010. [Online]. Available: https://doi.org/10.1038/nphoton.2010.203

[34] R. Kakarla, J. Schröder, and P. A. Andrekson, "One photon-per-bit receiver using near-noiseless phase-sensitive amplification," *Light: Science & Applications*, vol. 9, no. 1, p. 153, Sep 2020. [Online]. Available: https://doi.org/10.1038/s41377-020-00389-2

[35] R. Romanofsky, *Optical Array Versus Monolithic Telescope Ground Station Cost Assessment*, ser. NASA technical memorandum. National Aeronautics and Space Administration, Glenn Research Center, 2019. [Online]. Available: https://books.google.se/books?id=reu1zgEACAAJ

[36] S. L. I. Olsson, B. Corcoran, C. Lundström, E. Tipsuwannakul, S. Sygletos, A. D. Ellis, Z. Tong, M. Karlsson, and P. A. Andrekson, "Injection locking-based pump recovery for phase-sensitive amplified links," *Opt. Express*, vol. 21, no. 12, pp. 14 512–14 529, Jun 2013. [Online]. Available: https://opg.optica.org/oe/abstract.cfm?URI=oe-21-12-14512

[37] R. Kakarla, J. Schröder, and P. A. Andrekson, "Optical injection locking at sub nano-watt powers," *Opt. Lett.*, vol. 43, no. 23, pp. 5769–5772, Dec 2018. [Online]. Available: https://opg.optica.org/ol/abstract.cfm?URI=ol-43-23-5769

[38] Y. Okamura, M. Abe, K. Kondo, Y. Ohmichi, T. Kazama, T. Umeki, M. Koga, and A. Takada, "Optical pump phase locking to a carrier wave extracted from phase-conjugated twin waves for phase-sensitive optical amplifier repeaters," *Opt. Express*, vol. 24, no. 23, pp. 26 300–26 306, Nov 2016. [Online]. Available: https://opg.optica.org/oe/abstract.cfm?URI=oe-24-23-26300

[39] T. Kazama, T. Umeki, Y. Okamura, K. Enbutsu, O. Tadanaga, A. Takada, and R. Kasahara, "Ppln-based low-noise phase sensitive amplification using an optical phase-locked pump," *IEICE Transactions on Communications*, vol. E103.B, no. 11, pp. 1265–1271, 2020.

[40] R. Kakarla, M. Mazur, J. Schröder, and P. A. Andrekson, "Power efficient communication for low signal to noise ratio optical links," 2021.

[41] ——, "Power efficient communications employing phase sensitive pre-amplified receiver," *IEEE Photonics Technology Letters*, vol. 34, no. 1, pp. 3–6, 2022.

[42] L. Kulmer, Y. Horst, B. I. Bitachon, M. Destraz, T. Blatter, M. Rimlinger, A. Montmerle-Bonnefois, J. Montri, C. B. Lim, J.-M. Conan, B. Sorrente, N. Védrenne, L. Pommarel, D. Matter, B. Baeuerle, and J. Leuthold, "Highest-speed modulators enabling high-capacity free space optical communications at low snr," *Journal of Lightwave Technology*, vol. 42, no. 10, pp. 3770–3778, 2024.

[43] D. Hogg, "Fun with the friis free-space transmission formula," *IEEE Antennas and Propagation Magazine*, vol. 35, no. 4, pp. 33–35, Aug 1993.

[44] J. S. Luskin, E. Schmidt, B. Korzh, A. D. Beyer, B. Bumble, J. P. Allmaras, A. B. Walter, E. E. Wollman, L. NarvÃ¡ez, V. B. Verma, S. W. Nam, I. Charaev, M. Colangelo, K. K. Berggren, C. Peña, M. Spiropulu, M. Garcia-Sciveres, S. Derenzo, and M. D. Shaw, "Large active-area superconducting microwire detector array with single-photon sensitivity in the near-infrared," *Applied Physics Letters*, vol. 122, no. 24, p. 243506, 06 2023. [Online]. Available: https://doi.org/10.1063/5.0150282

[45] R. J. Sasiela, *Zero-Parameter Problems*. SPIE, September 2009, pp. 95–116. [Online]. Available: https://lens.org/196-479-015-169-518

[46] D. P. Greenwood and D. L. Fried, "Power spectra requirements for wave-front-compensative systems∗," *J. Opt. Soc. Am.*, vol. 66, no. 3, pp. 193–206, Mar 1976. [Online]. Available: https://opg.optica.org/abstract.cfm?URI=josa-66-3-193

[47] D. P. Greenwood, "Bandwidth specification for adaptive optics systems∗," *J. Opt. Soc. Am.*, vol. 67, no. 3, pp. 390–393, Mar 1977. [Online]. Available: https://opg.optica.org/abstract.cfm?URI=josa-67-3-390

[48] L. C. Andrews and R. L. Phillips, *Laser Satellite Communication Systems*. SPIE, 2005, pp. 477–531, https://www.spiedigitallibrary.org/ebooks/PM/Laser-Beam-Propagation-through-Random-Media-Second-Edition/12/Laser-Satellite-Communication-Systems/10.1117/3.626196.ch12. [Online]. Available: https://lens.org/066-367-569-948-329

[49] H. T. Yura and W. G. McKinley, "Aperture averaging of scintillation for space-to-ground optical communication applications," *Appl. Opt.*, vol. 22, no. 11, pp. 1608–1609, Jun 1983. [Online]. Available: https://opg.optica.org/ao/abstract.cfm?URI=ao-22-11-1608

[50] J. P. Gordon, "Quantum effects in communications systems," *Proceedings of the IRE*, vol. 50, no. 9, pp. 1898–1908, 1962.

[51] K. Balakier, L. Ponnampalam, M. J. Fice, C. C. Renaud, and A. J. Seeds, "Integrated semiconductor laser optical phase lock loops," *IEEE Journal of Selected Topics in Quantum Electronics*, vol. 24, no. 1, pp. 1–12, 2018.

[52] F. Herzog, K. Kudielka, D. Erni, and W. Bachtold, "Optical phase locking by local oscillator phase dithering," *IEEE Journal of Quantum Electronics*, vol. 42, no. 10, pp. 973–985, 2006.

[53] M. Zanuso, D. Tasca, S. Levantino, A. Donadel, C. Samori, and A. L. Lacaita, "Noise analysis and minimization in bang-bang digital plls," *IEEE Transactions on Circuits and Systems II: Express Briefs*, vol. 56, no. 11, pp. 835–839, 2009.

[54] J. Spilker, *Digital Communications by Satellite*. Prentice-Hall, Englewood Cliffs, New Jersey, 1977, ch. 12. [Online]. Available: https://books.google.se/books?id=RkwvEAAAQBAJ

[55] L. Palmer and S. Klein, "Phase slipping in phase-locked loop configurations that track biphase or quadriphase modulated carriers," *IEEE Transactions on Communications*, vol. 20, no. 5, pp. 984–991, 1972.

[56] C. Madsen, "Boundless-range optical phase modulator for high-speed frequency-shift and heterodyne applications," *Journal of Lightwave Technology*, vol. 24, no. 7, pp. 2760–2767, 2006.

[57] C. Rao, L. Zhong, Y. Guo, M. Li, L. Zhang, and K. Wei, "Astronomical adaptive optics: a review," *PhotoniX*, vol. 5, no. 1, p. 16, May 2024. [Online]. Available: https://doi.org/10.1186/s43074-024-00118-7

[58] A. Yevick, R. Bayne, R. Garcia, V. S. Grigoryan, R. Lafon, S. A. Tedder, J. Veselka, and B. Vyhnalek, "Experimental

demonstration of coherent receiver with photonic lantern and digital signal processing," in *Free-Space Laser Communications XXXVI*, H. Hemmati and B. S. Robinson, Eds., vol. 12877, International Society for Optics and Photonics. SPIE, 2024, p. 1287711. [Online]. Available: https://doi.org/10.1117/12.3003080

[59] Y. Yang, C. Geng, F. Li, G. Huang, and X. Li, "Multi-aperture all-fiber active coherent beam combining for free-space optical communication receivers," *Opt. Express*, vol. 25, no. 22, pp. 27 519–27 532, Oct 2017. [Online]. Available: https://opg.optica.org/oe/abstract.cfm?URI=oe-25-22-27519

[60] T. J. Karr, "Temporal response of atmospheric turbulence compensation," *Applied Optics; (USA)*, vol. 30:4, 2 1991. [Online]. Available: https://www.osti.gov/biblio/5858801

[61] M. Chen, C. Liu, and H. Xian, "Experimental demonstration of single-mode fiber coupling over relatively strong turbulence with adaptive optics," *Appl. Opt.*, vol. 54, no. 29, pp. 8722–8726, Oct 2015. [Online]. Available: https://opg.optica.org/ao/abstract.cfm?URI=ao-54-29-8722

[62] Y. Wang, H. Xu, D. Li, R. Wang, C. Jin, X. Yin, S. Gao, Q. Mu, L. Xuan, and Z. Cao, "Performance analysis of an adaptive optics system for free-space optics communication through atmospheric turbulence," *Scientific Reports*, vol. 8, no. 1, p. 1124, Jan 2018. [Online]. Available: https://doi.org/10.1038/s41598-018-19559-9

[63] M. W. Wright, J. F. Morris, J. M. Kovalik, K. S. Andrews, M. J. Abrahamson, and A. Biswas, "Adaptive optics correction into single mode fiber for a low earth orbiting space to ground optical communication link using the opals downlink," *Opt. Express*, vol. 23, no. 26, pp. 33 705–33 712, Dec 2015. [Online]. Available: https://opg.optica.org/oe/abstract.cfm?URI=oe-23-26-33705

[64] C. Paterson, "Towards practical wavefront sensing at the fundamental information limit," *Journal of Physics: Conference Series*, vol. 139, no. 1, p. 012021, nov 2008. [Online]. Available: https://dx.doi.org/10.1088/1742-6596/139/1/012021

[65] S. Haffert, J. Males, and O. Guyon, "Reaching the fundamental sensitivity limit of wavefront sensing on arbitrary apertures with

the Phase Induced Amplitude Apodized Zernike Wavefront Sensor (PIAA-ZWFS)," in *Adaptive Optics for Extremely Large Telescopes (AO4ELT7)*, Jun. 2023, p. 79.

[66] P. Feautrier, J.-L. Gach, M. Downing, P. Jorden, J. Kolb, J. Rothman, T. Fusco, P. Balard, E. Stadler, C. Guillaume, D. Boutolleau, G. Destefanis, N. Lhermet, O. Pacaud, M. Vuillermet, A. Kerlain, N. Hubin, J. Reyes, M. Kasper, O. Ivert, W. Suske, A. Walker, M. Skegg, S. Derelle, J. Deschamps, C. Robert, N. Vedrenne, F. Chazalet, J. Tanchon, T. Trollier, A. Ravex, G. Zins, P. Kern, T. Moulin, and O. Preis, "Advances in detector technologies for visible and infrared wavefront sensing," in *Adaptive Optics Systems III*, B. L. Ellerbroek, E. Marchetti, and J.-P. Véran, Eds., vol. 8447, International Society for Optics and Photonics. SPIE, 2012, p. 84470Q. [Online]. Available: https://doi.org/10.1117/12.925067

[67] C. d'Orgeville and G. J. Fetzer, "Four generations of sodium guide star lasers for adaptive optics in astronomy and space situational awareness," in *Adaptive Optics Systems V*, E. Marchetti, L. M. Close, and J.-P. Véran, Eds., vol. 9909, International Society for Optics and Photonics. SPIE, 2016, p. 99090R. [Online]. Available: https://doi.org/10.1117/12.2234298

[68] R. Mata-Calvo, D. B. Calia, R. Barrios, M. Centrone, D. Giggenbach, G. Lombardi, P. Becker, and I. Zayer, "Laser guide stars for optical free-space communications," in *Free-Space Laser Communication and Atmospheric Propagation XXIX*, H. Hemmati and D. M. Boroson, Eds., vol. 10096, International Society for Optics and Photonics. SPIE, 2017, p. 100960R. [Online]. Available: https://doi.org/10.1117/12.2256666

[69] A. P. Reeves, N. Ageorges, D. Kampf, D. G. Ramos, M. Abdo, I. Hristovski, H. F. Kelemu, D. J. Laidlaw, Z. Sodnik, R. M. Calvo, and B. Femenía-Castellá, "GEOStar: demonstration of laser guide star adaptive optics for free space optical communications," in *Free-Space Laser Communications XXXVI*, H. Hemmati and B. S. Robinson, Eds., vol. 12877, International Society for Optics and Photonics. SPIE, 2024, p. 128771S. [Online]. Available: https://doi.org/10.1117/12.3002594

[70] M. Diab, A. N. Dinkelaker, J. Davenport, K. Madhav, and M. M. Roth, "Starlight coupling through atmospheric turbulence into few-mode fibres and photonic lanterns in the presence of partial adaptive optics correction," *Monthly Notices of the Royal Astronomical Society*, vol. 501, no. 2, pp. 1557–1567, 12 2020. [Online]. Available: https://doi.org/10.1093/mnras/staa3752

[71] T. A. Birks, I. Gris-Sánchez, S. Yerolatsitis, S. G. Leon-Saval, and R. R. Thomson, "The photonic lantern," *Adv. Opt. Photon.*, vol. 7, no. 2, pp. 107–167, Jun 2015. [Online]. Available: https://opg.optica.org/aop/abstract.cfm?URI=aop-7-2-107

[72] W. Guo, Y. Li, J. Chen, T. Jin, S. Jiao, J. Wu, J. Qiu, and H. Guo, "Satellite-to-ground optical downlink model using mode mismatching multi-mode photonic lanterns," *Opt. Express*, vol. 31, no. 21, pp. 35 041–35 053, Oct 2023. [Online]. Available: https://opg.optica.org/oe/abstract.cfm?URI=oe-31-21-35041

[73] S. G. Leon-Saval, N. K. Fontaine, J. R. Salazar-Gil, B. Ercan, R. Ryf, and J. Bland-Hawthorn, "Mode-selective photonic lanterns for space-division multiplexing," *Opt. Express*, vol. 22, no. 1, pp. 1036–1044, Jan 2014. [Online]. Available: https://opg.optica.org/oe/abstract.cfm?URI=oe-22-1-1036

[74] S. Arisa, Y. Takayama, H. Endo, R. Shimizu, M. Fujiwara, and M. Sasaki, "Coupling efficiency of laser beam to multimode fiber for free space optical communication," in *International Conference on Space Optics - ICSO 2014*, Z. Sodnik, B. Cugny, and N. Karafolas, Eds., vol. 10563, International Society for Optics and Photonics. SPIE, 2017, p. 105630Y. [Online]. Available: https://doi.org/10.1117/12.2304222

[75] M. Arikawa, Y. Ono, and T. Ito, "Mode diversity coherent receiver with few-mode fiber-coupling for high-speed free-space optical communication under atmospheric turbulence," in *Free-Space Laser Communication and Atmospheric Propagation XXX*, H. Hemmati and D. M. Boroson, Eds., vol. 10524, International Society for Optics and Photonics. SPIE, 2018, p. 1052412. [Online]. Available: https://doi.org/10.1117/12.2288193

[76] G. A. Tyler, "Bandwidth considerations for tracking through turbulence," *J. Opt. Soc. Am. A*, vol. 11, no. 1, pp. 358–367, Jan

1994. [Online]. Available: https://opg.optica.org/josaa/abstract.cfm?URI=josaa-11-1-358

[77] H. P. Stahl, "Survey of cost models for space telescopes," *Optical Engineering*, vol. 49, no. 5, p. 053005, 2010. [Online]. Available: https://doi.org/10.1117/1.3430603

[78] L. Liu, M. A. Vorontsov, E. Polnau, T. Weyrauch, and L. A. Beresnev, "Adaptive phase-locked fiber array with wavefront phase tip-tilt compensation using piezoelectric fiber positioners," in *Atmospheric Optics: Models, Measurements, and Target-in-the-Loop Propagation*, S. M. Hammel, A. M. J. van Eijk, M. T. Valley, and M. A. Vorontsov, Eds., vol. 6708, International Society for Optics and Photonics. SPIE, 2007, p. 67080K. [Online]. Available: https://doi.org/10.1117/12.736366

[79] K. Jin, H. Chang, R. Su, J. Long, S. Chen, J. Zhang, Y. Ma, and P. Zhou, "Coherent beam combining of 7 fiber amplifiers based on all-fiber internal phase-locking technique," *Optics & Laser Technology*, vol. 171, p. 110456, 2024. [Online]. Available: https://www.sciencedirect.com/science/article/pii/S003039922301349X

[80] H. Chang, R. Su, J. Long, Q. Chang, P. Ma, Y. Ma, and P. Zhou, "Distributed active phase-locking of an all-fiber structured laser array by a stochastic parallel gradient descent (spgd) algorithm," *Opt. Express*, vol. 30, no. 2, pp. 1089–1098, Jan 2022. [Online]. Available: https://opg.optica.org/oe/abstract.cfm?URI=oe-30-2-1089

[81] C. Lao, J. Sun, Z. Lu, J. Li, M. Xu, H. He, R. Han, X. Cai, and Y. Li, "Multi-aperture fiber coherent combining system in urban horizontal atmospheric laser link," *Optics Communications*, vol. 466, p. 125172, 2020. [Online]. Available: https://www.sciencedirect.com/science/article/pii/S0030401819311563

[82] F. Zou, Z. Pan, J. Liu, Z. Li, L. Pan, R. Yang, J. Jiang, F. Li, C. Geng, and X. Li, "Bidirectional coherent beam combining and turbulence mitigating by phased fiber laser array in a 2 km atmospheric link," *Optics & Laser Technology*, vol. 163, p. 109311, 2023. [Online]. Available: https://www.sciencedirect.com/science/article/pii/S0030399223002049

[83] D. J. Geisler, T. M. Yarnall, M. L. Stevens, C. M. Schieler, B. S. Robinson, and S. A. Hamilton, "Multi-aperture digital coherent combining for free-space optical communication receivers," *Opt. Express*, vol. 24, no. 12, pp. 12 661–12 671, Jun 2016. [Online]. Available: https://opg.optica.org/oe/abstract.cfm?URI=oe-24-12-12661

[84] D. J. Geisler, T. M. Yarnall, C. M. Schieler, M. L. Stevens, B. S. Robinson, and S. A. Hamilton, "Optical ground terminals using multi-aperture digital coherent combining (invited paper)," in *2017 IEEE Photonics Conference (IPC)*, 2017, pp. 715–716.

[85] C. Ju, N. Liu, D. Wang, D. Wang, J. Yu, and Y. Qiu, "Real-time demonstration of two-aperture coherent digital combining free-space optical transmission with a real-valued mimo adaptive equalizer," *Opt. Lett.*, vol. 49, no. 4, pp. 903–906, Feb 2024. [Online]. Available: https://opg.optica.org/ol/abstract.cfm?URI=ol-49-4-903

[86] K. Xu, J. Song, Y. Li, J. Chen, J. Qiu, X. Hong, H. Guo, Z. Yang, and J. Wu, "Real-time low-complexity diversity combining algorithm for free space coherent optical communication systems over atmospheric turbulence channel," *Opt. Express*, vol. 31, no. 24, pp. 40 705–40 716, Nov 2023. [Online]. Available: https://opg.optica.org/oe/abstract.cfm?URI=oe-31-24-40705

[87] C. Rao, S. Cui, Y. Tu, K. Zhou, and D. Liu, "Toward practical digital phase alignment for coherent beam combining in multi-aperture free space coherent optical receivers," *IEEE Access*, vol. 8, pp. 202 585–202 595, 2020.

[88] Y. Tu, S. Cui, K. Zhou, and D. Liu, "Phase alignment with minimum complexity for equal gain combining in multi-aperture free-space digital coherent optical communication receivers," *IEEE Photonics Journal*, vol. 12, no. 2, pp. 1–10, 2020.

[89] J. Sun, P. Huang, Z. Yao, and J. Guo, "Adaptive digital combining for coherent free space optical communications with spatial diversity reception," *Optics Communications*, vol. 444, pp. 32–38, 2019. [Online]. Available: https://www.sciencedirect.com/science/article/pii/S0030401819302810

[90] Y. Bian, Y. Li, D. Zheng, T. Dong, E. Chen, W. Li, X. Hong, J. Qiu, Y. Jie, Y. Su, and J. Wu, "Performance investigation of satellite-to-ground downlink optical communications employing aperture diversity combined with mode diversity," *Optics Communications*, vol. 491, p. 126958, 2021. [Online]. Available: https://www.sciencedirect.com/science/article/pii/S003040182100208X

[91] C. Ju, N. Liu, L. Guan, D. Wang, and D. Wang, "Blind skew compensation and digital combining with widely linear equalizer for multi-aperture coherent fso communication," *Opt. Express*, vol. 31, no. 18, pp. 29 912–29 924, Aug 2023. [Online]. Available: https://opg.optica.org/oe/abstract.cfm?URI=oe-31-18-29912

[92] D. A. B. Miller, "Establishing optimal wave communication channels automatically," *Journal of Lightwave Technology*, vol. 31, no. 24, pp. 3987–3994, 2013.

[93] S. SeyedinNavadeh, M. Milanizadeh, G. Benci, C. De Vita, C. Klitis, M. Sorel, F. Zanetto, V. Grimaldi, G. Ferrari, D. A. Miller, A. Melloni, and F. Morichetti, "Self-configuring silicon-photonic receiver for multimode free space channels," in *2021 IEEE 17th International Conference on Group IV Photonics (GFP)*, 2021, pp. 1–2.

[94] V. Billault, J. Bourderionnet, J. P. Mazellier, L. Leviandier, P. Feneyrou, A. Maho, M. Sotom, X. Normandin, H. Lonjaret, and A. Brignon, "Free space optical communication receiver based on a spatial demultiplexer and a photonic integrated coherent combining circuit," *Opt. Express*, vol. 29, no. 21, pp. 33 134–33 143, Oct 2021. [Online]. Available: https://opg.optica.org/oe/abstract.cfm?URI=oe-29-21-33134

[95] W. Bogaerts, D. Pérez, J. Capmany, D. A. B. Miller, J. Poon, D. Englund, F. Morichetti, and A. Melloni, "Programmable photonic circuits," *Nature*, vol. 586, no. 7828, pp. 207–216, Oct 2020. [Online]. Available: https://doi.org/10.1038/s41586-020-2764-0

[96] F. Morichetti, G. Cavicchioli, A. Martinez, S. Seyedinnavadeh, F. Zanetto, C. Mazzucco, M. Re, M. Mattivi, F. Morandi, A. D'Acierno, U. Spagnolini, and A. Melloni, "Mitigation of atmospheric turbulence in an optical free space link with an

integrated photonic processor," in *Optical Fiber Communication Conference (OFC) 2023*. Optica Publishing Group, 2023, p. W3I.7. [Online]. Available: https://opg.optica.org/abstract.cfm?URI=OFC-2023-W3I.7

[97] J. M. Dziedzic, R. H. Stolen, and A. Ashkin, "Optical kerr effect in long fibers," *Appl. Opt.*, vol. 20, no. 8, pp. 1403–1406, Apr 1981. [Online]. Available: https://opg.optica.org/ao/abstract.cfm?URI=ao-20-8-1403

[98] M. Fejer, G. Magel, D. Jundt, and R. Byer, "Quasi-phase-matched second harmonic generation: tuning and tolerances," *IEEE Journal of Quantum Electronics*, vol. 28, no. 11, pp. 2631–2654, 1992.

[99] Z. Tong, C. Lundström, P. A. Andrekson, M. Karlsson, and A. Bogris, "Ultralow noise, broadband phase-sensitive optical amplifiers, and their applications," *IEEE Journal of Selected Topics in Quantum Electronics*, vol. 18, no. 2, pp. 1016–1032, 2012.

[100] K. J. Lee, F. Parmigiani, S. Liu, J. Kakande, P. Petropoulos, K. Gallo, and D. Richardson, "Phase sensitive amplification based on quadratic cascading in a periodically poled lithium niobate waveguide," *Opt. Express*, vol. 17, no. 22, pp. 20 393–20 400, Oct 2009. [Online]. Available: https://opg.optica.org/oe/abstract.cfm?URI=oe-17-22-20393

[101] G. C. Bhar and U. Chatterjee, "Analyses of phase-matching for noncollinear three-wave mixing in uniaxial crystals," *Japanese Journal of Applied Physics*, vol. 29, no. 6R, p. 1103, jun 1990. [Online]. Available: https://dx.doi.org/10.1143/JJAP.29.1103

[102] S. Shimizu, T. Kazama, T. Kobayashi, T. Umeki, K. Enbutsu, R. Kasahara, and Y. Miyamoto, "Non-degenerate phase-sensitive amplification scheme using digital dispersion pre-equalization for unrepeated transmission," *Opt. Express*, vol. 29, no. 6, pp. 8451–8461, Mar 2021. [Online]. Available: https://opg.optica.org/oe/abstract.cfm?URI=oe-29-6-8451

[103] T. Umeki, O. Tadanaga, A. Takada, and M. Asobe, "Phase sensitive degenerate parametric amplification using directly-bonded ppln ridge waveguides," *Opt. Express*, vol. 19, no. 7, pp. 6326–6332, Mar 2011. [Online]. Available: https://opg.optica.org/oe/abstract.cfm?URI=oe-19-7-6326

[104] T. Umeki, M. Asobe, and H. Takenouchi, "In-line phase sensitive amplifier based on ppln waveguides," *Opt. Express*, vol. 21, no. 10, pp. 12 077–12 084, May 2013. [Online]. Available: https://opg.optica.org/oe/abstract.cfm?URI=oe-21-10-12077

[105] R. Tang, J. Lasri, P. S. Devgan, V. Grigoryan, P. Kumar, and M. Vasilyev, "Gain characteristics of a frequency nondegenerate phase-sensitive fiber-optic parametric amplifier with phase self-stabilized input," *Opt. Express*, vol. 13, no. 26, pp. 10 483–10 493, Dec 2005. [Online]. Available: https://opg.optica.org/oe/abstract.cfm?URI=oe-13-26-10483

[106] Z. Ye, P. Zhao, K. Twayana, M. Karlsson, V. Torres-Company, and P. A. Andrekson, "Overcoming the quantum limit of optical amplification in monolithic waveguides," *Science Advances*, vol. 7, no. 38, p. eabi8150, 2021. [Online]. Available: https://www.science.org/doi/abs/10.1126/sciadv.abi8150

[107] J. Aasi *et al.*, "Enhanced sensitivity of the ligo gravitational wave detector by using squeezed states of light," *Nature Photonics*, vol. 7, no. 8, pp. 613–619, Aug 2013. [Online]. Available: https://doi.org/10.1038/nphoton.2013.177

[108] Y. Bouasria, D. Chatterjee, W. Xie, I. Fsaifes, F. Goldfarb, Y. Hassouni, and F. Bretenaker, "Investigation of the noise figure in a degenerate dual-pump phase-sensitive amplifier using a multi-wave model," *J. Opt. Soc. Am. B*, vol. 37, no. 9, pp. 2745–2754, Sep 2020. [Online]. Available: https://opg.optica.org/josab/abstract.cfm?URI=josab-37-9-2745

[109] K. Inoue, "Influence of multiple four-wave-mixing processes on quantum noise of dual-pump phase-sensitive amplification in a fiber," *J. Opt. Soc. Am. B*, vol. 36, no. 6, pp. 1436–1446, Jun 2019. [Online]. Available: https://opg.optica.org/josab/abstract.cfm?URI=josab-36-6-1436

[110] ——, "Phase matching condition of dual-pump phase-sensitive amplification in optical fiber," in *2017 Opto-Electronics and Communications Conference (OECC) and Photonics Global Conference (PGC)*, 2017, pp. 1–2.

[111] P. L. Voss and P. Kumar, "Raman-noise-induced noise-figure limit for $\chi(3)$ parametric amplifiers," *Opt. Lett.*, vol. 29,

no. 5, pp. 445–447, Mar 2004. [Online]. Available: https://opg.optica.org/ol/abstract.cfm?URI=ol-29-5-445

[112] P. Kylemark, P. Hedekvist, H. Sunnerud, M. Karlsson, and P. Andrekson, "Noise characteristics of fiber optical parametric amplifiers," *Journal of Lightwave Technology*, vol. 22, no. 2, pp. 409–416, 2004.

[113] A. Durecu-Legrand, C. Simonneau, D. Bayart, A. Mussot, T. Sylvestre, E. Lantz, and H. Maillotte, "Impact of pump osnr on noise figure for fiber-optical parametric amplifiers," *IEEE Photonics Technology Letters*, vol. 17, no. 6, pp. 1178–1180, 2005.

[114] Z. Yan, H. He, H. Liu, M. Iu, O. Ahmed, E. Chen, P. Blakey, Y. Akasaka, T. Ikeuchi, and A. S. Helmy, "χ2-based algaas phase sensitive amplifier with record gain, noise, and sensitivity," *Optica*, vol. 9, no. 1, pp. 56–60, Jan 2022. [Online]. Available: https://opg.optica.org/optica/abstract.cfm?URI=optica-9-1-56

[115] J. Zhang, S. Ding, H. Zhai, and A. Dang, "Theoretical and experimental studies of polarization fluctuations over atmospheric turbulent channels for wireless optical communication systems," *Opt. Express*, vol. 22, no. 26, pp. 32 482–32 488, Dec 2014. [Online]. Available: https://opg.optica.org/oe/abstract.cfm?URI=oe-22-26-32482

[116] Q. Wang, S. Yu, Y. Zhou, L. Tan, and J. Ma, "Influence of atmospheric turbulence on coherent source in a horizontal long-distance laser link," *Optics & Laser Technology*, vol. 122, p. 105877, 2020. [Online]. Available: https://www.sciencedirect.com/science/article/pii/S0030399219302701

[117] A. V. Anufriev, Y. A. Zimin, A. L. Vol'pov, and I. N. Matveev, "Change in the polarization of light in a turbulent atmosphere," *Soviet Journal of Quantum Electronics*, vol. 13, no. 12, p. 1627, dec 1983. [Online]. Available: https://dx.doi.org/10.1070/QE1983v013n12ABEH005021

[118] K. S. Abedin, M. F. Yan, T. F. Taunay, B. Zhu, E. M. Monberg, and D. J. DiGiovanni, "State-of-the-art multicore fiber amplifiers for space division multiplexing," *Optical Fiber Technology*, vol. 35, pp. 64–71, 2017, next Generation Multiplexing

Schemes in Fiber-based Systems. [Online]. Available: https://www.sciencedirect.com/science/article/pii/S1068520016301079

[119] A. Mikos-Nuszkiewicz, J. Paczos, K. Banaszek, and M. Jarzyna, "Bayesian approach to coherent combination of single photon beams," *Opt. Express*, vol. 32, no. 16, pp. 28 769–28 778, Jul 2024. [Online]. Available: https://opg.optica.org/oe/abstract.cfm?URI=oe-32-16-28769

[120] A. Buchner, S. Hadrath, R. Burkard, F. M. Kolb, J. Ruskowski, M. Ligges, and A. Grabmaier, "Analytical evaluation of signal-to-noise ratios for avalanche- and single-photon avalanche diodes," *Sensors*, vol. 21, no. 8, 2021. [Online]. Available: https://www.mdpi.com/1424-8220/21/8/2887

[121] R. J. Noll, "Zernike polynomials and atmospheric turbulence∗," *J. Opt. Soc. Am.*, vol. 66, no. 3, pp. 207–211, Mar 1976. [Online]. Available: https://opg.optica.org/abstract.cfm?URI=josa-66-3-207

APPENDIX A

Appendix A

A.1 Calculations for the AO-systems

A.1.1 AO model

The adaptive optics (AO) performance will depend heavily on the type of wavefront sensor used, here is an analysis for an ideal sensor that is able to allocate all tapped power (from the beam-splitter) to measure the aberration for the modes of interest only. The average received optical power per corrected mode is

$$P_m = \frac{\eta_{\text{optics}} r_{BS} I_r \pi D^2}{4 N_c} \tag{A.1}$$

where I_r is the time-averaged received intensity, see Fig. 4.1, η_{optics} accounts for the optical path loss from telescope to wavefront sensor and r_{BS} is the beam splitter ratio.

Typical detectors used for wavefront sensors comprise CMOS integrated avalanche photo-detectors (APDs) and single photon avalanche detectors (SPADs) [66] arrays which are typically cooled to reduce dark counts (thermal noise). The signal to noise ratio (SNR) per aberration mode, assuming ideal APD or SPAD detection, is $\eta_{QE} P_m / ah\nu B(1 + I_b/I_r)$ [120]:

$$\text{SNR} = \frac{\eta_{QE} \eta_{\text{optics}} r_{BS} I_r \pi D^2}{4 N_c ch\nu B(1 + I_b/I_r)} = \frac{\eta_{QE} \eta_{\text{optics}} r_{BS} I_r r_0^2}{4 ch\nu p B(1 + I_b/I_r)} \tag{A.2}$$

where η_{QE} is the detector quantum efficiency, $c \geq 1$ for SPAD and $c \geq 3$ for APDs and represents excess detector noise, B is the control loop bandwidth and I_b is the time-average background intensity caused by e.g. daylight scattering. The last equality in Eq. (A.2) uses $N_c = p(D/r_0)^2$ where p is a tunable parameter.

To relate the SNR to a residual phase error we can employ a 1st order PLL as the control system (see chapter 3) with error contributions $\sigma^2_{\phi_e} = \sigma^2_\phi + \sigma^2_N$, where the phase PSD of Eq. (2.4) is standard for AO [46, 47] and is used to calculate $\sigma^2_\phi = \pi S_\phi(1)/B^{5/3}$ via Eq. (3.10) ($B = k_\phi/2\pi$) and we have $\sigma^2_N = 1/\mathrm{SNR}_{\mathrm{OPLL}} = B/(\mathrm{SNR}_{\mathrm{OPLL}} \cdot B)$.

Assuming the same σ^2_ϕ and σ^2_N for each corrected mode compensation, the impact on the final efficiency can be written as [62, 121]

$$\eta_r \simeq 0.81 \exp\left[-\left(C\Big[\frac{D}{r_0}\Big]^{5/3} + \sigma^2_{\phi_e} \right) \right] \tag{A.3}$$

where C is a coefficient of Zernike fitting error

$$C \simeq 0.2944 N^{-\sqrt{3}/2}, \quad N > 10 \tag{A.4}$$

and the entire C-term takes into account the efficiency penalty from compensating a limited amount of modes. The factor 0.81 is obtained for a diffraction limited Bessel-spot to single mode fiber (SMF) matching and will change with telescope type, central obscuration etc. At this point, it is actually the entirety of the exponential argument in Eq. (A.3) that we wish to minimize for optimal AO performance. Thus we rewrite the argument as $\sigma^2 = \sigma^2_J + \sigma^2_\phi + \sigma^2_N$ where

$$\sigma^2_J = \frac{c_J}{p^b}, \quad \sigma^2_\phi = \frac{c_\phi}{B^a}, \quad \sigma^2_N = c_N B p \tag{A.5}$$

with $c_J = 0.2944(D/r_0)^{5/3-\sqrt{3}}$, $c_\phi = \pi S_\phi(1)$, $c_N = 1/(\mathrm{SNR}_{\mathrm{OPLL}} \cdot pB)$, $a = 5/3$ and $b = \sqrt{3}/2$. Here we are free to optimize both p (the number of corrected modes) and the PLL bandwidth B. Following the same

optimization process as in chapter 3 we arrive at the minimized σ^2:

$$\sigma^2 = \left[\left(\frac{b^a}{a^{a+ab}} + a^b b^a + \frac{a^b}{b^{b+ab}}\right) c_J^a c_N^{ab} c_\phi^b\right]^{1/(a+b+ab)} \simeq$$

$$0.8240\left(\frac{D}{r_0}\right)^{-0.0274}\left[\frac{(1+I_b/I_r)}{K_\eta I_r r_0^2}\right]^{0.3630}\left[k^2\int_{\text{path}} C_n^2(z)v^{5/3}(z)dz\right]^{0.2178} =$$

$$\frac{0.8240 B_T^{0.2178}}{D^{0.0274} r_0^{0.4082}}\left[\frac{(1+I_b/I_r)}{K_\eta I_r}\right]^{0.3630} \quad \text{(A.6)}$$

where $K_\eta = \eta_{QE}\eta_{\text{optics}} r_{BS}\pi/4ch\nu$ and the last bracket in the second row was condensed into a single channel parameter B_T. It should be noted that we only incorporated three error contributions to arrive at this expression. For instance, the gain seen by increasing D in this expression is surely cancelled by other implementation penalties that increase with larger telescope sizes.

A.1.2 The ISS to ground AO sensitivity

A power of $P_s - 36.6$ dBm was required to operate the AO system in [63] efficiently. The system used a 1m telescope $D = 1$ and the expected turbulence conditions was $r_0 = 4.5$ cm in the worst case. We assume $N_c = (D/r_0)^2$ number of corrected modes. In this instance the efficiency is modelled as $\eta_r = (\eta_{\text{optics}} P_{r_0} - P_s/N_c)/P_{r_0}$ for $\eta_{\text{optics}} P_{r_0} - P_s/N_c > 0$. This assumes a beam splitter with splitting ratio optimized for each power and which always ensured to feed the sensor with a power P_s/N_c per corrected mode.

A.1.3 Estimation of background intensity

A sunlight intensity of $I_S = 0.19$ W/m^2/nm at $\lambda = 1550$ nm was assumed for daytime, a 100,000 lower intensity was assumed for night time. Of this intensity 23% was assumed scattered (isotropic) with resulting intensity per nanometer and solid angle $0.23 I_S/4\pi$. The field of view of the wave-front sensor was assumed to be $\theta = 0.2°$, i.e. the same as the acceptance angle for the direct detection example in Fig. 2.4 b). Moreover, a $\Delta\lambda = 50$ nm filter was assumed to filter out this noise. The background intensity is then obtained as $I_b = 0.23 I_S \theta^2 \Delta\lambda/4\pi$.

A.2 Factor relating angle of arrival and tip-tilt phase

For efficient fiber coupling for SMF, we have $a \simeq 2.44\lambda f/D$ where the left hand side a is the fiber core and the right side is the spot size. The optimized focal length thus becomes $f = aD/2.44\lambda$. In the multi-mode fiber (MMF) case the optimal focal length is instead $f = ar_0/2.44\lambda$. The displacement δx resulting from an incidence angle θ_x is then $\delta_x = f\theta_x = aD\theta_x/2.44\lambda$. The equivalent OPLL tip-tilt phase is related to the displacement δ_x as $\phi_x = \delta_x/\sigma_r$ where $\sigma_r = r_a a$ where r_a is a factor. Via numerical fitting to a $a = 50$ micron MMF in [B] it was found that $\sigma_r \approx 8.5$ µm for single-mode reception (to the fundamental mode) and $\sigma_r \approx 17$ µm for multi-mode reception, which yields $r_a \simeq 0.17$ and 0.34 respectively. The phase becomes $\phi_x = aD\theta_x/2.44\lambda r_a a = 2.41D\theta_x/\lambda$ in the SMF-case and for the MMF $\phi_x = 1.21r_0\theta_x/\lambda$.